SYNTHESIS AND BATTERY APPLICATION OF NANOMATERIALS AND THE MECHANISM OF O_2 REDUCTION IN APROTIC LI-O_2 BATTERIES

Zheng Liu

A Thesis Submitted for the Degree of PhD
at the
University of St Andrews

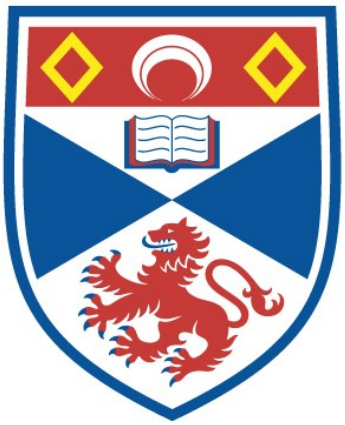

2016

Synthesis and Battery Application of Nanomaterials and The Mechanism of O_2 Reduction in Aprotic Li-O_2 Batteries

Zheng Liu

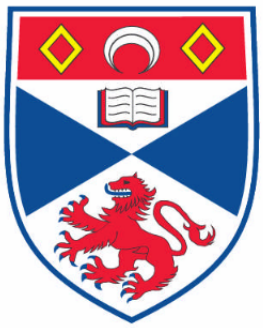

This thesis is submitted in partial fulfilment for the degree of PhD
at the
University of St Andrews

2016

1. Candidate's declarations:
I, Zheng Liu, hereby certify that this thesis, which is approximately words in length, has been written by me, and that it is the record of work carried out by me, or principally by myself in collaboration with others as acknowledged, and that it has not been submitted in any previous application for a higher degree.
I was admitted as a research student in September, 2010 and as a candidate for the degree of PhD in September, 2011; the higher study for which this is a record was carried out in the University of St Andrews between 2010 and 2016.

Date signature of candidate

2. Supervisor's declaration:

I hereby certify that the candidate has fulfilled the conditions of the Resolution and Regulations appropriate for the degree of PhD in the University of St Andrews and that the candidate is qualified to submit this thesis in application for that degree.

Date signature of supervisor

3. Permission for publication: (*to be signed by both candidate and supervisor*)

In submitting this thesis to the University of St Andrews I understand that I am giving permission for it to be made available for use in accordance with the regulations of the University Library for the time being in force, subject to any copyright vested in the work not being affected thereby. I also understand that the title and the abstract will be published, and that a copy of the work may be made and supplied to any bona fide library or research worker, that my thesis will be electronically accessible for personal or research use unless exempt by award of an embargo as requested below, and that the library has the right to migrate my thesis into new electronic forms as required to ensure continued access to the thesis. I have obtained any third-party copyright permissions that may be required in order to allow such access and migration, or have requested the appropriate embargo below.

The following is an agreed request by candidate and supervisor regarding the publication of this thesis:

Embargo on both all of the printed and electronic copy for a period of 2 years on the following ground(s):
Publication would be commercially damaging to the researcher, or to the supervisor, or the University
Publication would preclude future publication

Supporting statement for electronic embargo request:

Date signature of candidate signature of supervisor

Acknowledgements

First of all, I would like to express my deepest gratitude to my supervisor, Prof. Peter G. Bruce, for his patient guidance and precious ideas throughout my research work.

I would like to say thanks to Dr. Yu Ren, Dr. Yuri Andreev and Dr. Lee Johnson for both their help on the fundamental knowledge of nanomaterials, diffraction, and electrochemistry and their hand-by-hand instructions for the experiments and new equipment.

I appreciate the help and suggestions from Dr. Matthew Robert and Dr. Yuri Andreev during my thesis writing. And great thanks to SORS and EPSRC for their funding that supported me during my PhD.

Thanks for all the people who offered help in the research. Mrs. Sylvia Williamson for measuring N_2 adsorption; Dr. Frédérique Pourpoint from University of Cambridge for measuring and interpreting the ^{17}O solid-state MAS NMR; Dr. Chunmei Li and Dr. Yuhui Chen their help on FTIR, Raman, and CV; Dr. Yuan Wang and Dr. Rob Armstrong for the discussion of the nano-TiO_2 project.

Finally I would also like to say thanks to all my group members, Dr. Da Wang, Dr. Kun Luo, Dr. Aleksandra Hekselman, Dr. Juliette Billaud, Dr. Nuria Tapia, Dr. Andrew Naylor, Mr. Xiangwen Gao, Mr. Rong Hao for their help in daily life. It is really joyful to work together with them.

Contents

Abstract

Hunting for improved energy storage devices based on rechargeable Li-ion batteries and other advanced rechargeable batteries is one of the hottest topics in today's society. Both Li-ion batteries and Li-O_2 batteries have been studied within the thesis. The research work of this thesis contains two different parts. Part 1. The controlled synthesis of the extreme small sized nanoparticles and their application for Li-ion batteries; Part 2. The study of the O_2 reduction mechanism in Li-O_2 batteries with aprotic electrolytes.

In the first part, two different types of extremely small-sized TiO_2 nanoparticles with at lease on dimension less than 3 nm was synthesised via solvothermal/hydrothermal reaction, *i.e.*, anatase nanosheets and TiO_2(B). These nanoparticles were obtained without any contamination of long chain organic surfactants. A series of systematic characterisation methods were employed to analyse the size, phase purity, and surface condition. These extremely small-sized nanoparticles exhibit improved capacity, rate performance as anode materials for Li-ion batteries. The shapes of load curves of charge and discharge are significantly modified due to the reduced size of TiO_2 nanoparticles.

In chapter 3, we will see the variation of the capacity and the load curve shape of the anatase nanosheets according to their thickness and surface conditions. The origin of the excessive capacity is analysed based on the electrochemical data. It has been identified that both pseudocapacitive (interfacial) Li^+ storage and the excessive Li^+-storage from the bulk contribute to the increased capacity.

In chapter 4, the shape and size of the sub-3 nm TiO_2(B) nanoparticles are studied, a method based the PXRD data is established. These nanoparticles demonstrate a reversible capacity of 221 mAh/g at a rate of 600 mA/g and remain 135 mAh/g at 18000 mA/g without significant capacity fading during cycling.

In the last part, a systematic study of O_2 reduction mechanism for aprotic Li-O_2 batteries based on the combination of a series of electrochemical and spectroscopic data is presented. The novel mechanism unifies two previous models for the growth of Li_2O_2 during discharge, *i.e.*, Li_2O_2 particle formation in the solution phase and Li_2O_2 film formation on the electrode surface. The new mechanism provides fundamental conceptions for the improvement of Li_2O_2 batteries and shed light on the future research of Li_2O_2 batteries.

Chapter 1 Introduction

Energy storage based on rechargeable lithium-ion batteries (LIB) and other advanced rechargeable LIBs is one of the most pivotal issues in nowadays' society due to their incomparable combination of high specific energy (energy stored per unit weight), convenience, long lifespan, and ecological benefits. The demand of hunting for high quality LIBs stems from every aspect of daily life. On one hand, the quality of portable LIBs, which serve as essential components in portable consumer electronics, such as laptops, and mobile phones, limits the overall quality of the portable electronic devices. On the other hand, large scale of LIBs is required due to the global energy issues. The depletion of conventional energy based on fossil (oil and charcoal) and the heavy pollution from the consumption of such energy requires the substitution by renewable energies, such as wind energy, solar energy, and tide energy. These energies are generally converted into the form of electricity, which is both environmental friendly and of high energy efficiency. The call for large scale LIBs for grid storage, combined the ever-growing demand on LIBs for the electric vehicles (EVs) spurs scientists and engineers to search for more advanced LIBs and even other rechargeable LIBs (such as Li-O_2) with higher specific capacity, better rate performance, longer cycle life, and good safety.

1.1 Fundamentals of Electrochemical Energy Storage and Basic Terminologies Used in Rechargeable Lithium-ion Batteries

Before going into detailed introduction on the rechargeable LIBs and most recent relative works, it is essential to understand some principle about electrochemical energy storage and some basic terminologies with respect to rechargeable batteries.

Although the term "battery" is often used in daily life, the basic electrochemical unit is the "cell". A battery can contain one or more cells, which are connected in serious or parallel to provide required voltage and power. In the thesis, all batteries made for electrochemical characterization contain only one cell.

Electrochemical cell. An electrochemical cell is a device that can convert its chemical energy directly into electric energy by electrochemical redox reaction. It commonly comprises a cathode, an anode, electrolyte, separators, container and terminals[1].

The three major components are:

The cathode—the cathodic reaction takes place on the cathode during discharge, taking up electrons from external circuit and being reduced. Due to its high electrode potential, it is also referred to as “positive electrode”.

The anode—the anodic reaction takes place on the anode during discharge, giving electrons to external circuit and being oxidized. Due to its low electrode potential, it is also referred to as “negative electrode”.

The electrolyte—it is both ionic conductor and electronic insulator. It serves as an ionic medium for charge transfer inside the cell, but blocks the internal electron transfer so that the electrons can be used for external circuit and no self-discharge occurs. During discharge, the cations flow from the negative electrode to the positive electrode, and anions flow the other way around. Note that the ionic flow may involve only one species, depending on the electrochemical reaction and the electrolyte used.

Fig. 1-1 gives a schematic illustration of the cell discharge.

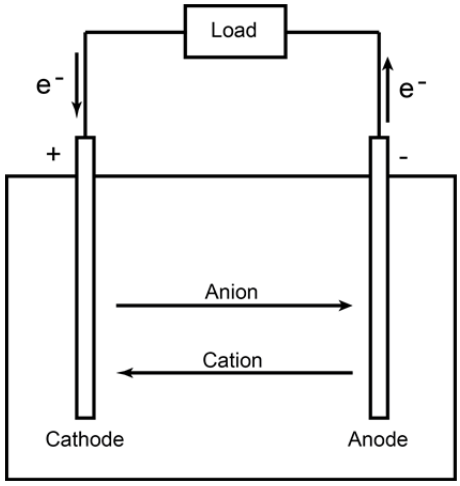

Fig. 1-1 Discharge of An Electrochemical Cell

Rechargeable cell/battery. If redox process is chemically reversible by applying a suitable external electric power, the cell can be recharged. During the charge process, both the ionic and the electronic current flows are reversed, reduction occurs on the negative electrode and oxidation on positive electrode. If the cell/battery can be discharged and recharged, it is called secondary or rechargeable cell/battery.

The cell potential (voltage). The cell potential (voltage, E), which is also called electromotive force (EMF), is determined by the electrode potential difference between the

cathode and the anode, and it can also be calculated using the Gibbs free-energy change of the involved electrochemical reaction (ΔG). [2]

$$E = E_c - E_a = -\frac{\Delta G}{nF} ,$$

where E_c and E_a are electrode potentials of the cathode and the anode respectively, n is the number electrons involved in the electrochemical reaction, and F is the Faraday constant (96485 $C \cdot mol^{-1}$). This formula is used in Chapter 5 to calculate the half-cell potentials in order to get the useful data for fundamental electrochemical analysis.

In fundamental material research for rechargeable LIBs, there are several important factors for the evaluation of the battery materials, including specific capacity, rate performance, columbic efficiency, and cycle life.

Specific capacity. Specific capacity is calculated by dividing the total capacity of the cell/battery by the weight of active material, generally expressed in the unit of mAh/g or $kWh \cdot kg^{-1}$. It reflects the intrinsic capacity of the material itself.

Coulombic efficiency. Coulombic efficiency is the ratio between the energy that can be used upon discharge and the energy that used to charge the cell/battery to its original capacity, express as percentage. It evaluates the energy efficiency of the cell and the material during the cycling.

Cycle life. Cycle life is the number of cycles that a cell/battery can perform before the capacity drops down to 80% of its initial value. Although it is not used in the thesis because some cycling takes extremely long time, all batteries are cycled until 50~200 cycles to show the capacity retention after cycling. It reveals reusability of the materials and batteries.

C-rate. C-rate is a measure of the charge and discharge current of a battery in order to normalise against the maximum capacity. A rate of xC means the discharge/charge current will fully discharge/charge the battery in $1/x$ hours. For example, 1C rate mean to discharge or charge a battery in one hour and 0.5C rate should discharge or charge the battery in 2 h. The specific capacity of the same active material can differ at difference C-rate, the changes of weight ratio of different materials in the composite electrode, or the variation of the thickness of the material on the electrode, due to either the limitation of electronic or ionic conductivity of the active materials, solid-state electrolyte interface (SEI, which is formed due to the reaction between active material and electrolyte.), or the diffusion limitation of

electrolyte in the thick electrode. This phenomenon is shown in Chapter 4. Generally, the intrinsic specific capacity, which corresponds to maximum lithium that can be stored in the active material, is measured at very low rate, where further reduction of the cycling rate will not significantly affect the specific capacity.

1.2 A Brief Introduction To Rechargeable Li-ion Batteries

1.2.1 The Development of Li-metal And Li-ion Batteries

Lithium, the lightest metal with lowest reduction potential, is an ideal choice for battery materials in the concept of delivering highest specific energy. The first generation of lithium batteries based on lithium metal anode were developed in the early 1970s, and were used as primary cells (not rechargeable). Materials that react with lithium reversibly were soon discovered[3]. In 1972, Exxon launched a research project on the first rechargeable lithium battery based on a layer-structured intercalation compound TiS_2 cathode and lithium metal anode, leading by M.S. Whittingham, the first rechargeable lithium batteries were realised[4]. Even though it is not commercialized due to the high cost and handling difficulties of TiS_2, the utilisation of intercalation compound in rechargeable lithium batteries has become a widely accepted idea. Other lithium intercalation materials such as $LiMO_2$ (M=Ni, Co, Mn) were proposed and identified later by John B. Goodenough[5, 6], these materials are still used in modern lithium ion batteries.

The application of lithium metal as the anode in liquid electrolyte were soon realised to be a severe problem due to the dendritic lithium growth during the charge process, which could lead to the explosion of the batteries. The substitution of lithium by intercalation compounds were then proposed by Scrosati[7] and in the meanwhile Rachid Yazami demonstrated the reversibility of electrochemical intercalation of lithium into graphite[8], which is one of the most widely used anode materials in modern Li-ion batteries. The replacement of the lithium metal by the intercalation compound solved the lithium dendrite issue and greatly increased the safety of the Li-ion batteries (LIB). Note they are called Li-ion batteries here, because the lithium intercalation compounds are used, in which lithium presents in its ionic form rather than the metallic state. Sometimes they are also referred to as lithium batteries. The batteries, which employ metallic Li as anodes, can only be referred to as lithium batteries.

1.2.2 The Construction And Materials Choice of Rechargeable Li-ion Batteries

The composition of a lithium-ion cell is the same as the normal electrochemical cell (See 1.1), while the electrodes are both lithium intercalation compounds, and electrolyte contains Li^+ as unique cation. Fig.1-2 describes the configuration of a commercialized lithium-ion battery from SONY. During charging, Li-ions are de-intercalated from cathode ($LiCoO_2$), transporting through the electrolyte, and intercalated into anode (graphite), upon discharging, Li-ions move back to cathode, reversing the charging process. Lithium ions move back and forth between cathode and anode during charge/discharge process, like a rocking chair. Therefore, LIBs are also called rocking chair batteries.

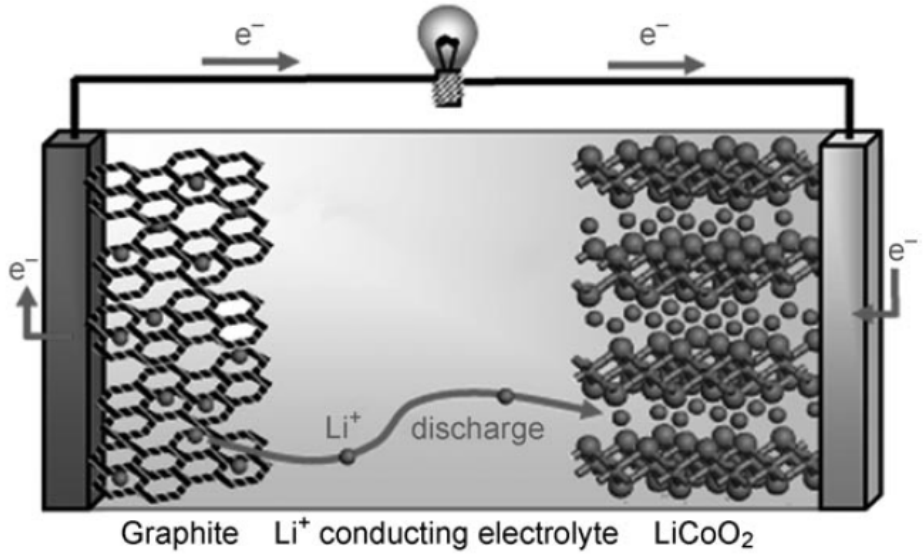

Fig. 1-2 Schematic Illustration of Li-ion Battery. It composes of a graphite anode, a $LiCoO_2$ cathode, and non-aquous Li^+ containing electrolyte (From ref. [9], Angewandte Chemie International Edition, 2008, Wiley).

Cathode Material

The cathode materials have a high electrode potential in Li-ion batteries. It generally contains Li^+ source due to most of the anode materials in Li-ion batteries do not. However, this is not theoretically necessary because pre-lithiated anode materials can be used to provide Li^+. There are three major types of cathode materials—layer-structured $LiMO_2$ (M=Mn, Co, Ni, or combination of these transition-metals in a certain ratio)[5, 10, 11], spinel structure like $LiMn_2O_4$[6], and $LiNi_{0.5}Mn_{1.5}O_4$[12], and polyanion-based materials, like $LiFePO_4$ (olivine structure)[13]. Besides, some metal oxide, such as MnO_2 in various polymorphs and V_2O_5 are all considered as excellent candidates as cathode materials for Li-ion batteries. A typical cathode has a capacity of 100-200 mAh/g, and operating potential of 3.5-5 V *vs.* Li.

Anode Material

The anode materials have a low electrode potential in Li-ion batteries. The most widely used material is graphite, which has very low lithium insertion potential range of 0.1-0.2 V *vs. Li*. Beside graphite, there are lots of other anode materials for L-ion batteries. Conversion material A, such as Si, Sn, and their alloys, based on the alloying and de-alloying reaction between Li and the active material[14-16]; Conversion material B, such as CuO[17], RuO_2[18], based on a conversion reaction of reversible Li_2O formation[9]; Other intercalation materials, such as $Li_4Ti_5O_{12}$[19], TiO_2[20], and $Li_{1+x}V_{1-x}O_2$[21], based on Li^+ insertion and de-insertion. The capacity of anode materials varies from several hundred (~350 mAh/g for graphite[22]) to several thousand (Si electrode, whose theoretical is 3950 mAh/g[14], although the practical capacity varies depending on the size and morphology of the nanoparticles). The electrode potential of the anode materials *vs.* Li^+ is generally below 2 V.

Electrolyte

The electrolytes for Li-ion batteries are Li^+ conductive liquids, solids, or polymers, which are electronic insulators and non-reactive towards the electrode materials, the anions in the electrolytes are electrochemical inert (not reactive with electrode during charge and discharge of a battery), such as PF_6^-, $CF_3SO_2NSO_2CF_3^-$ ($TFSI^-$), and ClO_4^-. The most widely used electrolytes are LP30 (1M $LiPF_6$, in 1:1 w/w ethylene carbonate: dimethyl carbonate), LP40 (1M $LiPF_6$, in 1:1 w/w ethylene carbonate: diethyl carbonate), and polyethylene oxide (PEO) based polymer electrolytes.

1.2.3 Improving The Performance of Li-ion Battery Materials

The improvement of the performance of a Li-ion cell is a very complicated topic. There are many factors that have impacts on the performance of the total cell, including the property of the active material, compatibility of the electrodes and electrolytes, the composition and structure of composite electrode and even the design of the cell. Since in this thesis work, the improvement of Li-ion battery performance is only focused on the aspect of the battery materials, here we only introduce some classical methods for improving the performance of electrode materials.

The performance of the Li-ion battery materials depends both on their intrinsic property and on the microscopic morphology.

The intrinsic property of the materials, like the type of materials, and crystal structures (only applicable to the crystalline materials), determines electrochemical potential of Li^+, available Li^+ sites, Li^+ conductivity inside the active materials, and electronic conductivity. The available Li sites are directly associates with the theoretical specific capacity, and the ionic and electronic conductivity have enormous impact on the high-rate performance. The stability of the active material matrix influences the cycle life. For example, conversion material generally suffer from the pulverization due to the massive volume change during lithiation and delithiation process, leading to huge capacity loss upon cycling[15]. But a lot of Li-insertion compounds have marginal volume changes during cycling. Another example involves different polymorphs of TiO_2. Anatase and TiO_2(B) are two distinctive polymorphs of TiO_2, which have different crystal structures (See Chapter 2 and Chapter 3). It has been established both theoretically and experimentally that the later has a more energetically favourable structure for faster lithium diffusion (better high-rate performance) and can theoretically accommodate more lithium (higher capacity) [23-27] at 1 V as large paticles, and furthermore, the discharge plateau of TiO_2(B) is 1.4-1.65 V[28], also lower than that of anatase—1.75 V[29]. The investigation of better materials generally entails alteration of crystal structures, and doping of other elements, coating of conductive carbons, *etc*.

The microscopic morphology, such as particle size, shape, specific surface area, and porosity, also has vast contribution to the performance of battery materials. Reduction of the size of the active material particles generally leads to the improvement of the electrochemical performance. Since the thesis work is mainly about the synthesis and battery application of the extremely small-sized nanoparticles, we will spend the next section to introduce the underlying principles and remarkable research works on the application of nanomaterials for Li-ion batteries.

1.3 Nanomaterials For Li-ion Batteries

1.3.1 The Advantage of Nanomaterials For Li-ion Batteries

The benefits of using nanomaterials for Li-ion batteries are ascribed to the following reasons:

1. The reduction of the particle size dramatically reduces the diffusion length of Li^+ inside the particles. Calculated from Fick's law of diffusion, the diffusion time t is given by the equation, $t = L^2/D$, where L is the diffusion length for Li^+ to reach the particle centre from the edge of the particle, and D is the diffusion coefficient. According to the

equation, the diffusion time t is in proportional to the square of the diffusion length L. In principle, a nanoparticle, whose dimension is $1/n$ of the bulk particles, can be charged/discharged within $1/n^2$ time that is required to charge/discharge the bulk material in the same condition[30]. Therefore, the application of nanomaterials significantly improves the high rate performance of the Li-ion batteries. *E.g.*, the impact of the particle size on the rate performance of anatase nanoparticles has been systemically demonstrated in the research work of Haoshen Zhou et al[31].

2. Due to the same reason, the transport of electrons inside the nanoparticle can also be promoted with a reduced particle size.

3. A nanomaterial generally has a high specific surface area. This high specific surface area provides more contact between active materials and electrolyte, allowing more Li^+ to transport across the electrode/electrolyte interface in the same time under the same condition. The enhancement of the ionic transport rate across the interface, which also leads to a better rate performance.

4. When the size of the nanoparticles becomes small enough, the electrode potential can be thermodynamically modified due to the contribution of high surface energy of the nanoparticles, resulting in the modification of the cell voltage[32, 33].

5. The capacity contribution from pseudocapacitive or grain boundary Li storage becomes more significant with decreased particle size, as a result of the increased surface area. D. Bruce *et al.* have demonstrated a considerable increase of the capacity from pseudocapacitive Li storage with decreased particle size on anatase material[34].

6. The nanosizing of materials can promote the Li-solubility inside the solids and corresponding solid-solution behaviour in the insertion materials, modifies the load curve, as well as alerts the insertion capacity[35].

7. The strains due to the intercalation of Li^+ are better accommodated in nanomaterials, and it permits some electrochemical Li^+ insertion to take place in nanomaterials even the reaction cannot occur in the micron-sized or larger bulk materials. The best example is the remarkable work on mesoporous β-MnO_2 published P. G. Bruce *at el.*, in which the mesoporous β-MnO_2 with nanosized walls is proven to be able to reversibly intercalate of Li^+ without destroying its crystal structure, while the sub-micrometre-sized bulk material does not show any electrochemical activity at all[36].

1.3.2 The Drawbacks of Nanomaterials For Li-ion Batteries

Despite the tremendous benefits stated above, there are still some drawbacks associated with the application of nanomaterials in Li-ion batteries.

1. Synthesis of nanomaterials can be quite complicated and expensive. The control of particle size and shape often requires surfactants, which can alter the property of the nanoparticles. The surfactants are sometimes difficult to remove without changing the size and shape of the as-synthesised nanoparticles. This is especially true when the required dimensions of nanoparticles are extremely small, *e.g*, less than 5 nm. The extremely small-sized TiO_2 nanoparticles was obtained without

2. The high specific surface area of the nanoparticles can lead to more severe side reaction between the electrode material and electrolyte at the interface, due to the decomposition of electrolyte on high-energy nanoparticle surface, generally resulting in a high initial capacity loss on the first cycle. Surface treatment with lithium bases, like lithium ethoxide can significantly alleviate this problem due to the reduction of the surface reactivity. Section 4.3.6 serves as a good example for the partial elimination of the initial irreversible capacity loss by such method.

3. The loose packing of the nanoparticles decreases the density of the materials, and hence results in less the volumetric energy density.

1.3.3 Previous Achievements On Nano TiO_2 Based Anode Materials

The first part of this thesis work demonstrates the synthesis of extremely small-sized TiO_2 nanoparticles and their electrochemical property—both anatase (Chapter 3) and TiO_2(B) (Chapter 4) nanoparticles with at least one dimension less than 3 nm. Here, we will introduce some previous achievements on the synthesis and the battery application of the TiO_2 nanomaterials.

Two polymorphs of TiO_2, anatase and TiO_2(B), are generally considered as possible graphite alternatives as anode materials for Li-ion batteries, because of their comparable theoretical capacity (334 mAh/g if fully lithiated) to that of graphite (~350 mAh/g), reasonable cycleability, and less safety concerns due to their higher operating potential (1.4-1.8 V), which alleviates the electrolyte decomposition and eliminates the lithium plating problem of graphite during cycling[37-39].

The highly size-dependant electrochemical performance of TiO_2 has been demonstrated by a lot of research groups, including the gradually increased capacity with the reduction of particle size, modification of the load curve, and enhanced rate performance of smaller nanoparticles. The underlying principles have been elucidated in Section 1.3.1.

The exceptional rate performance of anatase nanostructure has been manifested by P. G. Bruce's group in 2009. The mesoporous nano anatase electrode synthesised by hard template method can sustain a capacity of 125 mAh/g at 12 $A \cdot g^{-1}$ (37.5C);

Xiongwen Lou *et al.* has constructed a hierarchical structure with ultrathin anatase nanosheets, which delivers a reversible capacity of ~180 mAh/g at 1C, exceeding the theoretical reversible capacity of 167 mAh/g for anatase according to 0.5 Li for TiO_2 formula[40].

J. Maier's group has achieved a 302 mAh/g at 1 C and 229 mAh/g at 5 C with 5 nm porous anatase nanoparticles, and ascribed the excessive capacity to the pseudocapacitive (interfacial) storage of Li^+ on the surface TiO_2[41].

Studies from M. Wagemaker *et al.* claims that the excessive capacity of the extremely small sized nano anatase is due to the formation of a newly found poor Li^+-conductive phase Li_1TiO_2, which is kinetically allowed due to the short Li^+ diffusion length of the below 7 nm anatase nanoparticles[35].

In the meanwhile, the research and development in nanosized TiO_2(B) has reached a new milestone. The application of TiO_2(B) nanowires[42] and nanotubes[43] as anode materials for Li-ion batteries has significantly increased the capacity of TiO_2(B). The TiO_2(B) nanowires can accommodate 0.91 Li for TiO_2 nanowires ($Li_{0.91}TiO_2$), while the nanotubes can accommodate 0.98 Li for TiO_2 ($Li_{0.98}TiO_2$) on initial discharge, corresponding to an initial discharge capacity of 303 mAh/g and 327 mAh/g, while the initial discharge capacity of the micron-sized bulk TiO_2(B) is only 237 mAh/g.

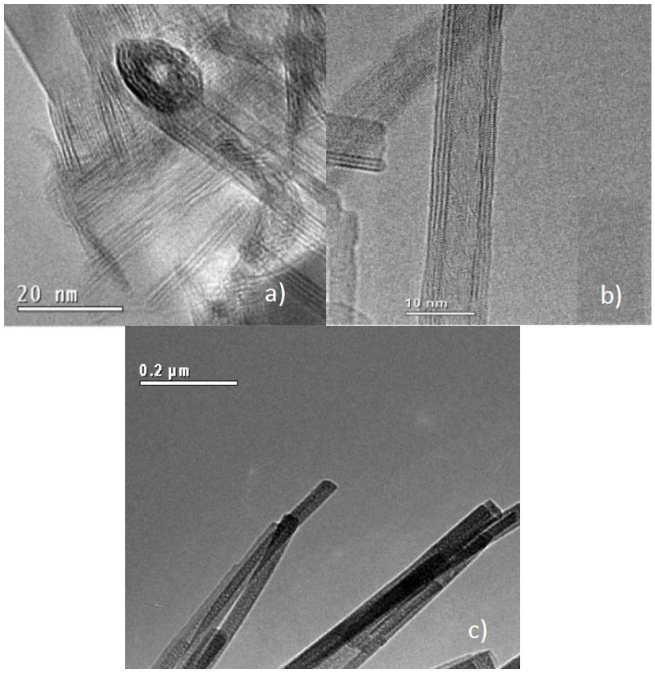

Fig. 1-3 The Morphology of TiO_2(B) nanotubes and nanowires. (a), (b) the morphology of the nanotubes(From ref. [43]); (c) the morphology of nanowires (From ref. [42])

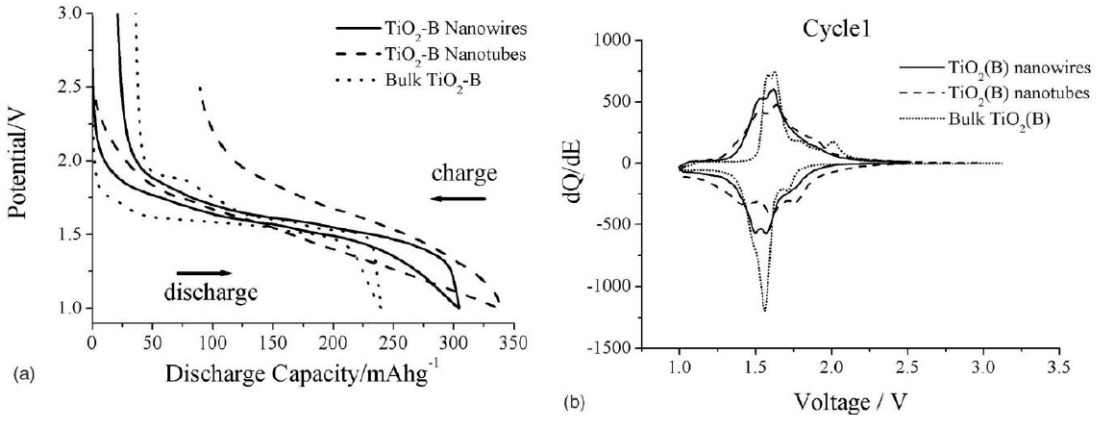

Fig. 1-4 Size And Shape Dependant Electrochemical Performance of Different TiO_2(B). a) first charge/discharge curves of TiO_2(B) nanotubes, nanowires, and bulk TiO_2(B) at 10 mA/g between voltage limits of 1-3 V; b) Incremental capacity plots (From ref. [25].)

Fig. 1-3 and Fig. 1-4 illustrate the morphology of TiO_2(B) nanotubes and nanowires and first charge/discharge curves for these materials respectively, giving us a visual impression of how these extremely small-sized nanoparticles alert the capacities, modifies the load curves (characterised by the loss of plateau). In Chapter 4, the sub-3 nm TiO_2(B) nanoparticles will be presented, which brings higher capacity with the similar lithiation behaviour. The detailed discussion is made in the particular chapter.

1.4 Advanced Rechargeable Lithium Battery—non-aqueous Li-O_2 Battery

1.4.1 The Advantages of non-aqueous Li-O2 Batteries

Despite of the success of the Li-ion batteries on the global markets, the hunting for more advanced rechargeable batteries has never been discontinued. Aiming at several times of the specific energy and energy density that the normal Li-ion batteries can achieve, the research on non-aqueous rechargeable Li-O_2(Air) batteries has attracted considerable attention from many research groups and companies.

A non-aqueous Li-O_2 battery is similar to Li-metal and Li-ion batteries, but involves different cathode reactions. Instead of Li^+ insertion/removal reaction with cathode materials, in Li-O_2 battery, Li^+ reacts and combines with electrochemically reduced O_2, forming Li_2O_2 particles upon discharge; and during charge, the Li_2O_2 can be oxidized, releasing Li^+, and O_2 evolves. And the reactions on the anode side are totally the same with normal Li-metal/Li-ion batteries.

Based on the cell reaction $2Li + O_2 \leftrightarrow Li_2O_2$, the non-aqueous Li-$O_2$ batteries can theoretically operate at a voltage of 2.96 V with a specific capacity of 1168 mAh/g (based on cathode weight due to the formation of Li_2O_2, assuming the anode is Li-metal), and hence delivers a theoretical specific energy of 3.46 kWh·kg^{-1}[44], which is ~6 times of that of a $LiCoO_2$-graphite battery (0.584 kWh·kg^{-1}[45]), over 9 times of that of LiFePO4-graphite battery (0.373 kWh·kg^{-1}[45]). If this is achieved, all portable electronics can be used much longer after every single charge, and it will permit electric vehicles to beat the traditional automobiles based on gasoline consumption.

1.4.2 The Principle And Mechanism of non-aqueous Li-O_2 batteries

Although the cell reaction looks extremely simple, the reaction mechanism on the cathode side is quite complicated.

Discharge—O_2 Reduction Reaction (ORR)

The ORR mechanism is similar in various aprotic electrolytes, such as dimethyl sulfoxide (DMSO), ethers, and acetonitrile[46-48]. Despite final discharge product is Li_2O_2, the ORR is not a 2-e^- process. O_2 is firstly reduced to O_2^- through a 1-e^- reduction (Reaction 1-1). Then O_2^- rapidly combines with a Li^+ to form LiO_2, which can exist either in form of dissolved species in the solution, or in form of solid on the electrode surface. (Reaction 1-2). The LiO_2 can either be further reduced by another electron and combines with Li^+ to form Li_2O_2

electrochemically (Reaction 1-3a), or undergo spontaneous chemical disproportionation to form Li_2O_2 and O_2 (Reaction 1-3b).

$$O_2 + e^- \longrightarrow O_2^- \quad (1\text{-}1)$$

$$O_2^- + Li^+ \longrightarrow LiO_2 \quad (1\text{-}2)$$

$$LiO_2 + Li^+ + e^- \rightleftharpoons Li_2O_2 \quad (1\text{-}3a)$$

$$2LiO_2 \longrightarrow Li_2O_2 + O_2 \quad (1\text{-}3b)$$

Reaction 1-3a and 1-3b are competitive reactions, which leads to different models of Li_2O_2 formation—surface model, and solution model. The morphology and growth of Li_2O_2 are very different, resulting in significant difference of the capacity, cycleability, rate performance, *etc*.

The detailed mechanism will be discussed in the last experimental chapter (Chapter 5).

Charge—O_2 Evolution Reaction (OER)

The charge of Li-O_2 cell (OER) is different from that of discharge because of the absence of LiO_2 intermediate. Shao-Horn *at el.* has proposed a mechanism based on the study of the overpotential associated with charging process and divided the OER into 3 stages[49]. Stage 1, the slope region from 2.9 V to 3.4 V, is ascribed to delithiation of the Li_2O_2 through solid solution process, producing LiO_2-like species from the outside part of the Li_2O_2 particles and then this LiO_2-like species disproportionate to form Li_2O_2 and O_2; Stage 2, the plateau region on the charge curve, is the direct oxidation of the Li_2O_2 via two phase transition; Stage 3 is the oxidation of the by-products formed during discharge.

Reference:

1. Linden, D. *Handbook of batteries*. in *Fuel and Energy Abstracts*. 1995.
2. Bard, A.J. and L.R. Faulkner, *Electrochemical methods: fundamentals and applications*. Vol. 2. Wiley New York.
3. Tarascon, J.M. and M. Armand, *Issues and challenges facing rechargeable lithium batteries.* Nature, 2001. **414**(6861): p. 359-367.
4. Whittingham, M.S., *Electrical energy storage and intercalation chemistry.* Science, 1976. **192**(4244): p. 1126-1127.
5. Mizushima, K., et al., *LixCoO2 (0<x<-1): A new cathode material for batteries of high energy density.* Materials Research Bulletin, 1980. **15**(6): p. 783-789.
6. Thackeray, M.M., et al., *Lithium insertion into manganese spinels.* Materials Research Bulletin, 1983. **18**(4): p. 461-472.
7. Lazzari, M. and B. Scrosati, *A Cyclable Lithium Organic Electrolyte Cell Based on Two Intercalation Electrodes.* Journal of The Electrochemical Society, 1980. **127**(3): p. 773-774.
8. Yazami, R. and P. Touzain, *A reversible graphite-lithium negative electrode for electrochemical generators.* Journal of Power Sources, 1983. **9**(3): p. 365-371.
9. Bruce, P.G., B. Scrosati, and J.-M. Tarascon, *Nanomaterials for Rechargeable Lithium Batteries.* Angewandte Chemie International Edition, 2008. **47**(16): p. 2930-2946.
10. Choi, J. and A. Manthiram, *Role of Chemical and Structural Stabilities on the Electrochemical Properties of Layered LiNi1 / 3Mn1 / 3Co1 / 3O2 Cathodes.* Journal of The Electrochemical Society, 2005. **152**(9): p. A1714-A1718.
11. Zhou, F., et al. *Comparison of LiNi2/3Mn1/3O2, LiNi1/3Mn1/3Co1/3O2, LiNi0. 5Mn0. 3Co0. 2O2 and LiNi0. 42Mn0. 42Co0. 16O2 as Positive Electrode Materials for Lithium-Ion Batteries*. in *Meeting Abstracts*. 2010. The Electrochemical Society.
12. Kim, J.H., et al., *Comparative Study of LiNi0.5Mn1.5O4-δ and LiNi0.5Mn1.5O4 Cathodes Having Two Crystallographic Structures: Fd3m and P4332.* Chemistry of Materials, 2004. **16**(5): p. 906-914.
13. Padhi, A.K., K. Nanjundaswamy, and J. Goodenough, *Phospho‐olivines as positive‐electrode materials for rechargeable lithium batteries.* Journal of the electrochemical society, 1997. **144**(4): p. 1188-1194.
14. Liu, W.-R., et al., *Effect of electrode structure on performance of Si anode in Li-ion batteries: Si particle size and conductive additive.* Journal of Power Sources, 2005. **140**(1): p. 139-144.
15. Zhang, W.-J., *A review of the electrochemical performance of alloy anodes for lithium-ion batteries.* Journal of Power Sources, 2011. **196**(1): p. 13-24.
16. Whitehead, A.H., J.M. Elliott, and J.R. Owen, *Nanostructured tin for use as a negative electrode material in Li-ion batteries.* Journal of Power Sources, 1999. **81–82**: p. 33-38.
17. Sahay, R., et al., *High Aspect Ratio Electrospun CuO Nanofibers as Anode Material for Lithium-Ion Batteries with Superior Cycleability.* The Journal of Physical Chemistry C, 2012. **116**(34): p. 18087-18092.
18. Balaya, P., et al., *Fully Reversible Homogeneous and Heterogeneous Li Storage in RuO2 with High Capacity.* Advanced Functional Materials, 2003. **13**(8): p. 621-625.

19. Zaghib, K., et al., *Electrochemical study of Li 4 Ti 5 O 12 as negative electrode for Li-ion polymer rechargeable batteries.* Journal of Power Sources, 1999. **81**: p. 300-305.
20. Zachau-Christiansen, B., et al., *Lithium insertion in different TiO 2 modifications.* Solid State Ionics, 1988. **28**: p. 1176-1182.
21. Armstrong, A.R., et al., *The lithium intercalation process in the low-voltage lithium battery anode Li1+xV1−xO2.* Nat Mater, 2011. **10**(3): p. 223-229.
22. Endo, M., et al., *Recent development of carbon materials for Li ion batteries.* Carbon, 2000. **38**(2): p. 183-197.
23. Dalton, A.S., A.A. Belak, and A. Van der Ven, *Thermodynamics of Lithium in TiO2(B) from First Principles.* Chemistry of Materials, 2012. **24**(9): p. 1568-1574.
24. Arrouvel, C., S.C. Parker, and M.S. Islam, *Lithium Insertion and Transport in the TiO2−B Anode Material: A Computational Study.* Chemistry of Materials, 2009. **21**(20): p. 4778-4783.
25. Armstrong, G., et al., *TiO2 (B) Nanotubes as Negative Electrodes for Rechargeable Lithium Batteries.* Electrochemical and Solid-State Letters, 2006. **9**(3): p. A139-A143.
26. Zhang, T., et al., *Understanding electrode materials of rechargeable lithium batteries via DFT calculations.* Progress in Natural Science: Materials International, 2013. **23**(3): p. 256-272.
27. Lindström, H., et al., *Li+ Ion Insertion in TiO2 (Anatase). 2. Voltammetry on Nanoporous Films.* The Journal of Physical Chemistry B, 1997. **101**(39): p. 7717-7722.
28. Armstrong, A.R., et al., *Lithium Coordination Sites in LixTiO2(B): A Structural and Computational Study.* Chemistry of Materials, 2010. **22**(23): p. 6426-6432.
29. Wagemaker, M., et al., *Multiple Li Positions inside Oxygen Octahedra in Lithiated TiO2 Anatase.* Journal of the American Chemical Society, 2003. **125**(3): p. 840-848.
30. Arico, A.S., et al., *Nanostructured materials for advanced energy conversion and storage devices.* Nat Mater, 2005. **4**(5): p. 366-377.
31. Jiang, C., et al., *Particle size dependence of the lithium storage capability and high rate performance of nanocrystalline anatase TiO2 electrode.* Journal of Power Sources, 2007. **166**(1): p. 239-243.
32. Balaya, P., et al., *Nano-ionics in the context of lithium batteries.* Journal of Power Sources, 2006. **159**(1): p. 171-178.
33. Jamnik, J. and J. Maier, *Nanocrystallinity effects in lithium battery materials Aspects of nano-ionics. Part IV.* Physical Chemistry Chemical Physics, 2003. **5**(23): p. 5215-5220.
34. Wang, J., et al., *Pseudocapacitive Contributions to Electrochemical Energy Storage in TiO2 (Anatase) Nanoparticles.* The Journal of Physical Chemistry C, 2007. **111**(40): p. 14925-14931.
35. Wagemaker, M., W.J.H. Borghols, and F.M. Mulder, *Large Impact of Particle Size on Insertion Reactions. A Case for Anatase LixTiO2.* Journal of the American Chemical Society, 2007. **129**(14): p. 4323-4327.
36. Jiao, F. and P.G. Bruce, *Mesoporous Crystalline β-MnO2—a Reversible Positive Electrode for Rechargeable Lithium Batteries.* Advanced Materials, 2007. **19**(5): p. 657-660.

37. Aurbach, D., et al., *A short review of failure mechanisms of lithium metal and lithiated graphite anodes in liquid electrolyte solutions.* Solid State Ionics, 2002. **148**(3–4): p. 405-416.
38. Subramanian, V., et al., *Nanocrystalline TiO2 (anatase) for Li-ion batteries.* Journal of Power Sources, 2006. **159**(1): p. 186-192.
39. Liu, Z., et al., *Nanostructured TiO2(B): the effect of size and shape on anode properties for Li-ion batteries.* Progress in Natural Science: Materials International, 2013. **23**(3): p. 235-244.
40. Chen, J.S., et al., *Constructing Hierarchical Spheres from Large Ultrathin Anatase TiO2 Nanosheets with Nearly 100% Exposed (001) Facets for Fast Reversible Lithium Storage.* Journal of the American Chemical Society, 2010. **132**(17): p. 6124-6130.
41. Shin, J.-Y., D. Samuelis, and J. Maier, *Sustained Lithium-Storage Performance of Hierarchical, Nanoporous Anatase TiO2 at High Rates: Emphasis on Interfacial Storage Phenomena.* Advanced Functional Materials, 2011. **21**(18): p. 3464-3472.
42. Armstrong, A.R., et al., *TiO2-B Nanowires.* Angewandte Chemie International Edition, 2004. **43**(17): p. 2286-2288.
43. Armstrong, G., et al., *Nanotubes with the TiO2-B structure.* Chemical Communications, 2005(19): p. 2454-2456.
44. Christensen, J., et al., *A critical review of Li/air batteries.* Journal of the Electrochemical Society, 2011. **159**(2): p. R1-R30.
45. Lu, Y.-C., et al., *Lithium-oxygen batteries: bridging mechanistic understanding and battery performance.* Energy & Environmental Science, 2013. **6**(3): p. 750-768.
46. Laoire, C.O., et al., *Elucidating the Mechanism of Oxygen Reduction for Lithium-Air Battery Applications.* The Journal of Physical Chemistry C, 2009. **113**(46): p. 20127-20134.
47. Laoire, C.O., et al., *Influence of Nonaqueous Solvents on the Electrochemistry of Oxygen in the Rechargeable Lithium–Air Battery.* The Journal of Physical Chemistry C, 2010. **114**(19): p. 9178-9186.
48. Laoire, C., et al., *Rechargeable Lithium/TEGDME- LiPF6 / O2 Battery.* Journal of The Electrochemical Society, 2011. **158**(3): p. A302-A308.
49. Lu, Y.-C. and Y. Shao-Horn, *Probing the Reaction Kinetics of the Charge Reactions of Nonaqueous Li–O2 Batteries.* The Journal of Physical Chemistry Letters, 2013. **4**(1): p. 93-99.

Chapter 2 Characterisation Techniques

2.1 Powder X-Ray Diffraction (PXRD)

Powder X-ray diffraction is one of the most widely used non-destructive techniques in chemistry and material science for characterising crystalline materials. It is generally used for phase identification, lattice parameter calculation, particle size analysis, strain analysis and etc.

The principle of X-ray diffraction has been established by Laue and the Bragg family in 1910s, more than 15 years later after the discovery of the X-rays by W.C. Röntgen in 1895. The wavelengths of X-rays used in crystallography, ranging from 0.5 and 2.5 Å, are in the same order of magnitude as the shortest interatomic spacings in crystalline materials. Therefore, when X-rays propagate through a substance, the process of diffraction will take place. The X-ray photons are scattered by each of the atoms in the crystalline sample.

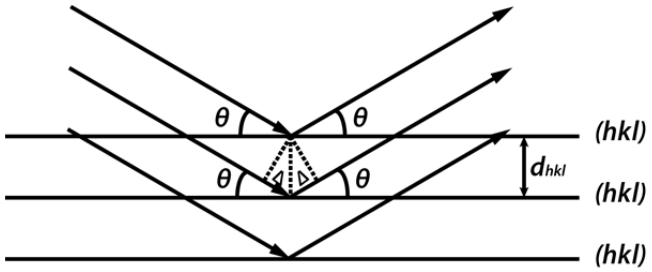

Fig. 2-1 Geometry of Bragg Diffraction on (hkl) Plane

According to Braggs' study, diffraction from a crystalline substance can be explained and described by using a simple mirror reflection of the incident X-ray beam on a series of crystallographic planes.

As shown in Fig. 2-1, the (*hkl*) planes of a perfect crystal are parallel to each other, equally spaced by the interplanar distance of d_{hkl}, and repeated infinitely. The diffraction of X-rays from such a set of planes is restricted to some specific angles, θ. When a parallel incident beam hits the (*hkl*) planes from an angle θ, the reflected beam will also be of the same angle from these planes. The path difference between the incident and reflected beams by neighbouring planes is $2d_{hkl}\sin\theta$, the constructive interference from this infinite periodic structure will only occur when the path difference satisfies,

$$2d_{hkl}\sin\theta = n\lambda,$$

where n is an integer, known as the order of diffraction and λ is the wavelength of the X-ray. In calculation, the value of n is generally taken as 1, since the higher order diffraction (n>1), can always be simplified by using the relationship $d_{hkl} = nd_{nh,nk,nl}$, resulting in[1],

$$2d_{nh,nk,nl}\sin\theta_{nh,nk,nl} = \lambda,$$

where $d_{nh,nk,nl}$ is the interplanar distance from the crystallographic planes of multiple Miller indices. The intensity of the diffraction is determined by the crystal structure and atomic properties. Therefore, the diffraction patterns from different materials are unique, and can be considered as fingerprints of these materials. Phase identification is by comparing the real diffraction pattern with the standard diffraction patterns, e.g., the powder diffraction files (PDF) provided by the International Centre for Diffraction Data (ICDD) or the files from the Inorganic Chemical Structure Database (ICSD).

Another important information we can get from the PXRD pattern is the average crystallite size and shape according to the peak broadening. There are many factors that determine the shape of the peaks, *i.e.*, instrumental factor, strain, and average crystallite size. In this thesis, the size effect is the main factor of the peak broadening, because the sizes of the synthesized materials are all below 10 nm. When the size of the crystal reduces to below several microns, the periodic structure of the crystal can no longer be considered as infinite. In this case, diffraction intensity will not immediately drop to zero when θ deviates a little from the specific angle calculated according to the Bragg's law.

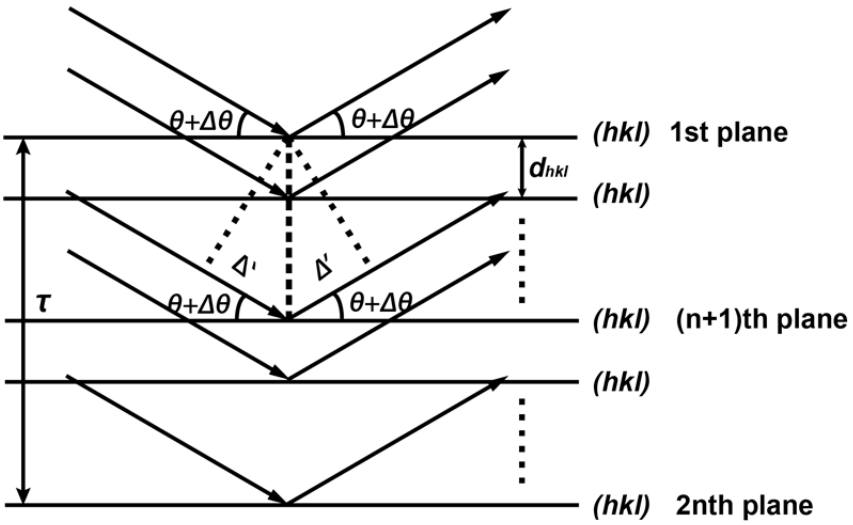

Fig. 2- 2 Illustration of the Scherrer Equation

Fig. 2-2 illustrates the limit condition in which the diffraction intensity drops to zero in case of an even number (2n layers) of crystal planes (For old number of crystal planes, since intensity of the scattering from only one single crystal plane is very low, it is reasonable to use a closest even number to approximate, which also does not make too much difference in crystallite size). Under this circumstance, the reflection angle deviates from the Bragg angle by a small angle of $\Delta\theta$, resulting in a destructive interference of the beam reflected by the 1st plane and the (n+1)th plane. The same applies to the beam reflected by the 2nd and (n+2)th planes, nth and 2nth planes, and so on, which nullifies the total diffraction intensity. The path difference between the 1st beam and the (n+1)th beam is calculated by

$\Delta' = 2\times\frac{\tau}{2}\sin(\theta+\Delta\theta) \approx \tau\Delta\theta\cos\theta$ ($\Delta\theta$ is a small angle, and in unit of radian),

When the first destructive interference appears,

$$\Delta' = \frac{\lambda}{2}.$$

Hence,

$$\tau = \frac{\lambda}{2\Delta\theta\cos\theta},$$

In practice, it is hard to correctly measure the width of a peak from the very bottom; instead, the full width at the half maximum (FWHM, β) is commonly applied.

$\beta = k\Delta(2\theta) = 2k\Delta\theta$, (note the PXRD patterns are plotted against 2θ, where k is the peak shape factor, which has a value around 1).

Considering the fact that the (hkl) planes are not infinite in length and their length is not even identical due to the shape of the actual crystallites, there should be a factor in relevant with the crystallite shape included in the equation, resulting in the Scherrer equation,

$$\tau_{hkl} = \frac{K\lambda}{\beta\cos\theta_{hkl}},$$

where $\tau_{h\square l}$ is the average size of the crystallites along the <*hkl*> direction, K is the shape factor, generally considered to be 0.9, λ is the wavelength of the incident X-ray, β is the full width at the half maximum (FWHM) in the unit of radian. It is worth noting that Scherrer

equation is only an approximation of the particle size. In practice, when the PXRD pattern is from low symmetric crystal system, the peaks will generally overlap, some software, like GSAS, can be employed to analyse the FWHM of each peaks by refinement using the peak shape profile factors.

In order to achieve a more reliable size and shape information, some other full-profile refinements must be applied, such as the refinement based on Debye equation,

$$I(\theta) = \sum_n f_n^2(\theta) + 2\sum_i \sum_j f_i(\theta) f_j(\theta) \frac{\sin(4\pi r_{ij}\sin\theta/\lambda)}{4\pi r_{ij}\sin\theta/\lambda},$$

where $f_n(\theta)$ is the atomic factor of the corresponding atoms in the real crystal, λ is the wavelength of the X-ray, and r_{ij} is the distance between the i^{th} and the j^{th} atoms in the particle. The summation is carried out over all atoms in a single nanocrystal. The best-fit of using this equation with the experimental pattern will give information about the best average particle shape and size. For detailed information, please see Chapter 4.3.

In this thesis, PXRD patterns are collected using an Empyrean PANalytical diffractometer, operating in reflection mode with Cu $K_{\alpha 1}$ radiation (λ = 1.541 Å), if not specified. Step size is 0.017^o, general scan time is 1 hour. A zero background single-crystal silicon substrate was used as the sample holder.

2.2 X-ray Photoelectron Spectroscopy (XPS)

X-ray photoelectron spectroscopy (XPS) is a surface sensitive technique, which measures quantitatively the surface elemental composition, oxidation state, chemical environments of the elements, and electronic structure in solids[2].

Aside from diffraction effect, when X-rays interact with matters, the electrons in the illuminated materials can also be excited and escape from the substance to an unbounded state. The kinetic energy of the emitted electron and the intensity are measured by a XPS spectrometer. The XPS spectrum is a plot of the number of electrons detected *vs.* the binding energy (sometimes use kinetic energy directly) of the excited electrons.

The electrons detected in XPS spectrum may come from two processes-- photoelectron emission and Auger electron emission, see Fig. 2-3. In Fig. 2-3 (a). An electron from the K shell is knocked out from solid by an X-ray photon, the binding energy of this electron (E_b) can be expressed in terms of energy of the illuminating X-ray beam (E_p), the kinetic energy

observed in the electron detector (E_k), and the work function with respect to the spectrometer level (ϕ)[3].

$$E_b = E_p - (E_k + \phi),$$

The work function term can be eliminated by calibration of the electron spectrometer.

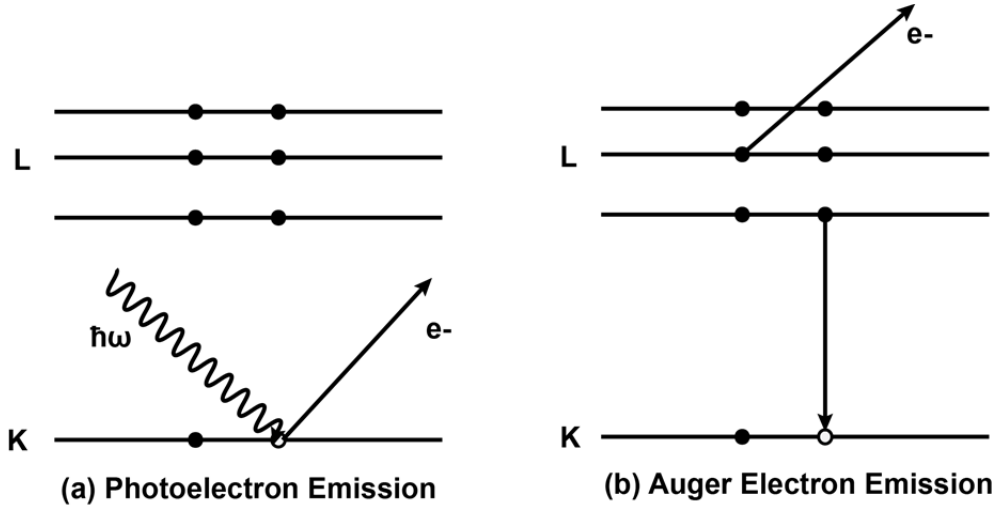

Fig. 2-3 Two typical electron emission processes detected in XPS. (a) Photoelectron emission; (b) Auger electron emission.

The generation of the Auger electrons is more complicated. When a core electron is ejected from an atom, leaving a vacancy in the core shell, electron in higher energy level will fall into the vacancy, release the energy difference between this two energy level. If this energy is transferred to another higher energy level electron, the electron can also be ejected from the atom/solid, calling Auger electrons. The energy of the Auger electron more complicated, since the Auger process is not observed in the thesis, we are not going into detail about this.

The energy of electron in XPS is not high enough, as a result, electron generated from the inside of the sample is not able to escape the solid, the detection depth of XPS is restricted to the surface layer up to a depth of 5 nm.

The chemical shift in XPS provides valuable information about the change of local chemical environment and formal oxidation state of the element on few the surface atomic layers (several nanometers) of the sample[3]. With the help of the established data of XPS databases, like LaSurface and NIST, together with the knowledge of the impact from oxidation state and surrounding atoms, the surface chemistry of the sample can be precisely analysed. The

quantification of surface elements in different states is made by calculating the area of the correlated peaks after the subtraction of the background using professional software, such as CasaXPS.

In this thesis, XPS characterisation was carried out on a Scienta ESCA-300 XPS spectrometer equipped with a rotating Al anode (1486.6 eV). The energy scale was calibrated to the Au $4f_{7/2}$ peak at 83.95eV. CasaXPS software was employed in data analysis. The experimental data were fitted and decomposed into single peak components using Gaussian-Lorentzian curves and Shirley background functions provided by the software.

2.3 Nitrogen Adsorption

N_2 adsorption is a powerful tool for the determination of the surface area and pore size distribution of the solids. Since most of the samples are not reactive to N_2, the adsorption of N_2 on solid surface is commonly considered as a pure physical process[4]. The adsorption isotherm is a plot of the amount of the N_2 adsorbed (c) against the relative pressure (p/p_0), which generally starts from a point very close to 0 to a point close to 1. The lowest relative pressure depends on the vacuum level that the equipment can reach. One of the most standard and widely used procedures for the determination of the specific surface area of the materials from N_2 adsorption is Brunauer–Emmett–Teller (BET) theory[5], which is named after the surnames of the three scientists who established this theory in 1938. BET theory adopts a multiple layer physical adsorption model of the adsorbates on material solid surface. The equation can be expressed as follow,

$$\frac{1}{v(p_0/p-1)}=\frac{c-1}{v_m c}\frac{p}{p_0}+\frac{1}{v_m c},$$

where p and p_0 are equilibrium pressure and saturation pressure of nitrogen at measurement temperature (N_2 can also be replaced by other non-reactive adsorbates for some specific purposes), v and v_m are adsorption quantity and monolayer adsoption quantity, respectively, and c is the BET constant. A linear relationship between $1/[v(p_0/p-1)]$ and p/p_0 is generally maintained in relative pressure (p/p_0) range from 0.05 to 0.35. Therefore, the BET plot of $1/[v(p_0/p-1)]$ versus p/p_0 is chosen to be in this pressure range. The value of monolayer adsorption quantity (v_m) and BET constant (c) can be expressed in term of the slope (A) and y-intercept (I) in following equation,

$$v_m = \frac{1}{A+I} \ ,$$

$$c = 1 + \frac{A}{I},$$

and the specific surface area (S_{BET}) is calculated by,

$$S_{BET} = \frac{v_m N s}{aV} \ ,$$

where v_m is calculated according equations above and in unit of volume, N is Avogadro's number, s is the cross section of the adsorbates (0.162 nm^2 for nitrogen), a is the mass of the sample and V is the molar volume of the adsorbed gas (N_2).

In this thesis, the measurements of BET surface area were carried out on a Micromeritics Tristar 3020 equipment with nitrogen at a constant temperature of 77K. A 0.1-0.2 g of sample was generally used in measurements. Before the measurements, samples were degassed at 120 ^oC under vacuum (10^{-3}~10^{-5} mbar) over night.

2.4 Transmission Electron Microscope (TEM)

The capability of transmission electron microscope (TEM) for direct observation of the samples at sub-micron to atomic (angstrom) level makes TEM an important technique for material science[6].

The high resolving power of TEM is the result of the short wavelength of the accelerated electrons. The electron beam used in TEM is generated by an electron gun, where electrons are accelerated under an electrostatic field of several hundreds of kilovolts, which gives the electrons of the corresponding energy, and a wavelength which is several hundreds of thousand times shorter than that of visible light, according to de Broglie equation. The electron beam is controlled by a set of electrostatic and electromagnetic lenses and metallic apertures via a highly precise mechanical and computerised system. The functions of these electro-lenses are similar to the lenses in optical microscope, but more complicated. The electron beam is transmitted through an ultrathin specimen, interacting with the specimen, magnified, focused, and finally, the image is formed on a fluorescent screen, recorded by photographic film or by an electron sensitive CCD camera. The later is most commonly used in today's TEM due to its higher efficiency and better accessibility.

High-resolution transmission electron microscope (HRTEM) allows scientists to study materials at sub-nanometer level. In this mode, the lattice of a crystal or the amorphous structure of the non-crystalline samples can be easily observed, which provides very detailed visual information that cannot be obtained by other instruments.

Besides its direct imaging ability, there are also some other functions on TEM, like select area electron diffraction (SAED), and energy-dispersive X-ray spectroscopy (EDS), if equipped with relevant functional units. When TEM operates in electron diffraction (ED) mode, the beam is focused on a very small area of the specimen, and a diffraction pattern from the selected area is obtained. The EDS is capable to quantitatively analyse the element composition of the selected area. It detects and analyses the characteristic X-rays emitted by particular atoms from the electron-illuminated area. The uniqueness of the X-rays generated from different elements is essential for EDS analysis. Quantification is based on the intensity of X-rays and the relative intensity from the standard database.

The TEM and HRTEM studies in this thesis were based on a JEOL JEM-2011 TEM instrument, equipped with a LaB_6 filament as electron source, and the accelerating voltage was 200 kV. Sample was dispersed in acetone under sonication, dropped onto SPI® holey carbon coated copper grids, and then transferred into TEM chamber after drying and loaded onto the grid holder. The TEM and HRTEM images were recorded by a Gatan CCD camera in digital format.

2.5 Scanning Electron Microscope (SEM)

Scanning electron microscope (SEM), like TEM, also exploits electron beam as its “light source”, but relies on different principle and provides different information. The SEM image generally contains the surface topography of the sample and information about the sample composition (Depend on the detectors equipped) [7].

A SEM utilizes low energy electron beam, ranging from several hundreds eV to several tens KeV. It works by scanning the sample with a focused electron beam. When the electron beam hits the sample, it produces different signals, including secondary electrons (emitted by atoms the excited by the electron beam), backscattered electrons, transmitted electrons, X-rays, light, current and *etc*. The basic SEM mode works by the detection of the secondary electrons. The signal of the secondary electrons is captured by the secondary electron detector, which is equipped on the all SEMs, and then analysed and reconstructed into a visualized image by

computer system. A SEM image is capable to reveal the sample surface in a very detailed resolution of less than 1 nm, when the instrument is equipped with a field emission gun.

Other signals can also be detected and analysed, if the required detector is equipped. For example, when an energy dispersive X-ray spectroscopy (EDS) is equipped, it can also perform X-ray microanalysis. The principle and function of the EDS on SEM is the same as that on TEM.

SEM analysis in this thesis was carried out on a JEOL JSM-6700F FE-SEM using SEI (secondary electron image) mode. Sample was loaded onto the sample holder by attaching it on the conductive carbon tape.

2.6 Fourier Transform Infrared (FTIR) Spectroscopy

A Fourier transform infrared (FTIR) spectroscopy is a technique, which collects the infrared spectrum of a sample with a high resolution over a wide spectral range simultaneously. Alhough an FTIR spectrometer works in a totally different way comparing to the normal infrared (IR) spectrometer due to the different physical methods exploited to obtain the spectrum, the fundamental physical principal and spectroscopic information are entirely the same.

An IR beam, whose wavelength is shorter than that of the visible light, can be absorbed by the sample. An (FT)IR spectrum is typically a plot of the infrared light transmittance or absorbance *vs.* the frequency of the IR radiation, which is the generally expressed as wavenumber (a reciprocal wavelength, with unit symbol of reciprocal centimeters, cm^{-1}). The IR absorption of the molecules, and solids are characteristic frequencies of their structures and functional groups[8]. This absorption is called resonant absorption because the radiation absorbed matches the transition energy of the bonds, groups, or structures that vibrates.

Lots of molecules and functional groups have different vibration (normal) modes. Only those vibrations that change the dipole moment of the molecule or group are IR sensitive. Each IR sensitive vibration gives a distinctive absorption band. IR spectrum is generally used for structural identification because a certain functional group gives rise to one or a couple of characteristic IR absorption bands in both peak intensity, shape, and position, which shifts within a limited range due to the impact of the neighbouring structures. These characteristic absorption bands are listed in most of the chemistry handbooks, which help scientists to identify the functional groups in molecules or structures in solids. A more reliable approach

of the species identification is by the comparison of the unknown spectrum with the spectrum of standard sample from experiments or database. It is noteworthy that amorphous substance, which is not detectable in PXRD and some other techies, is mostly detectable and identifiable by (FT)IR technique. This makes (FT)IR spectroscopy a very important technique in modern chemistry and material science.

A normal IR spectrometer works in energy dispersive way, *i.e.*, when it collects the spectrum, the instrument scans over the required frequency from one side to another and records the transmitted beam intensity step by step. The modern FTIR spectrometer exploits a Michelson interferometer and polychromatic IR light source and obtains an interferogram, which will result in the same IR spectrum as the one collected on the normal IR spectrometer after Fourier transformation[8]. This new technique used on FTIR spectrometer allows it to measure the IR spectrum in a very short time.

All FTIR spectra in this thesis were collected on a Nicolet 6700 FTIR spectrometer (Thermo Fisher Scientific) in an N_2-filled glove box using transmission mode. The samples were made by cesium iodide (CsI) pellet method, in which adequate amount of sample was mixed with spectroscopic grade CsI, grounded finely, and pressed into a transparent pellet with a manual pelletizer. Cesium iodide was used instead of the regular potassium bromide (KBr) due to its a wider IR transparent window.

2.7 Raman and Surface Enhanced Raman Spectroscopy (SERS)

Similar to IR spectroscopy, Raman spectroscopy is also a technique working in the IR region, and it is also able to obtain the information about the vibrational modes in a system. However, a Raman spectrum is a scattering spectrum based on Raman (inelastic) scattering of the monochromic light.

When a sample is illuminated by a light beam, there will be various interactions between the radiation and the substance, including absorption, elastic scattering (also known as Rayleigh scattering, in which the frequency of the scattered light is the same with the original light), and inelastic scattering (Raman scattering, in which the wavelength of the scattered light is either shorter or longer than the excitation beam). A Raman spectrometer works by the detection of the photons from Raman scattering[9]. A typical Raman spectrum is a plot of scattering intensity (on y-axis) versus Raman shift (on x-axis), which is calculated from the difference between the wavenumber (generally in unit of cm^{-1}) of the scattered light and that of the excitation source. Since signal of the Raman scattering is generally very weak, hence a

special detection system is equipped and a laser beam is always employed in the Raman spectrometer as the excitation light source, which also grants the best monochromic property.

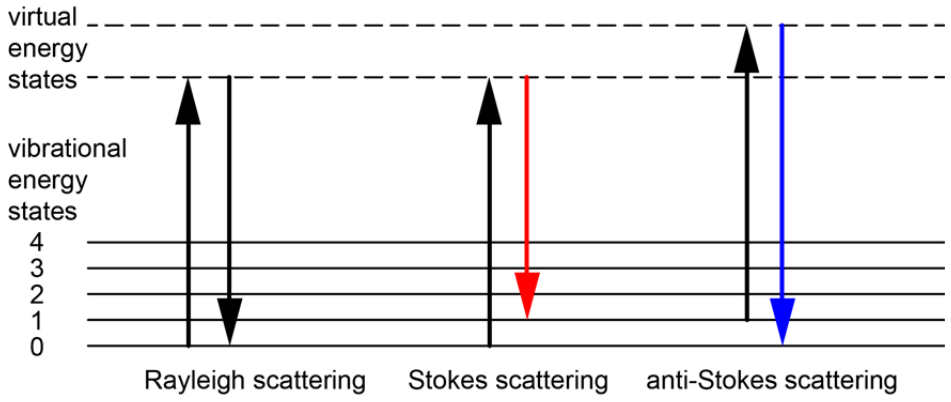

Fig. 2-4 Schematic Illustration of Raman and Rayleigh Scattering

Fig. 2-4 illustrates the mechanism of Raman scattering. A laser photon excites the sample molecule from the ground rotational vibrational state or excited state to a virtual energy state (an intermediate state that has a very short life time), after a very short period, it jumps back to ground or excited state randomly by releasing a photon. If the resulting state and the initial state are the same, it is called Rayleigh scattering. If not, it is Raman scattering. In Raman scattering, when the energy of the finial rotational-vibrational state is higher than the initial state, the energy of the resulting photon becomes lower, which is Stokes scattering, in the other case, the energy of the resulting photon becomes higher, called anti-Stokes scattering. Each of the vibration modes, which changes the polarisibility of the molecule or structure, will have a response in the Raman spectrum. Some vibrations that it not IR active can be Raman active, and *vice versa*.

A solid will also have its characteristic Raman spectrum according to the normal vibration modes that satisfy the polarisibility's rule, and the sensitivity of the Raman for solids is high enough to effectively identify some minor impurities from a sample. Particle size has little impact towards most of the peak position[10], which makes Raman suitable for the impurity detection in extremely small-sized particles, *e.g.*, in Chapter 3, Raman is applied to examine the phase purity of sub-3nm sized TiO_2(B).

The Raman characterisation was carried out on a Renishaw InVia Raman microscope system (Renishaw, Wottonunder-Edge, UK).

Surface enhanced Raman spectroscopy (SERS) is an advanced technique, which exploits the fact that the intensity of Raman scattering will be strongly magnified on roughened gold or

silver surface due to the surface plasma effect of the metal surface[11]. It allows the scientists to identify the surface species in ppm scale, making it a extremely useful technique in a lot of cutting edge studies.

Both Raman and SERS can be used as *ex-situ* or *in-situ* techniques. The *in-situ* SERS was employed in the thesis for the examination of the surface O_2^- species in Chapter 5. The experiment was carried out on a laboratory-made spectrometer, for the details, please see Chapter 5.

2.8 Battery Test

Various methods are used in research and industry in order to understand different aspects of the battery performance, such as capacity, cycleability, and safety. One of the most widely used approaches is galvanostatic cycling (charge and discharge at a constant current) at a constant temperature. This was also applied in the thesis for battery test. Since the main purpose of the electrochemical study in the thesis is to understand the lithiation/de-lithiation property of the synthesised materials themselves instead of the engineering problem of the whole battery construction, coin type cells were used, due to their low cost, less material consumption, convenience to assemble and handle, and good experimental repeatability. The coin cell kits were purchased from the National Research Council, Canada (25 mm in diameter by 2.5 mm in height), and Fig. 2-5 shows an exploded view of the coin cell. All cell parts were dried before usage.

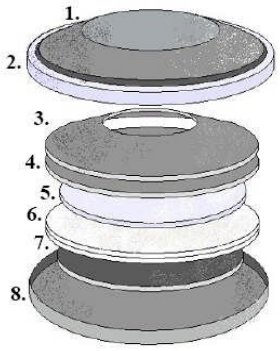

Fig. 2-5 Exploded View of A Coin Cell. 1. Coin cell top part. 2. Sealing grommet. 3. Spring. 4. Spacer. 5. Lithium anode. 6. Separator 7. Sample cathode disc. 8. Coin cell bottom part.

A typical procedure of coin cell assembling is described as follow: the sample is firstly mixed with Kynar® 2801 (a polyvinylidene fluoride base co-polymer, Arkema), and Super P

(TIMCAL) carbon black in a selected weight ratio. Acetone (Aldrich, > 99%) is used to disperse the mixture under magnetic stir for 8-12 h, until viscous slurry forms. Then a slurry film of about 50 μm thickness is cast onto a copper foil (purity 99.95+%, electrodeposited, thickness 0.017 mm, Advent Research Materials Ltd) using a doctor-blade technique. After the solvent evaporates at room temperature, the foil is transferred into a vacuum oven and further dried at 80 ^{o}C for 1 h. Then the foil is cut into small discs (13 mm in diameter) using a coin cell puncher and the discs were dried in a Büchi® oven at 80-100 °C for 12 h under vacuum. The sample discs are later transported into an Ar-filled MBraun® glovebox (H2O, O2 < 0.1 ppm) for the battery assembling. A sample disc is first placed on a coin cell bottom part with the active material coated side facing upward, and then two pieces of glass fibre separators (grade GF/F, binder-free, Whatman®) are placed on the top of the sample disc, 10-12 droplets of electrolyte LP30 (1M $LiPF_6$ in 1:1 v/v ethylene carbonate: dimethyl carbonate, Merck®). Then a piece of lithium metal (99.9%, cut from lithium ribbon, Aldrich), a stainless-steel disc, a spring and a coin cell top part with a plastic sealing grommet are placed on top of each other in the described order. Finally, the cell is sealed with a coin cell pressing system inside of the glovebox.

A MACCOR® 4200 multichannel battery test system were used to collect the battery cycling data. All tests were carried out in a 30 °C incubator. The batteries are generally allowed to rest for at least 4 h before the test start, in order to reach equilibrium between the electrode and electrolyte.

2.9 Cyclic Voltammetry (CV)

Cyclic voltammetry (CV) is a typical electrochemical technique, which is generally applied to study the redox behaviour of the analytes in solution. It provides valuable information, such as the standard potential of a redox couple, reversibility of a redox reaction, intermediate species, electron transfer kinetics, and so on[12].

The measurement is carried out using a three-electrode electrochemical cell, in which the working, counter, and reference electrodes are placed in a correct geometry. And the voltage scans linearly from the open circuit potential to the target potential, then ramps in the opposite to another set potential, or returns to the initial potential. This process can be repeated for a lot of times. A cyclic voltammogram is created by plotting the current at the working electrode against the potential applied on the working electrode versus the reference electrode. A typical voltammogram is shown in Fig. 2-6.

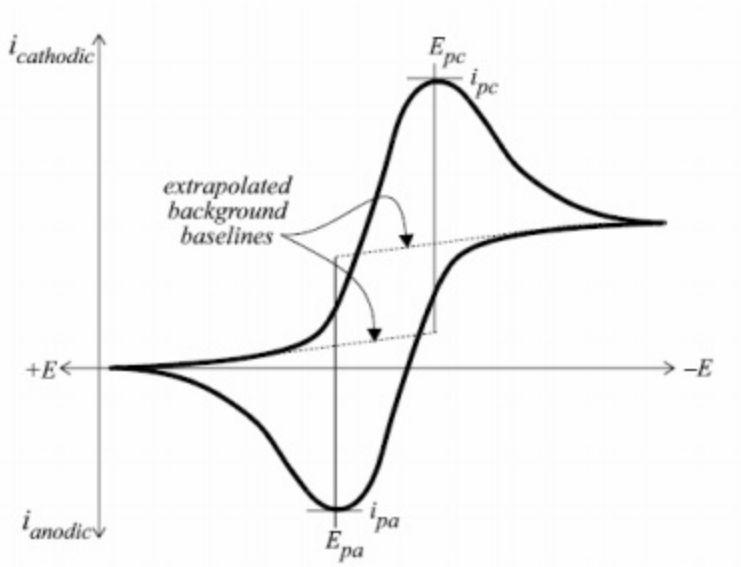

Fig. 2-6 A typical cyclic voltammogram. E_{pc} is the peak cathodic potential, E_{pa} is the peak anodic potential, i_{pc} is the peak cathodic current (with respect to the extrapolated background baseline), i_{pa} is the peak anodic current (with respect to the extrapolated background baseline). From ref. 12.

A reversible redox couple is characterised by,

$$\frac{i_{pa}}{i_{pc}} = 1 \ ,$$

and an ideal system satisfies,

$$E_{pa} - E_{pc} = \frac{56.5}{n} mV \ ,$$

where n is the number of electrons transferred in the redox process.

The standard potential E^o is calculated by,

$$E^o = \frac{E_{pa} + E_{pc}}{2} \ ,$$

In the thesis, CVs were measured on a BioLogic® VMP3 workstation using a three-electrode electrochemical cell in Chapter 5 in order to study solution electrochemistry of O_2 reduction. The counter and reference electrode are specified in the relative chapter.

Reference

1. Bragg, W.H. and W.L. Bragg, *The Reflection of X-rays by Crystals.* Proceedings of the Royal Society of London A: Mathematical, Physical and Engineering Sciences, 1913. **88**(605): p. 428-438.
2. Kuzmany, H., *Solid-state spectroscopy: an introduction*. 2009: Springer Science & Business Media.
3. Watts, J.F., *Special Issue Surface Science Techniques X-ray photoelectron spectroscopy.* Vacuum, 1994. **45**(6): p. 653-671.
4. Rouquerol, J., et al., *Adsorption by powders and porous solids: principles, methodology and applications*. 2013: Academic press.
5. Brunauer, S., P.H. Emmett, and E. Teller, *Adsorption of Gases in Multimolecular Layers.* Journal of the American Chemical Society, 1938. **60**(2): p. 309-319.
6. Williams, D.B. and C.B. Carter, *The Transmission Electron Microscope*, in *Transmission Electron Microscopy: A Textbook for Materials Science*. 1996, Springer US: Boston, MA. p. 3-17.
7. Goldstein, J., et al., *Scanning electron microscopy and X-ray microanalysis: a text for biologists, materials scientists, and geologists*. 2012: Springer Science & Business Media.
8. Stuart, B., *Infrared Spectroscopy*, in *Kirk-Othmer Encyclopedia of Chemical Technology*. 2000, John Wiley & Sons, Inc.
9. Colthup, N., *Introduction to infrared and Raman spectroscopy*. 2012: Elsevier.
10. Gouadec, G. and P. Colomban, *Raman Spectroscopy of nanomaterials: How spectra relate to disorder, particle size and mechanical properties.* Progress in Crystal Growth and Characterization of Materials, 2007. **53**(1): p. 1-56.
11. Haynes, C.L., A.D. McFarland, and R.P.V. Duyne, *Surface-enhanced Raman spectroscopy.* Analytical Chemistry, 2005. **77**(17): p. 338 A-346 A.
12. Bard, A.J. and L.R. Faulkner, *Electrochemical methods: fundamentals and applications*. Vol. 2. Wiley New York.

Chapter 3 Synthesis of Anatase Nanosheets And Their Application As Anode Materials For Lithium Ion Battery

Anatase nanosheets of different thickness were synthesized by solvothermal reactions. Powder X-ray diffraction (PXRD) and TEM were employed to measure their thickness and determine their morphology. A series of factors that have impacts on the thickness and morphology of the nanosheets and will be discussed. By tuning the synthesis conditions, nanosheets with a thickness of *ca.* 3 nm and a perfect rectangular shape were prepared, denoted as 3nm-NS. After calcination at different temperature, the nanosheets were explored as anode materials for Li-ion batteries. The 3nm-NS was also subjected to a surface treatment with H_2O_2/NH_3. The variation of its surface condition was analysed by FTIR and XPS. This sample exhibited an initial capacity of 322 mAh/g, and the capacity remained at 201 mAh/g even after 100 cycles at a rate of 170 mA/g, higher than most of the anatase materials reported.

3.1 Experimental

3.1.1 Synthesis of Anatase Nanosheets.

Anatase nanosheets were synthesized by a modified solvothermal reaction, reported by X. Yang et al[1]. Typically, 0.4 ml of hydrofluoric acid (HF, 49-51%, Alfa Aesar), 5-6 ml of titanium (IV) butoxide ($Ti(OBu)_4$, ≥97%, Sigma-Aldrich), and 0-5 ml of tert-butanol (t-BuOH, ≥99.7%, Sigma-Aldrich) were mixed in a 50 ml Teflon-lined stainless steel autoclave, and kept at 160 ^oC for 24 h in an electric oven. After cooling down to room temperature naturally, the solid was separated using a centrifuge and washed several times with absolute ethanol and distilled water. In order to get rid of any possible HF residue, the sample was then soaked in 10 ml of 0.1 M ammonia (NH_3) solution for 5 min, and finally rinsed 3 times with distilled water repeatedly. After drying at 100 ^oC overnight, the sample was grounded and calcined at a specific temperature for 4 h in dry air with a ramping rate of 10 ^oC/min.

3.1.2 Surface treatment

The nanosheets synthesized using 5 ml of $Ti(OBu)_4$, 0.5 ml of t-BuOH and 0.4 ml of HF were subjected to the surface treatment in order to remove the surface fluoride and organic residues left after synthesis. This was done by washing the sample first with NH_3 and then again with 10 ml of an aqueous solution containing 6% H_2O_2 and 0.1 M NH_3. The resulting material was then rinsed several times with distilled water, dried at 100 ^oC overnight, ground and then calcined at 350 ^oC for 4 h in dry air with a ramping rate of 10 ^oC/min.

3.1.3 Battery test.

The electrochemical performance of the anatase nanosheets was evaluated in a coin cell. The cell was assembled in an Argon-filled glovebox according to the procedure introduced in Chapter 2. The ratio of anatase nanosheets: Super P: Kynar was 8:1:1. And the cell was cycled between 3-1 V at specific rates.

3.2 Result and Discussion

We will begin from the synthesis, examining the factors that have impacts on the morphology and dimensions of the anatase nanosheets, including the ratio of the reagents, and annealing. By varying the synthesis condition, the anatase nanosheets with regular shape and uniformed size distribution has been achieved. These uniform nanosheets, heated up to different temperature, or subjected to surface treatment, were later explored as anode materials for Li-ion batteries. In this section, we will see the size and surface dependence of the capacity, and the reasons will be discussed respectively.

3.2.1 Thickness and morphology of anatase nanosheets

Estimation of the thickness of the nanosheets. One of the methodologies used in this chapter is to characterise the particle size of the nanosheets using powder x-ray diffraction data (For more details, see Chapter 2). The thickness and morphology of anatase nanosheets are controlled by the ratio of $Ti(OBu)_4$: HF: t-BuOH. The thickness of the nanosheets was estimated from the full width at half maximum (FWHM) of the broadest (004) powder diffraction peak centred at 37.8^o using the Scherrer equation (see Chapter 2). Even though this broad peak comprises 3 distinct reflections (103, 004, and 112), the difference in their

intensities and the anisotropic property of the nanosheets renders it feasible to disregard the contributions from the 103 and 112 reflections when considering the peak width, since the calculated 004 reflection is 4 fold more intense than the other two and is the sole orientation (preferential orientation) of the nanosheets associated with significantly reduced crystallite size (details are provided in the following discussion). Finally, the morphology of the nanosheets was investigated by TEM and the thickness was verified.

The ratio of $Ti(OBu)_4$ to HF. The synthesis of nanosheets involves the addition of several compotents the quantities of which influence the resultant morphology. In order to illustrate the impact of the ratio of $Ti(OBu)_4$ to HF, the amount of $Ti(OBu)_4$ varied from 5 ml to 6 ml without the addition of t-BuOH.

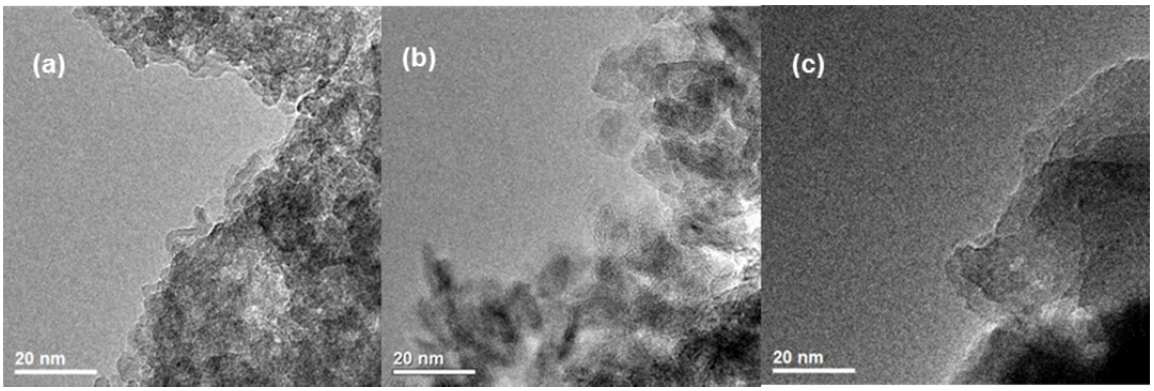

Fig. 3-1 TEM images of the anatase nanosheets without the addition of tert-butanol: (a) 5 ml $Ti(OBu)_4$, (b) 5.5 ml $Ti(OBu)_4$, (b) 6 ml $Ti(OBu)_4$

The morphologies of different samples are revealed by TEM in Fig. 3-1. The nanosheet morphologies are clearly recognised from the edges of the samples, although severely agglomerated. It seems that the nanosheets grow in length and width with more $Ti(OBu)_4$, however, the thickness of these nanosheets can hardly be obtained by direct TEM observation due to the agglomeration. Hence, the thickness of these nanosheets was only estimated from their PXRD patterns. It is worth noting that as a result of bending and distortion (See Fig. 3-1), the coherent length of these nanosheets is significantly reduced, leading also to the broadening of the associated 200 peak. Their powder diffraction patterns are presented in Fig. 3-2.

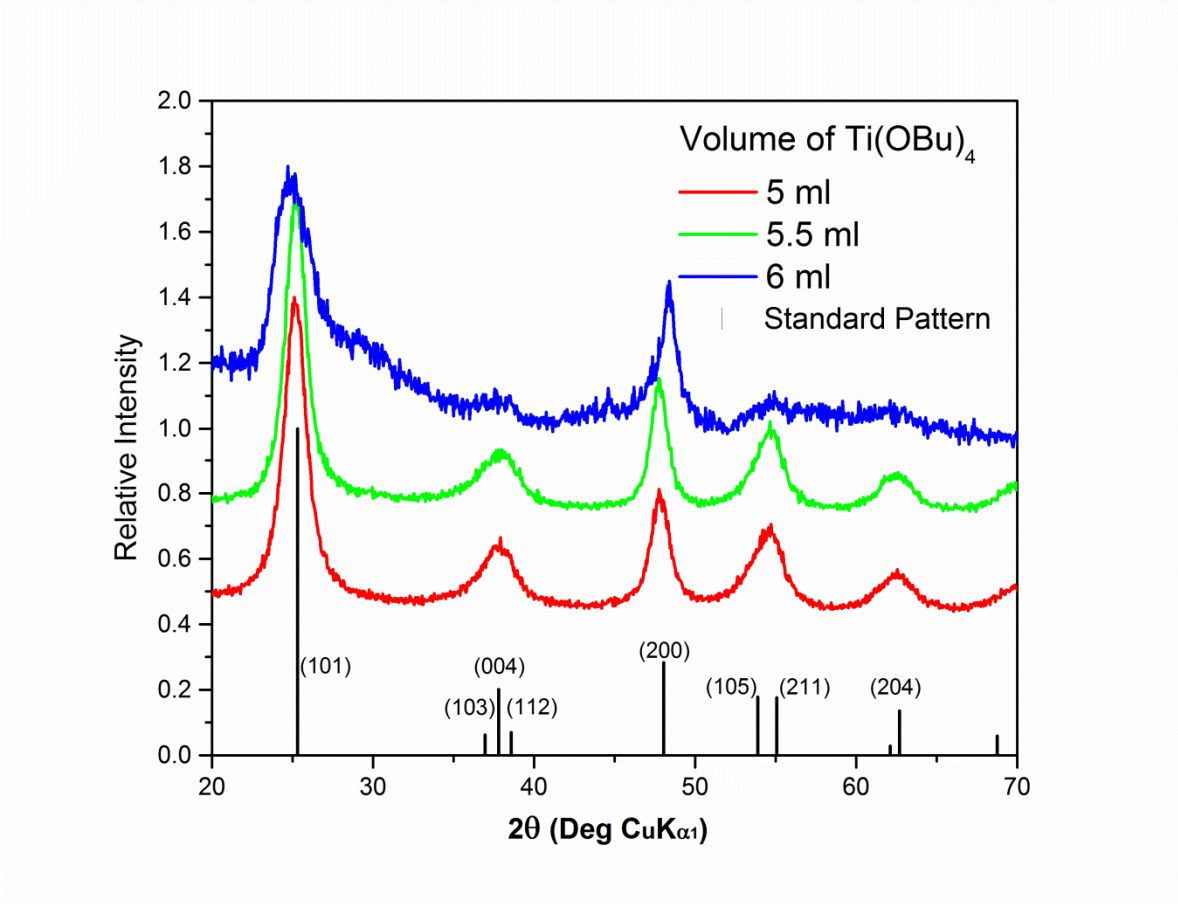

Fig. 3-2 PXRD of patterns of the anatase nanosheets without the addition of tert-butanol. The volume of $Ti(OBu)_4$ varies from 5 ml to 6 ml.

All these patterns were identified as anatase (*I4₁/amd*). The increased FWHM of the 004 reflection peak implies a reduced crystallite size along c-axis, the average thickness of nanosheets changes from 3.38 nm to 3.14 nm, when the amount of $Ti(OBu)_4$ increased from 5 ml to 5.5 ml . When the volume of $Ti(OBu)_4$ increased to 6 ml, the 004 peak became very weak, suggesting that the related thickness became smaller. However, the 200 peak shifted from 48.0^o to 48.9^o, indicating that the d-spacing of (001) plane is smaller than the standard anatase sample. Although a higher ratio of $Ti(OBu)_4$ contributes to slightly reduced nanosheet thickness, it will also cause severe distortion. In order to obtain high quality anatase nanosheets, high volume of $Ti(OBu)_4$ should be voided in the following synthesis.

The effect of t-BuOH. For the preparation of the TiO_2 nanosheets in this section, the volume of HF and $Ti(OBu)_4$ was fixed at 0.4 ml and 5 ml, respectively. And the volume of tert-

butanol (t-BuOH) varied from 0 to 2 ml. By adding t-BuOH, regular ultrathin anatase nanosheets were obtained.

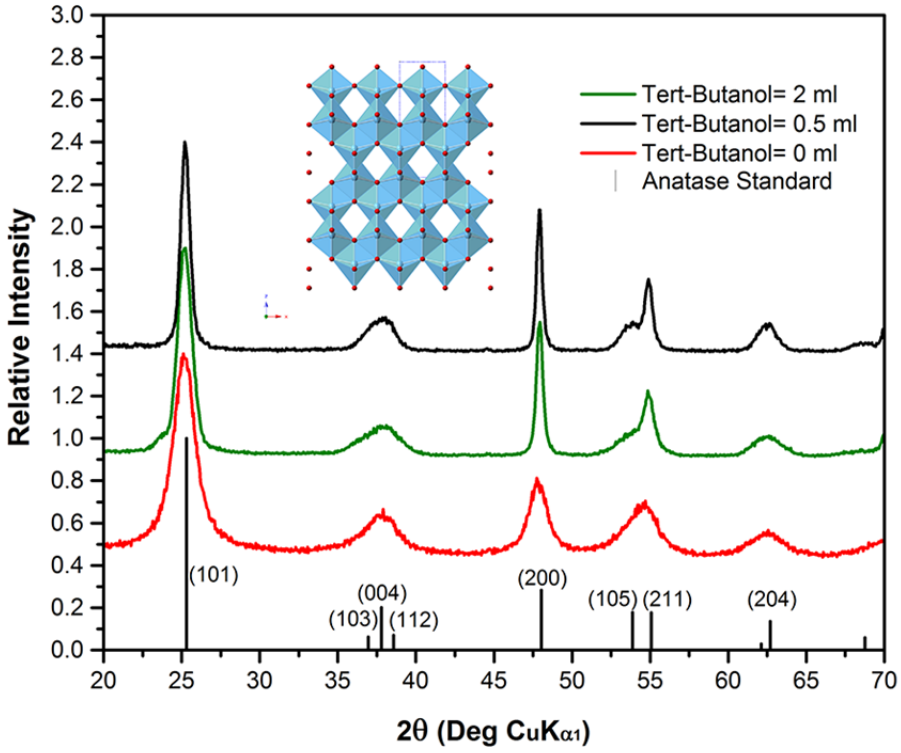

Fig. 3-3 PXRD patterns of the anatase nanosheets with the amount of tert-butanol changing from 0 to 2 ml. The inset is the (010) view of the anatase crystal structure.

The PXRD patterns are presented in Fig. 3-3. The significant narrowing of the 200 peak has been observed after the addition of t-BuOH, indicative of a considerable increase in the coherent length along [200] direction. This has been confirmed by TEM. Fig. 3-4 presents the top and side view of the nanosheets. After the introduction of t-BuOH, the shape of the anatase nanosheets changed dramatically from the irregular agglomerates (Fig. 3-4 (a) (b)) to a more uniform rectangular structure (Fig. 3-4 (c)-(f)).

The thickness and width of the nanosheets, calculated from Scherrer equation, are listed in Table 3-1, these values are in good agreement with TEM observation.

Table 3-1 The change of crystallite sizes along different directions measured by PXRD

Volume of Tert-butanol (ml)	Crystallite Sizes Along Different Directions (nm)*		
	<101>**	<001>	<100>
0	4.79	3.38	14.69
0.5	7.42	2.81	42.69
2	11.45	3.84	51.86

*The crystallite sizes are estimated according to the Scherrer equation $\tau = \frac{K\lambda}{\beta\cos(\theta)}$, K=0.9. For the detailed explanation, see Chapter 2.1

**<hkl> denotes the sets of all equivalent [hkl] directions that are related by symmetry

Interestingly, while the width of the nanosheets increases with more t-BuOH, the thickness of the nanosheets did not follow the same trend. The thinnest nanosheets were achieved when the volume of t-BuOH was 0.5 ml, and average thickness of the sample is 2.81 nm. The lattice fringe from the side view of HRTEM image (Fig. 3-4 (c)) is 0.237 nm in accordance with the d-spacing of anatase (004) (0.2378 nm), which confirms that the thinnest direction of the nanosheets is along c-axis of the crystal.

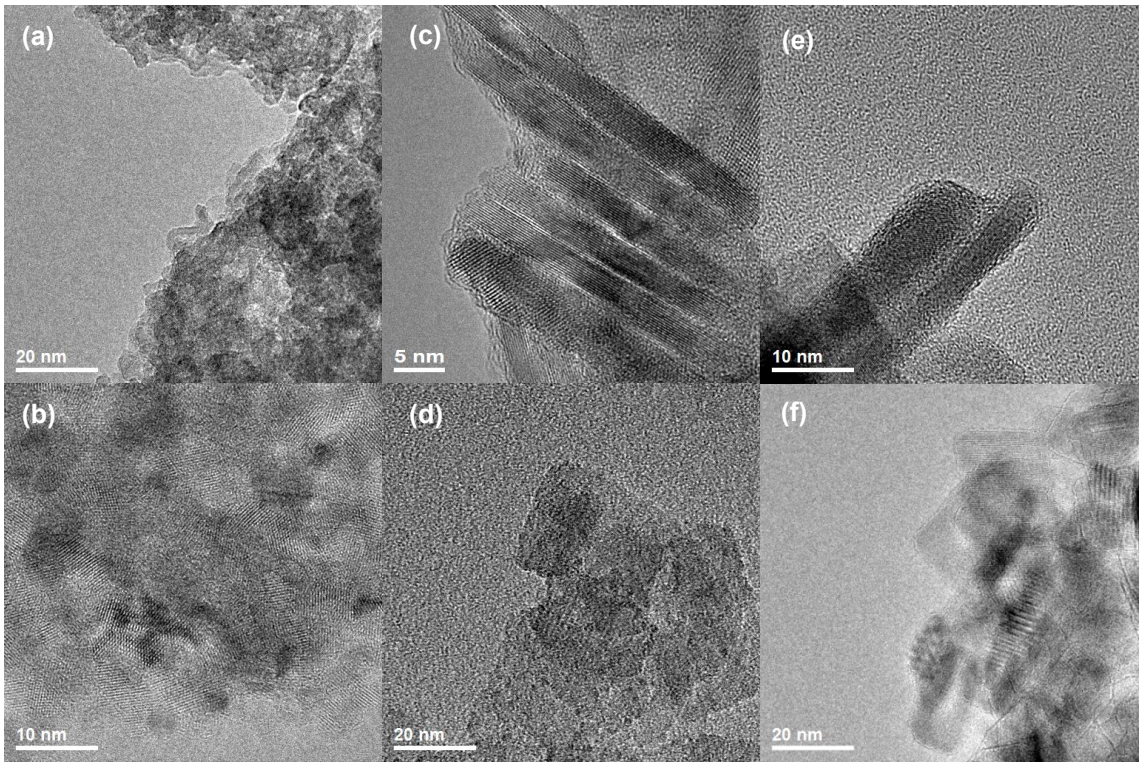

Fig. 3-4 TEM Images of anatase nanosheets prepared with different amount of tert-butanol. (a) (b) tert-butanol = 0 ml; (c) (d) tert-butanol = 0.5 ml; (e), (f) tert-butanol = 2 ml.

The result of adding t-BuOH is more complicated—the change of the shape, along with different effects on the size of the thickness and width. The mechanism of the nanosheets formation has been discussed in previous paper[2]. Fluoride serves as a capping agent, which bonds much stronger to the high energy {001} facets, suppressing the crystal growth along the [001] direction. Together with the fact that the (100) and (010) facets are symmetrically identical (usually denoted as {100} facets), crystal growth along a and b axis should be the same. Hence, the theoretical shape of the nanosheets should be rectangular with the same length along the [100] and [010] directions and a very limited thickness along [001] direction, like the images in Fig. 4 (c)-(e). It is possible that without t-BuOH, both the concentration and the viscosity of the reagents are too high for the growth of the perfect theoretical shape as there are only 2 reagents themselves in the reaction system, leading to the formation of the bended and distorted nanosheets. However, after the addition of t-BuOH, both the concentration and the viscosity were reduced, and the shape became regular and uniform.

In principle, the addition of t-BuOH dilutes the concentration of F^-, which should result in less F^- bonds formed to the facet of the anatase nanocrystal. Under this condition, the nanocrystals prefer to grow larger. This agrees with the increase of the size of nanosheets when the volume of t-BuOH changed from 0.5 ml to 2 ml. The inconsistency of the [001] size reduction when t-BuOH changed from 0 to 0.5 ml is possibly because the nanosheets grown without t-BuOH stacked together and the grain boundaries merged during solvothermal reaction.

The thinnest regular anatase nanosheets was synthesized with 5 ml of $Ti(OBu)_4$, 0.4 ml of HF, and 0.5 ml of t-BuOH. This was used in all further studies and was the only sample investigated electrochemically, denoted as 3nm-NS.

Calcination temperature. Another parameter which effects the resulting nanosheets is the heating temperature. Anatase is stable during the heating, no other TiO_2 phases are identified up to 400 ^oC (See Fig. 3-5). The thickness of the 3nm-NS grows with rising heating temperature, according to the narrowing of the (004) peak shown in Fig. 3-5. The thickness of the nanosheets were estimated to be 2.81 nm, 3.62 nm, 4.21 nm, and more than 7 nm, for the 3nm-NS, 300 ^oC, 350 ^oC, and 400 ^oC calcined samples respectively. It is worth noting that the

(103) and (112) peaks become visible in the 400 °C annealed sample, as the result of the significant narrowing of the (004) peak. The electrochemistry of these samples will be studied in a later section.

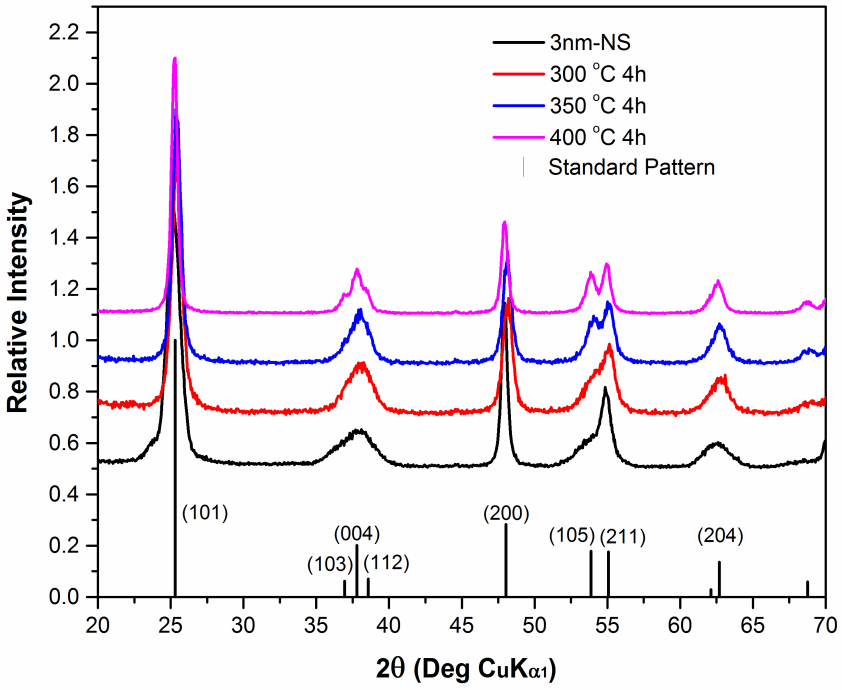

Fig. 3-5 The variation of the PXRD patterns at different calcination temperature

3.2.2 Surface Treatment

As we will see in Section 3.2.3, the capacity of these TiO_2 nanosheets was not as high as expected, hence, a surface treatment was applied to these nanosheets, due to a speculation that a cleaner and larger surface of the nanosheets might contribute to more capacity.

The process of the treatment has been described in the experimental section.

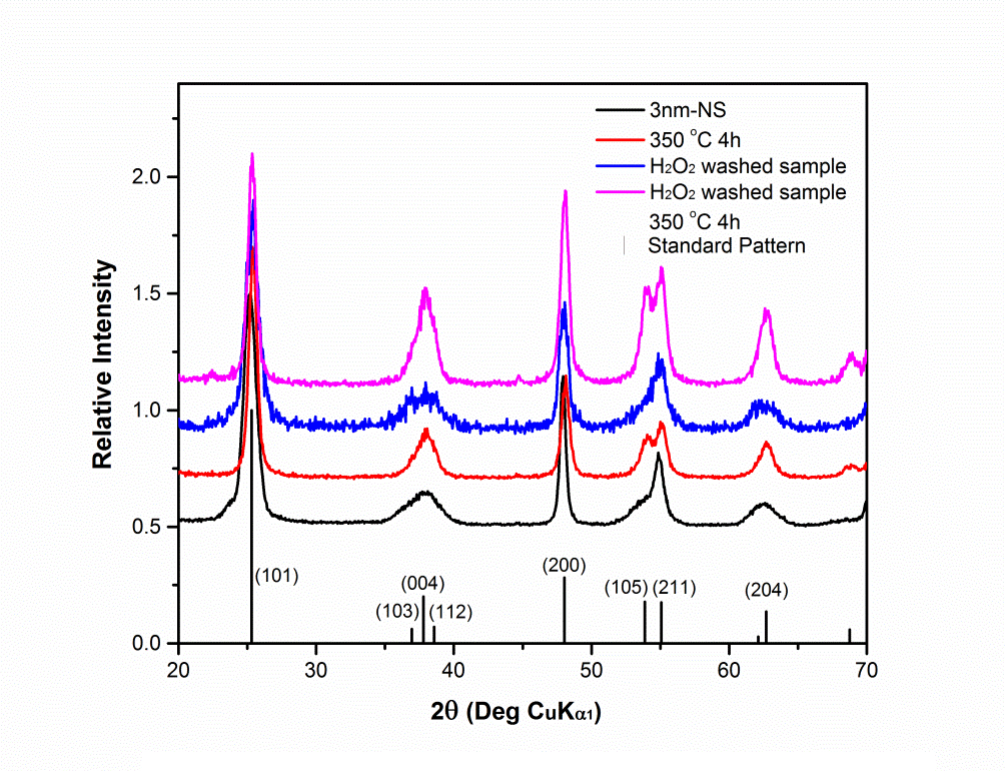

Fig. 3-6 PXRD patterns before and after surface treatment.

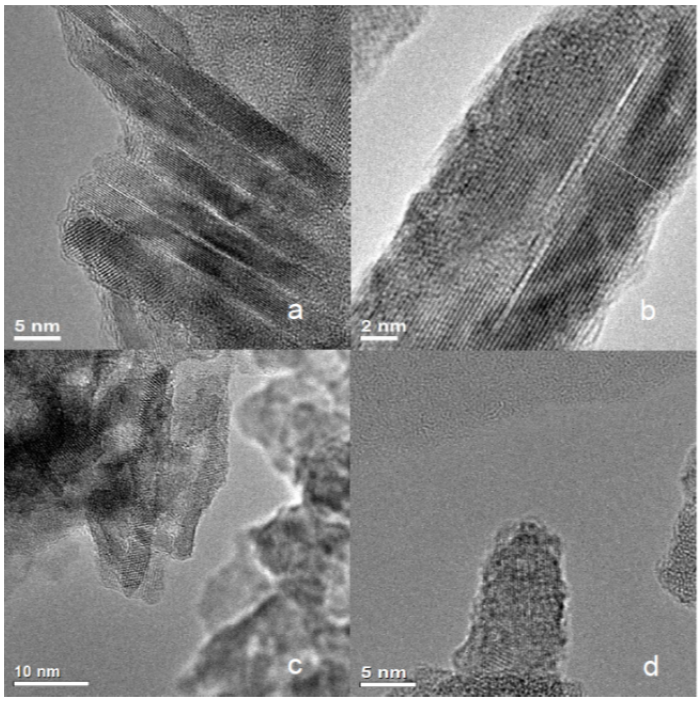

Fig. 3-7 The morphologies before and after surface treatment. (a) 3nm-NS; (b) 350 °C calcinated sample; (c) H_2O_2/NH_3 washed sample; (d) H_2O_2/NH_3 washed sample after calcination at 350 °C

The 3nm-NS before and after H_2O_2/NH_3 treatment are compared in this section. The PXRD patterns and TEM images are presented in Fig. 3-6 and Fig. 3-7, respectively. No obvious change of the size of the nanosheets was observed after the H_2O_2/NH_3 treatment according to the diffraction data and TEM images, but the surface of the nanosheets became roughened (See Fig. 3-7(c)), which implies that H_2O_2/NH_3 is corrosive towards the surface of the anatase nanocrystals. Another evidence that H_2O_2/NH_3 is corrosive towards the nanosheets surface is that the solution became yellow in colour during the H_2O_2/NH_3 treatment, which is a characteristic colour of Ti^{4+}-O_2^{2-} complex in basic solution. After calcination at 350 ^oC, the average thickness of the treated sample was estimated to be 4.68 nm (4-5 nm from TEM), while the pristine sample after calcination was 4.21 nm (4-5 nm from TEM). The thickness of the treated sample became larger than the untreated sample after annealing in the same condition as there was no surface layers to restrict grain growth, indicating that the amount of protective agents (surface organics and fluoride) on the surface of the anatase nanosheets is reduced after the wash of H_2O_2/NH_3.

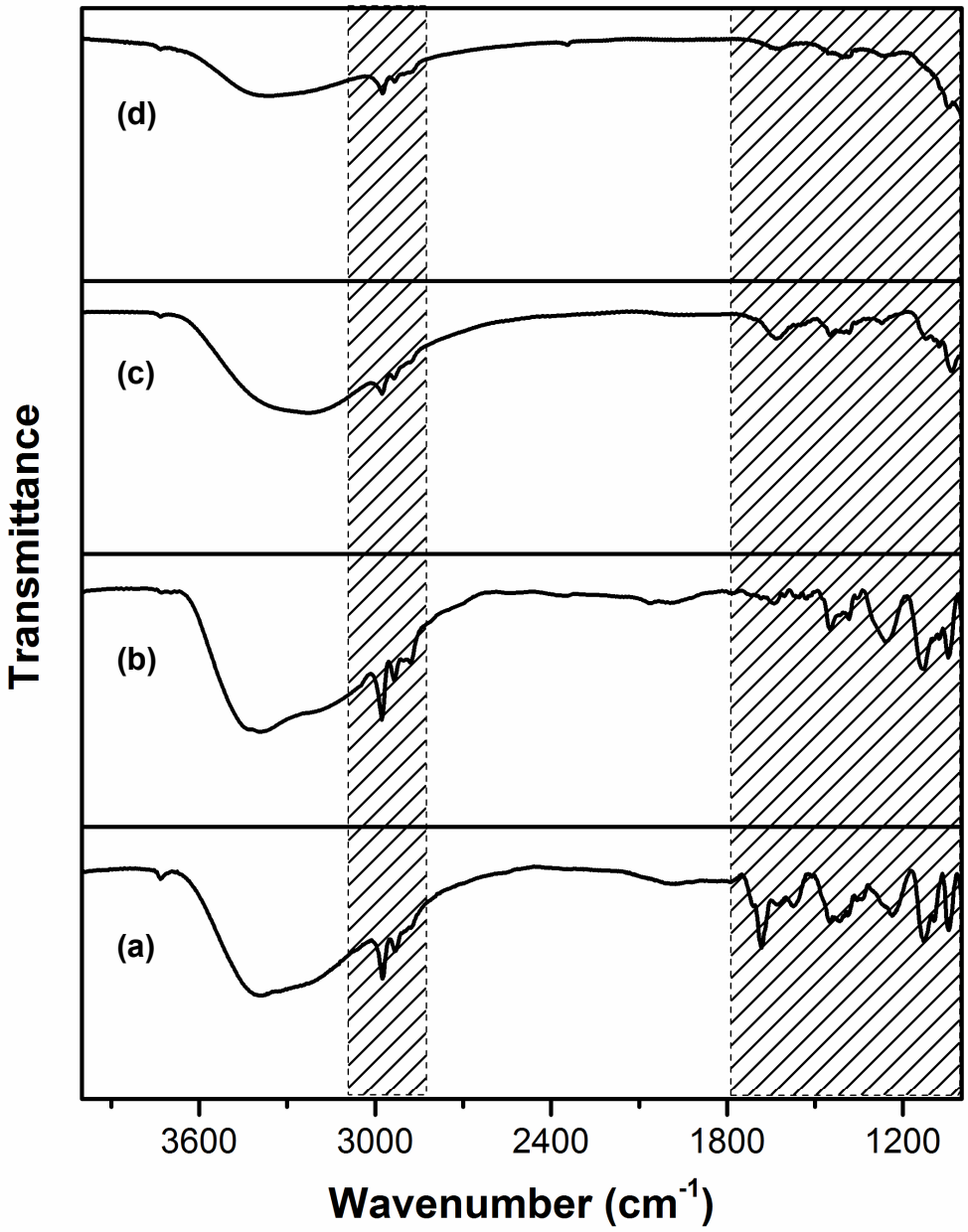

Fig. 3-8 FTIR spectra for 3nm-NS (a) H_2O washed sample; (b) H_2O washed sample after calcination at 350 ^oC; (c) H_2O_2/NH_3 washed sample; (d) H_2O_2/NH_3 washed sample after calcination at 350 ^oC. The shaded regions indicate organic residue. The scale of transmittance is from 20% to 100%

Removal of organics. The removal of surface organics was confirmed by FTIR (Fig. 3-8). The shaded regions in Fig. 3-8 imply the existence of organic species. The peaks in the region

of 3100-2800 cm^{-1} are due to the stretching of the C-H bonds, peaks in 1800-1100 cm^{-1} region are quite complicated, due possibly to the new organic compounds formed and adsorbed on the nanosheets surface during the solvothermal reaction. Accurate analysis of the organic species is not of the interest of this chapter. The information from weakening of the peaks and the smoothing of the 1800-1100 cm^{-1} regions is enough to be the evidence of the effective removal of the surface organics. Some of the surface organics are quite stubborn and cannot be effectively removed by direct heating under 350 ^{o}C (Fig. 3-8 (b)). However, the treatment of H_2O_2/NH_3 removes these organics readily due to its corrosive nature towards the anatase nanosheets. After calcination, no obvious organic peaks were identified. The existence of surface bonded and adsorbed $–OH/H_2O$ is revealed by the strong broad peak from 3600 cm^{-1} to 2800 cm^{-1}, the region of O-H stretching.

Removal of fluoride. The presence of fluorine was confirmed by XPS (Fig. 3-9).

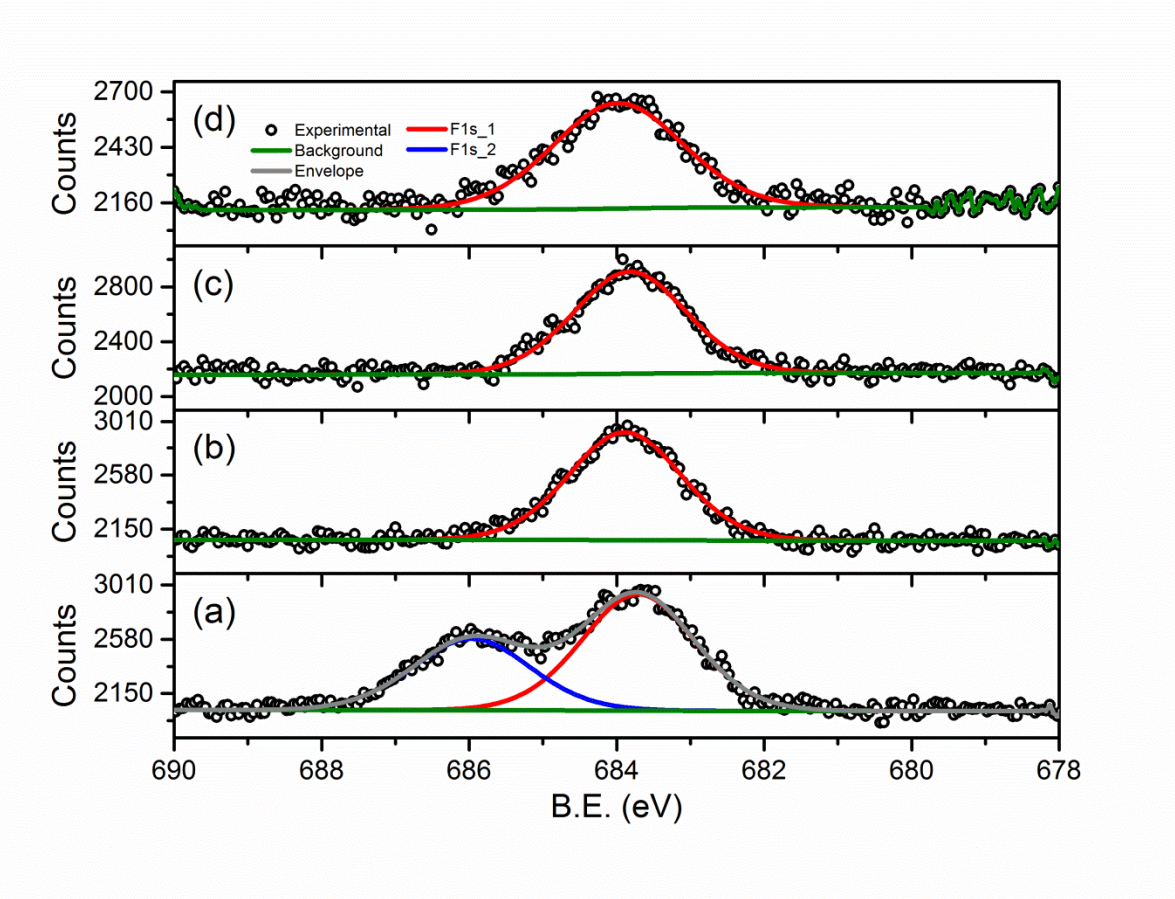

Fig. 3-9 XPS spectra of fluorine: (a) 3nm-NS, (b) 3nm-NS after heating at 350 ^{o}C for 4 h, (c) 3nm-NS washed with H_2O_2/NH_3 solution. (d) 3nm-NS washed with H_2O_2/NH_3 solution after heating at 350 ^{o}C for 4 h.

The quantification of atomic ratio of fluorine to titanium was obtained by comparing the background subtracted peak area of fluorine and titanium from the full scan, and the result are listed in Table 3-2.

Table 3-2 Surface Fluorine To Titanium Ratio of Anatase Nanosheets From XPS

	3nm-NS	350 ^{o}C calcined sample	H_2O_2/NH_3 treated sample	H_2O_2/NH_3 treated sample after calcination
F1/Ti	0.19	0.19	0.13	0.12
F2/Ti	0.12	--	--	--

Two fluorine peaks were observed. The binding energy of F1 1s electron is centred at 683.71 eV and that of F2 is centred at 685.97 eV. The F2 peak disappears after either heating or the treatment of H_2O_2/NH_3. This peak should be attributed to the surface adsorbed fluorocarbon pieces[3], formed during the solvothermal reaction. The F1 peak at 683.71 eV is assigned to the surface bonded, chemisorbed F^- (Ti-F) based on its binding energy[4]. A similar peak assignment was reported in previous paper[5]. The surface bonding of F-Ti is very strong. The ratio of surface bonded fluoride to titanium did not vary after heating, but was reduced by 36% after the treatment of H_2O_2/NH_3.

In summary, the H_2O_2/NH_3 treatment can effectively remove the surface organics and part of the surface bonded fluoride.

3.2.3 Electrochemical property of 3nm TiO_2 nanosheets

In the following section the electrochemical performance of the 3nm-NS calcined at different temperatures and the sample after the treatment of H_2O_2/NH_3 will be studied.

The general charge/discharge process can be described by the following equation,

$TiO_2 + xLi^+ + xe^- = Li_xTiO_2$ $(0 \leq x \leq 1)$ (discharge process: form left to right)

Previous work has shown that a plateau around 1.75 V on discharge and 1.85V on charge should be observed due to a two phase equilibrium reaction between a Li-poor phase ($Li_{0.01}TiO_2$) and Li-rich phase ($Li_{0.6}TiO_2$)[6]. Generally, the micron-sized anatase can accommodate up to *ca.* 0.5 Li per unit of TiO_2 on the initial discharge to 1 V, corresponding to a capacity of 167 mAh/g[7], and this capacity fades rapidly due to the sluggish nature of Li insertion and de-insertion. A discharge capacity of *ca.* 150 mA/g for the materials synthesized by similar methods was reported[8], and the capacity decreases during the following cycles. Higher capacities were achieved in some other nanoforms of anatase, e.g., mesoporous TiO_2[9], hierarchical structure[10], and nanotube struture[11].

The cycling performance of the 3nm-NS after annealing at different temperature and H_2O_2/NH_3 treatment is presented in Fig. 3-10. The initial capacity, capacity loss on the first cycle, and capacity retention after 100 and 200 cycles are summarized in Table 3-3. In order to understand the fading of the capacity during cycling and the origin of the irreversible

capacity, the load curves of the 1st, 2nd, 5th, 10th, and 100th cycles for each of the samples are plotted in Fig. 3-11

Table 3-3 Initial discharge capacity and capacity retention of 3nm-NS sample

	Initial discharge capacity (mAh/g)	Initial charge capacity (mAh/g)	Irreversible capacity on first cycle (mAh/g)	Capacity after 100 cycles (mAh/g)	Capacity after 200 cycles (mAh/g)	BET Surface area (m^2/g)
3nm-NS	322	180	142	18	11	170
300 °C 4h	240	205	35	38	32	93
350 °C 4h	233	212	21	134	113	74
400 °C 4h	184	167	17	105	95	65
H_2O_2/NH_3 350 °C 4h	301	257	44	201	185	163

Performance *vs.* annealing temperature. The capacity of the pristine 3nm-NS and 300 °C annealed sample faded rapidly after cycling (See Fig. 3-10), with only 18 mAh/g and 38 mAh/g remaining after 100 cycles.

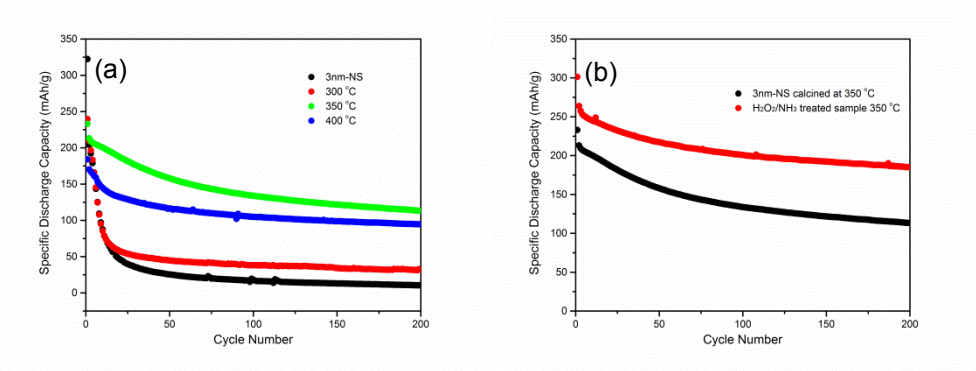

Fig. 3-10 Variation of specific discharge capacity with cycle number for anatase nanosheets composite electrode. (a) the effect of heat treatment; (b) the effect of surface treatment. The cells were cycled between 3-1 V at a current density of 170 mA/g.

The gradual loss of their charge/discharge plateaux during cycling is clearly shown on the load curves (Fig. 3-11 (a) (b)). This implies the diminishment of two-phase insertion and de-insertion reaction of Li. This is possibly due to the poor crystallinity of the 3nm-NS and 300 °C annealed sample. After annealing at higher temperature, *e.g.*, 350 °C and 400 °C, the

cycleability of the nanosheets was improved dramatically. The capacity remains at a reasonable value of 134 mAh/g, and 104 mAh/g after 100 cycles. The plateaux still exist after 100 cycles (Fig. 3-11 (c) (d)). Annealing at higher temperature generally gives rise to better crystallization, and a larger particle size. Higher degree of crystallization will contribute to more stable cycleability, which also explains the lower capacity fading of 400 ^{o}C annealled sample than that of 350 ^{o}C sample (See Fig. 3-10).

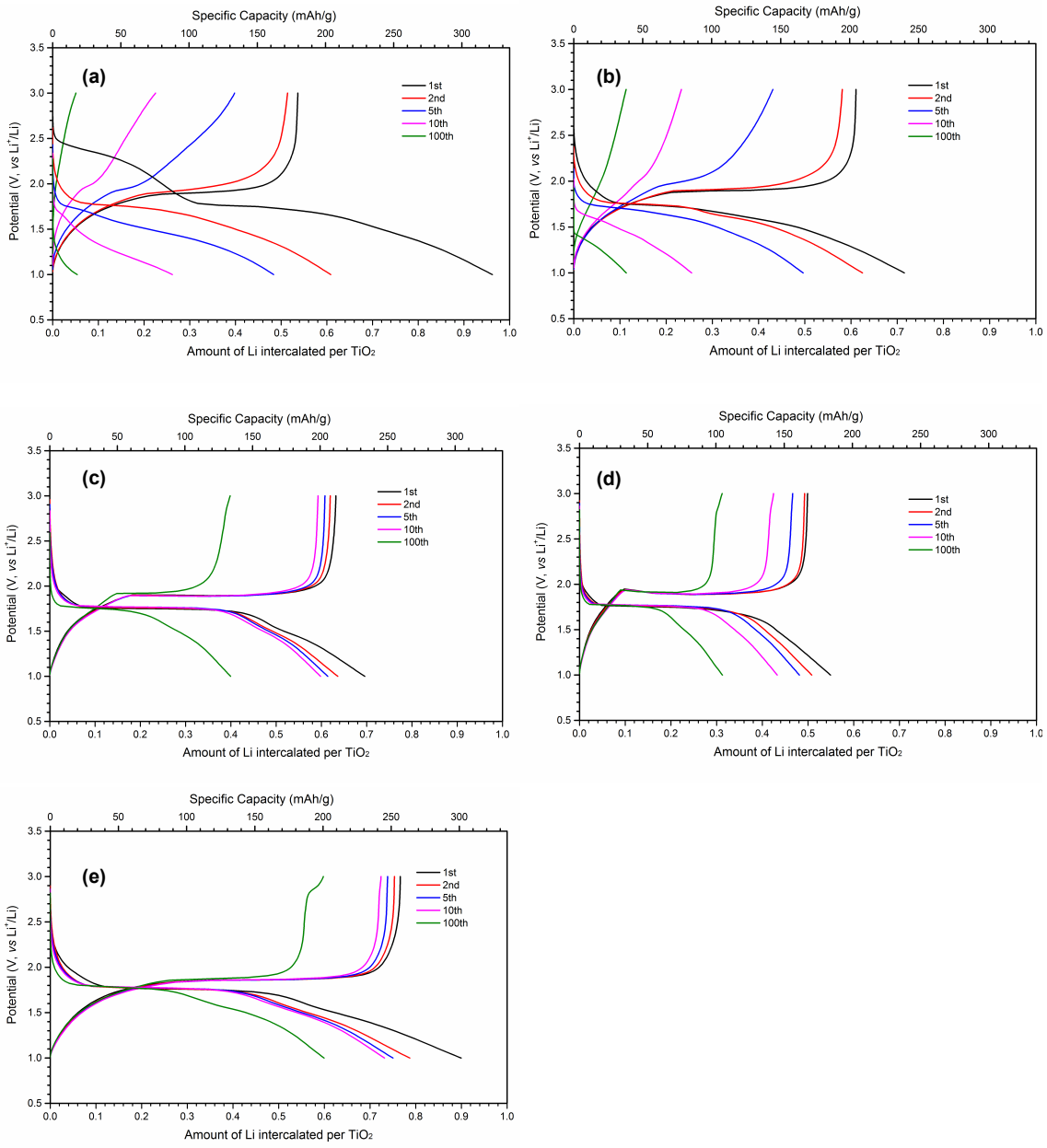

Fig. 3-11 The load curves of various anatase nanosheets samples. (a) 3nm-NS; (b) 300 ^{o}C sample; (c) 350 ^{o}C sample; (d) 400 ^{o}C sample; (e) surface treated sample with H_2O_2/NH_3 after calcined at 350 ^{o}C

However, the capacity of the 350 ^{o}C sample is higher. This can be ascribed to the size effect of anatase nanoparticles. Since the first cycle generally involves an irreversible surface reaction between electrolyte and the surface of the nano active material, the second discharge/charge curve is more suitable for the study of the intercalation behaviour. The second discharge capacity of different nanosheets and their capacity from different electrochemical behaviours are listed together with the texture properties of the nanosheets in Table 3-4.

Table 3-4 Capacity of the second discharge and physical properties of different nanosheets

	Second Discharge Capacity (mAh/g)	Plateau Region (mAh/g)		Capacity From Plateau Region (mAh/g)	Capacity From Slope Region (mAh/g)	Nano-sheets Thickness (nm)	BET Surface area (m^2/g)
		Start	End				
3nm-NS	204.4	26.8	67.0	40.2	164.2	2.81	170
300 ^{o}C 4h	207.7	26.8	83.8	57.0	150.8	3.62	93
350 ^{o}C 4h	211.1	26.8	130.7	103.9	107.2	4.21	74
400 ^{o}C 4h	170.9	10.1	110.6	100.5	70.4	>7	65
H_2O_2/NH_3 350 ^{o}C 4h	251.3	33.5	144.1	110.6	140.7	4.68	163

The shape of the discharge profiles varies from different samples. Typically we expect a two-phase intercalation behaviour for anatase, characterized by the existence of a long plateau on the discharge curve, due to the equilibrium between the co-existing Li-poor and Li-rich phase. However, the load curves of these nano anatase particles deviate from that. There are currently two explanations that describe the slope in the load curves of anatase nanoparticles and the associated increased capacity: 1) pseudocapacitive/surface storage[12]; 2) solid solution process[13, 14]. In the surface storage hypothesis, besides the common intercalation, Li^+ can be stored at the nanoparticle surface and grain boundaries electrochemically, resulting in a slope on the load curve which follows a capacitive behaviour, and a reduced particle size generally leads to larger surface area, and hence the enhanced capacity in proportion to the surface area. In the solid solution hypothesis, the solid solution process becomes more energetically favourable with a reduced particle size than the established two-phase reaction. The concentration dependence of Li^+ free energy in the Li-TiO_2 solid solution, which

modifies the equilibrium potential of Li^+/Li, also leads to the slope feature on the load curve, and this solid solution phase can accommodate more lithium. Both effects may contribute to the capacity variation of the nanosheets calcined at different temperature. However, the solid solution rationale is the best explanation in this situation for the following reason. The capacity of the slope regions increases more significantly from the 400 ^oC sample to the 300 ^oC sample than the changes of their BET surface area. For example, while the surface area increases by 14% from 400 ^oC to 350 ^oC, the slope capacity boosts by 52%, not proportional to the increment of surface area. Combined with the fact that plateau region diminishes with the particle size reduction, it is more likely that the sloped regions seen for the 300 ^oC to 400 ^oC annealed samples are mainly due to the formation of the more Li-rich Li-TiO_2 solid solution.

To summarise it is clear that the 350 ^oC calcination process results in the material with the best compromise of capacity and cycleability.

Performance *vs.* surface treatment. The speculation that cleaner and larger surface will lead to a higher capacity of the anatase nanosheets is confirmed in this section. The surface treatment by H_2O_2/NH_3 has improved the electrochemical performance of the 3nm-NS significantly (See Fig. 3-10). This sample (denoted as "treated sample") demonstrated an initial discharge capacity of 301 mAh/g ($Li_{0.9}TiO_2$) with 44 mAh/g irreversible capacity loss on the first cycle, and 251 mAh/g ($Li_{0.75}TiO_2$) on the second cycle. And the capacity remained at 201 mAh/g after 100 cycles, and 184 mAh/g after 200 cyles, much higher than the 350 ^oC sample. For the same reason discussed above, the second discharge/charge curves of this sample (denoted as "treated sample") is compared with the 350 ^oC sample in order to illustrate the origin of the increased capacity. The capacity from the plateau region is 110.6 mAh/g (Li per TiO_2) for the treated sample and 103.9 mAh.g for the 350 ^oC sample, respectively. The major discrepancy in their capacity originates from the slope regions, 140.7 mAh/g for the treated sample and 107.2 mAh/g for the 350 ^oC sample (See Table 4 and Fig. 3-11 (d) (e)). The similarity in their particle sizes (4.21 nm for the 350 ^oC sample and 4.68 nm for the treated sample) should result in a similar capacity through the solid solution mechanism. It is therefore proposed that the extra 0.1 Li storage (34 mAh/g) of the treated

sample from the sloped region should be ascribed to the surface storage. Surface storage contributes very little to the capacity increase of the untreated samples, as analysed before, however, the treatment with H_2O_2/NH_3 increased the surface area and also modified the surface condition. The surface area of the treated sample remained at 163 m^2/g after annealing at 350 ^oC, while that of untreated sample decreased to 74 m^2/g. It is believed that the clean surface of the treated sample with less organics and fluoride residues together with higher surface area has promoted lithium storage via the pseudocapacitive behaviour, thus an increased capacity.

Finally, the rate performance of the treated sample is presented in Fig. 3-12. At a high rate of 1700 mA/g (~10C), this sample rendered an initial capacity of 186 mAh/g, and the capacity still remained at 120 mAh/g after 100 cycles, demonstrating its capability as a good anode material for Li-ion batteries.

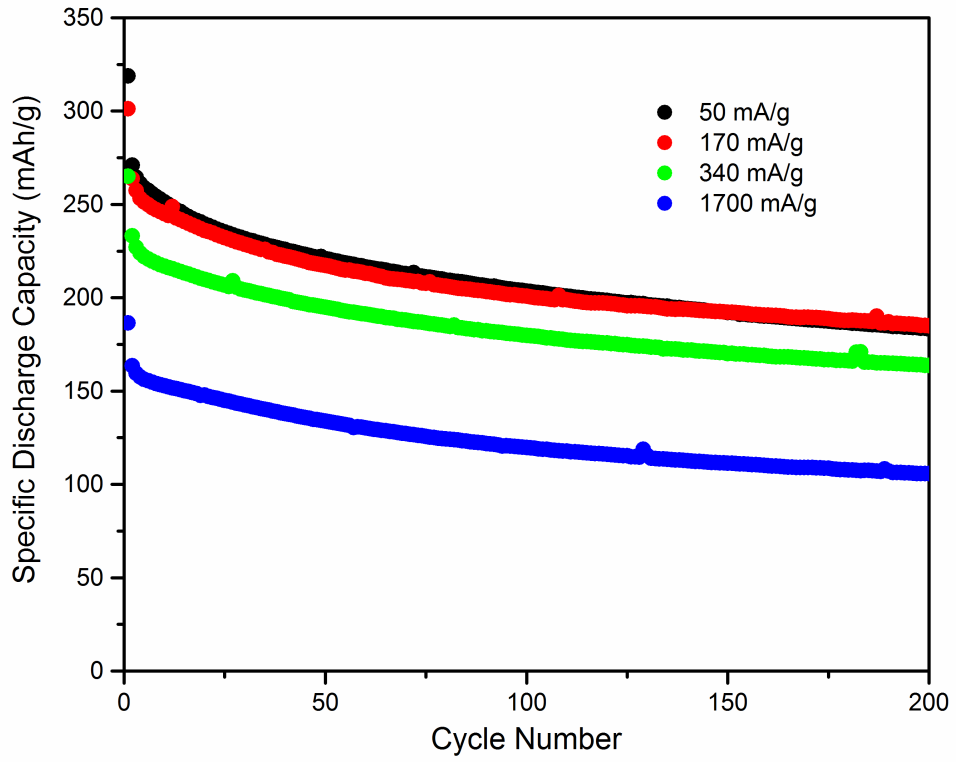

Fig. 3-12 Rate performance of the H_2O_2/NH_3 treated sample after annealing at 350 ^oC for 4 h

3.3 Conclusion

Ultrathin TiO_2 nanosheets with a regular shape were successfully synthesized through solvothermal reactions. A series of treatments were applied to alter the material shape, size, and morphology. The effect of these changes on the electrochemical behaviour was examined. It was found that crystallinity, particle size, and surface conditions are all important factors that determine the electrochemical property of the ultrathin TiO_2 nanosheets. Smaller particle sizes gives rise to more Li insertion through a solid solution process, and a larger and clean surface will also contribute more capacity via a pseudocapacitive surface storage. A reversible capacity over 200 mAh/g at a rate of 170 mAh/g has been achieved by controlling the particle size and applying a proper surface treatment.

Reference

1. Yang, X.H., et al., *Ultra-thin anatase TiO2 nanosheets dominated with {001} facets: thickness-controlled synthesis, growth mechanism and water-splitting properties.* CrystEngComm, 2011. **13**(5): p. 1378-1383.
2. Yang, H.G., et al., *Anatase TiO2 single crystals with a large percentage of reactive facets.* Nature, 2008. **453**(7195): p. 638-641.
3. Moulder, J.F., J. Chastain, and R.C. King, *Handbook of X-ray photoelectron spectroscopy: a reference book of standard spectra for identification and interpretation of XPS data*. 1992: Perkin-Elmer Eden Prairie, MN.
4. Dozzi, M.V., B. Ohtani, and E. Selli, *Absorption and action spectra analysis of ammonium fluoride-doped titania photocatalysts.* Physical Chemistry Chemical Physics, 2011. **13**(40): p. 18217-18227.
5. Ruzicka, J.-Y., et al., *XPS and NEXAFS study of fluorine modified TiO2 nano-ovoids reveals dependence of Ti3+ surface population on the modifying agent.* RSC Advances, 2014. **4**(40): p. 20649-20658.
6. Wagemaker, M., A.P.M. Kentgens, and F.M. Mulder, *Equilibrium lithium transport between nanocrystalline phases in intercalated TiO2 anatase.* Nature, 2002. **418**(6896): p. 397-399.
7. Wagemaker, M., et al., *Multiple Li Positions inside Oxygen Octahedra in Lithiated TiO2 Anatase.* Journal of the American Chemical Society, 2003. **125**(3): p. 840-848.
8. Sun, C.H., et al., *Higher charge/discharge rates of lithium-ions across engineered TiO2 surfaces leads to enhanced battery performance.* Chemical Communications, 2010. **46**(33): p. 6129-6131.
9. Wang, Z., et al., *Preparation and Li-intercalation properties of mesoporous anatase-TiO2 spheres.* Electrochemical and solid-state letters, 2007. **10**(3): p. A77-A80.
10. Chen, J.S., et al., *Constructing Hierarchical Spheres from Large Ultrathin Anatase TiO2 Nanosheets with Nearly 100% Exposed (001) Facets for Fast Reversible Lithium Storage.* Journal of the American Chemical Society, 2010. **132**(17): p. 6124-6130.
11. Xu, J., et al., *Electrochemical properties of anatase TiO2 nanotubes as an anode material for lithium-ion batteries.* Electrochimica Acta, 2007. **52**(28): p. 8044-8047.
12. Wang, J., et al., *Pseudocapacitive Contributions to Electrochemical Energy Storage in TiO2 (Anatase) Nanoparticles.* The Journal of Physical Chemistry C, 2007. **111**(40): p. 14925-14931.
13. Wagemaker, M., W.J. Borghols, and F.M. Mulder, *Large impact of particle size on insertion reactions. A case for anatase Li x TiO2.* Journal of the American Chemical Society, 2007. **129**(14): p. 4323-4327.
14. Sudant, G., et al., *Electrochemical lithium reactivity with nanotextured anatase-type TiO2.* Journal of Materials Chemistry, 2005. **15**(12): p. 1263-1269.

Chapter 4 Synthesis of TiO_2(B) Nanoparticulates And Its Application As Anode Material For Li-ion Battery

In this chapter, TiO_2(B) nanoparticles of extremely small size, synthesized by a hydrothermal reaction, are described. The size of the particles was controlled by the reaction time. Particles smaller than 3 nm were obtained without any surfactant residue. Their properties were characterized by a variety of methods. The purity of the nanoparticles was confirmed by PXRD, cyclic voltammetry, Raman spectroscopy, and solid-state MAS NMR. The size and the shape of the particles were determined using TEM images and PXRD data, by employing refinements by Rietveld and Debye methods. The presence of surface hydroxyl groups was established by FTIR and ^{1}H-NMR spectroscopies. It has been shown that the 3nm TiO_2(B) is a promising candidate material for anodes in Li-ion batteries, exhibiting superior performance compared with bulk, nanotube and nanowire morphologies of TiO_2(B).

4.1 Introduction

In addition to anatase (space group $I4_1/amd$), rutile (P42/mnm), and brookite (Pcab), TiO_2(B) (C2/m) is another polymorph of TiO_2, which exists under ambient conditions. Discovered in 1980s by Marchand R. and co-workers[1], it has attracted great attention as a promising anode material for rechargeable lithium ion batteries, due to high rate of Li intercalation/de-intercalation, excellent cycleability, improved safety and low cost. The most widely used commercial anode material, graphite, has a high capacity and low potential against Li[2]. However, safety concerns limit its use, especially in high-rate devices, because the lithiation potential of graphite is close to that of lithium plating. The latter may cause battery failures due to short-circuiting and even leads to explosion[3]. This problem is more acute in high-power lithium batteries for grid storage or electric vehicles. TiO_2(B) is an excellent alternative, since its characteristic potential is around 1.5V (*vs.* Li^+/Li)[4], much higher than that of lithium plating. The less beneficial higher anode potential of TiO_2(B) (1.5 V-1.7 V) can be compensated by using a high voltage cathode, such as Li-Ni-Mn-O spinel[5].

The theoretical capacity of TiO_2(B) is 335 mAh/g, which corresponds to 1 Li per TiO_2 ($LiTiO_2$(B))[6]. The process of insertion and extraction of Li^+ can be described as the following equation:

$$x\ Li^+ + TiO_2(B) + x\ e^- = Li_xTiO_2(B) \quad (x=0\sim1) \qquad \text{Eq(1)}$$

In practice, bulk TiO_2(B) has initial discharge capacity of 230~270 mAh/g, followed by a reversible capacity of 100~200 mAh/g in the subsequent cycles at a slow C-rate[4, 7, 8]. A number of its nano varieties have been proven to have higher capacity even at high rates. Previous work by Armstrong et al has shown that TiO_2(B) nanowires can accommodate 0.91 Li ($Li_{0.91}TiO_2$(B)), providing a capacity of 305mAh/g at a rate of 50 mA/g (0.15C) on initial discharge[4], while the capacity of nanotubes increases to 330 mAh/g[9]. During the subsequent cycles their capacity drops down to 200 mAh/g and 230 mAh/g, respectively, and remains stable. In another study, TiO_2(B) nanosheets are shown to maintain 220 mAh/g reversible capacity at 10C, stable even after 200 cycles[10].

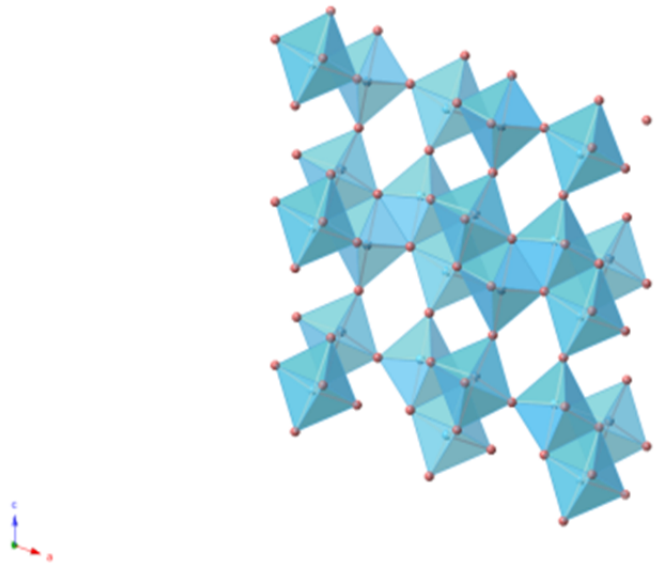

Fig. 4-1 [010] view of TiO_2(B) crystal structure

Comparing with other TiO_2 polymorphs, TiO_2(B) has the largest lattice parameters and a sizeable 1-dimensional channel along the b axis (as shown in Fig. 4-1). These structural features promote fast lithium transport in TiO_2(B), and therefore enhanced rate performance. Theoretical study by Arrouvel et al reveals a low energy barrier for lithium transport along the b axis[11]. Van der Van at el. established the lithiation profile using DFT calculations[6]. They found that TiO_2(B) can actually accommodate 1.25 Li per TiO_2. However, insertion of the additional 0.25 Li^+ occurs at very low voltage and is due to the lattice distortion and subjected to a strong Li-Ti repulsion. Although the most favourable lithium site is still being debated, the theoretical capacity is predicted to be in the range from 240 to 335 mAh/g when cycling between 1 V and 2.5 V *vs.* Li.

Such features of nanostructured TiO_2(B) make them a promising anode material for practical applications. In this chapter, the properties of a novel TiO_2(B) naomaterial, 3 nm particles, are reported.

4.2 Experimental

4.2.1 Synthesis of TiO_2(B) nanoparticles.

TiO_2(B) nanoparticles were synthesized by a modified hydrothermal reaction originally reported by M. Kobayashi[12]. 0.72 g of Ti powder (99.7%, ~325 mesh, Alfa Aesar) was dissolved in a basic piranha solution, made up with H_2O_2 (60 mL, 30.0%, Fisher Scientific) and NH_3 (20 mL, 35%, Fisher Scientific), in an ice-water bath for 2-3 h with stirring. Then 1.71 g of glycolic acid (99%, Fisher Scientific) was added into the solution. To eliminate the excessive H_2O_2 and NH_3, the solution was kept at 80 °C for 3-4 hours, until forming a yellow gel ($(NH_4)_6[Ti_4(C_2H_2O_3)_4(C_2H_3O_3)_2(O_2)_2]$). The gel was re-dissolved in ca. 40 ml of distilled water and 3.0 g of H_2SO_4 (98.0%) was added. Then the total volume was then adjusted to 60 mL by adding water (here the H_2SO_4 was ca. 0.50 mol/L). 20 mL of the resulting solution was placed into a 50 ml Teflon-lined stainless steel autoclave and heated at 160 °C for a certain period of time, e.g. 30 min, 1 h, 4 h, 9 h, 13 h, 17 h, and 24 h. After cooling down to room temperature, the solid products were separated from the solutions by centrifugation and washed several times by water and ethanol to remove the residual acid. The solid was dried at 60 °C overnight. Finally, the samples were ground and calcined at 300 ^oC in dry air. The sample for ^{17}O NMR was made by the same procedure up to the point when the yellow gel was formed. The gel was diluted to 60 ml, then 1 ml of the solution was transferred into a small vial dried at 80 ^oC, and 1 ml of 45% ^{17}O-enriched water was added into the vial and 0.05 g of H_2SO_4 was added to adjust the pH. The vial was placed into a 10 ml Teflon-lined stainless steel autoclave and heated at 160 ^oC for 30 min. The following treatment was the same as described above.

4.2.2 Surface treatment.

The 30 min sample after calcination was subjected to a surface treatment. 1 M lithium ethoxide (EtOLi) in THF and 1 M n-butyllithium (BuLi) in hexane (Acros) were used as the surface treating agents. For EtOLi treatment, 0.4 g of the nanoparticles (5 mmol) were dispersed in 100 mL of dry THF (H_2O < 4 ppm) under vigorous stirring for 1 h inside an Ar-

filled glovebox (O_2 and H_2O content less than 0.1 ppm) , and then 2 mL of EtOLi were added into the dispersion dropwise (the amount of EtOLi is excessive compared to the capacity loss on the initial discharge--75 mAh/g, corresponding to 0.2 Li per TiO_2) and the mixtures were left under stirring for another 1 h to complete the reaction. The solid was separated by filtration and washed with dry THF 3 times, and dried under vacuum (less than $1x10^{-3}$ mbar) for 1 h. In the BuLi treatment, the procedure was similar, and the same volume of dry hexane (H_2O < 1 ppm) was used instead of THF, and 1.5 mL of BuLi solution was used instead of EtOLi (The amount of BuLi was calculated according to 0.3 Li per TiO_2(B)). Note that the samples after the treatment were air-sensitive and should be kept inside the glovebox, and electrode casting was also performed inside glovebox.

4.3 Result and discussion

4.3.1 Size and purity of the TiO_2(B) nanoparticles

The size of the TiO_2(B) nanoparticles is controlled by the time of the hydrothermal reaction. To get the desired size of single crystalline TiO_2(B) particles a range of the reaction times, 30 min, 1 h, 4 h, 9 h, 13 h, 17 h, and 24 h were investigated. The size was calculated using the Scherrer equation (See Chapter 2) from the half width of a 110 powder diffraction peak at 24.9^o and verified by TEM. Powder diffraction and cyclic voltammetry confirmed the phase purity. The surface area of the particles was measured by N_2 sorption under 77K.

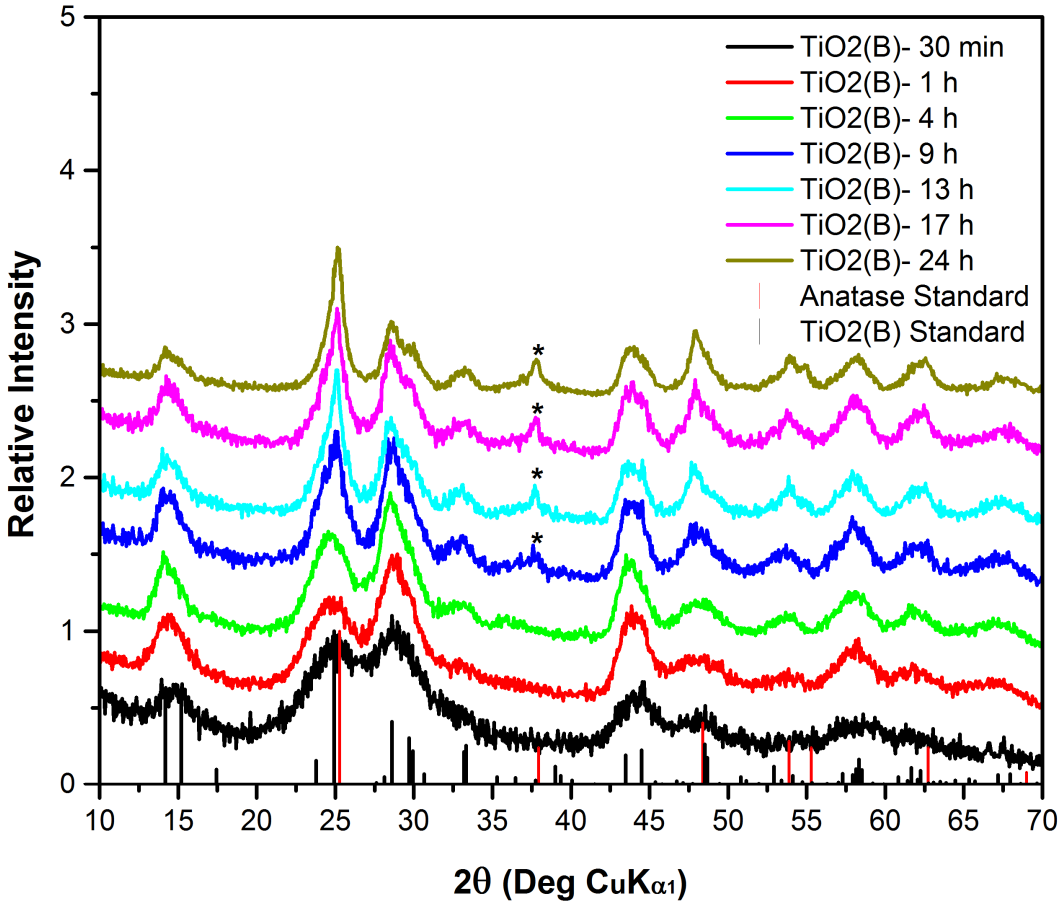

Fig. 4-2 PXRD patterns of different nanocrystalline TiO_2(B) particle hydrothermal treated at 160 °C for different time , 1/2 , 1, 4, 9, 13, 17, and 24 h. The asterisks indicate anatase impurity.

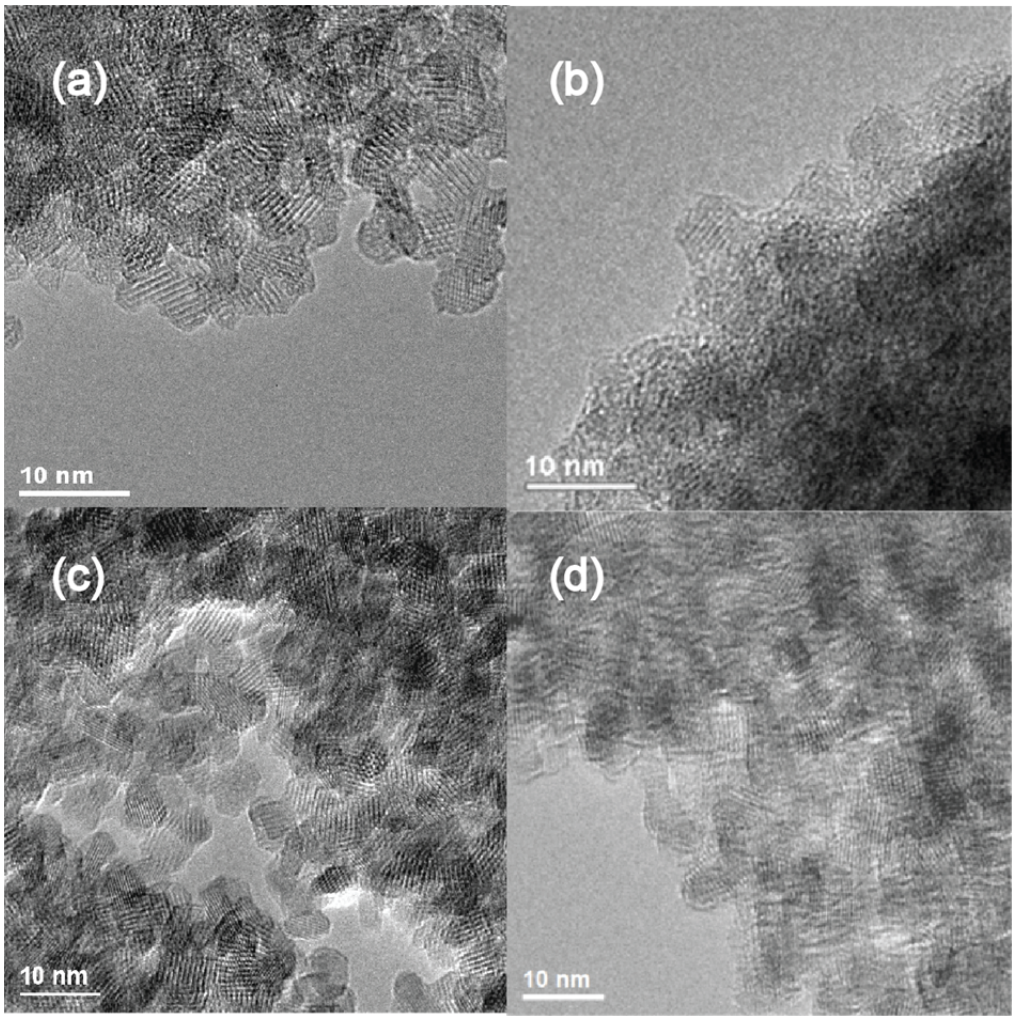

Fig. 4-3 TEM image of TiO_2(B) nanoparticles obtained from different hydrothermal time. (a) 30 min; (b) 1h; (c) 9h; (d)24 h

The 110 diffraction peak narrows as the hydrothermal time increases, indicating the growth of the crystallite size, Fig. 4-2. The size gradually changes from 3 nm to 6 nm with the increase of the reaction time from 30 min to 24 h. This is in good agreement with the TEM data (Fig. 4-3). The peak at 36.5^o, appearing in the diffraction patterns of the samples synthesised for ≥ 9 h, indicates anatase impurity. The peak broadening in the PXRD patterns results in significant overlap which makes it rather difficult to spot minor anatase impurities. This problem is most acute for the smallest particle size. Thus the phase purity of the TiO_2(B) nanoparticles was assessed by other techniques. Cyclic voltammetry (CV) can readily distinguish minor anatase impurity in TiO_2(B). Peaks in the voltammogram correspond to the lithiation/delithiation of different Li sites in the crystal. Anatase redox couple appears at higher potential than TiO_2(B), as intercalated Li^+ has higher energy in anatase than that in

TiO_2(B). Each powder was mixed with super P and Kynar 2801, in the ratio 7:2:1, placed into a coin cell and cycled at 10 mV/min against Li metal using LP30 as the electrolyte. The redox couple at 1.75 V and 1.9 V indicates the presence of the anatase impurity (Fig. 4-4). In agreement with the PXRD results, no anatase is found in samples synthesized in less than 4 h. Note that the peaks in the voltammogram broaden with the decrease of the particle size. This is possibly due to the pseudocapacitive behaviour[13] or the surface defects in the TiO_2(B) nanoparticles. The metastable nature of the TiO_2(B) phase prevents further growth of the particles by increasing the time of the hydrothermal synthesis beyond 4 h. Increased reaction time results in formation of a more thermodynamically stable phase -- anatase. In order to obtain pure TiO_2(B), the reaction time must be below 4 h. Physical properties of the TiO_2(B) nanoparticles are summarized in Table 4-1. The discrepancy between the particle sizes determined from the PXRD data and those using the N_2 adsorption data imply that the nanoparticles tend to form agglomerates, which is confirmed by TEM (Fig.3 (a)).

Table 4-1 Physicochemical properties of the nanoparticulate TiO_2(B)

Materials	**Phase (XRD/ CV)**	**S_{BET} (m^2/g)**	**Particle size (nm, by XRD)**	**Particle size (nm, by N_2 adsorption)**
TiO_2-30 min	TiO_2(B)	302	3.0	5.2
TiO_2-1 h	TiO_2(B)	280	3.5	5.6
TiO_2-4 h	TiO_2(B)	255	4.8	6.2
TiO_2-9 h	TiO_2(B)+anatase	244	4.9	6.5
TiO_2-13 h	TiO_2(B)+anatase	236	4.9	6.7
TiO_2-17 h	TiO_2(B)+anatase	187	5.1	8.5
TiO_2-24 h	TiO_2(B)+anatase	160	5.6	9.9
TiO_2-30min C*	TiO_2(B)	260	3.0	6.0

* TiO_2(B)- 30 min calcined at 300 ^oC for 1 h.

In the following sections, more detailed studies of the 3 nm TiO_2(B) nanoparticles after 1 h calcination at 300 ^oC are presented.

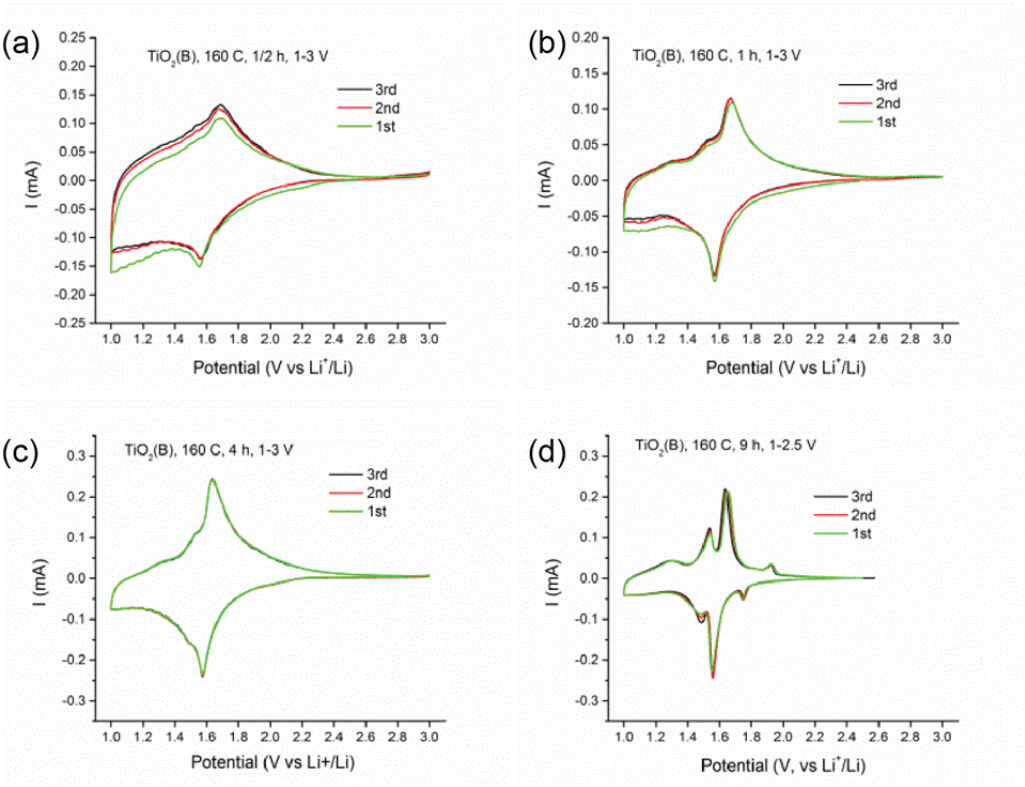

Fig. 4-4 Cyclic voltammetry for the TiO_2(B) nanoparticles derived from different hydrothermal time. (a) 30 min; (b) 1 h; (c) 4 h; (d) 9 h. The appearance of redox coulple at 1.75 V and 1.90 V indicates anatase phase impurity

4.3.2 Solid state NMR and Raman spectroscopy

Phase purity is particularly important for detailed studies. In order to verify that the 3 nm TiO_2(B) was not contaminated by anatase, the sample was characterised by ^{17}O solid state MAS NMR and Raman spectroscopy. These two techniques are sensitive to local structures and short range ordering rendering them as effective tools for discovering impurities in nanomaterials.

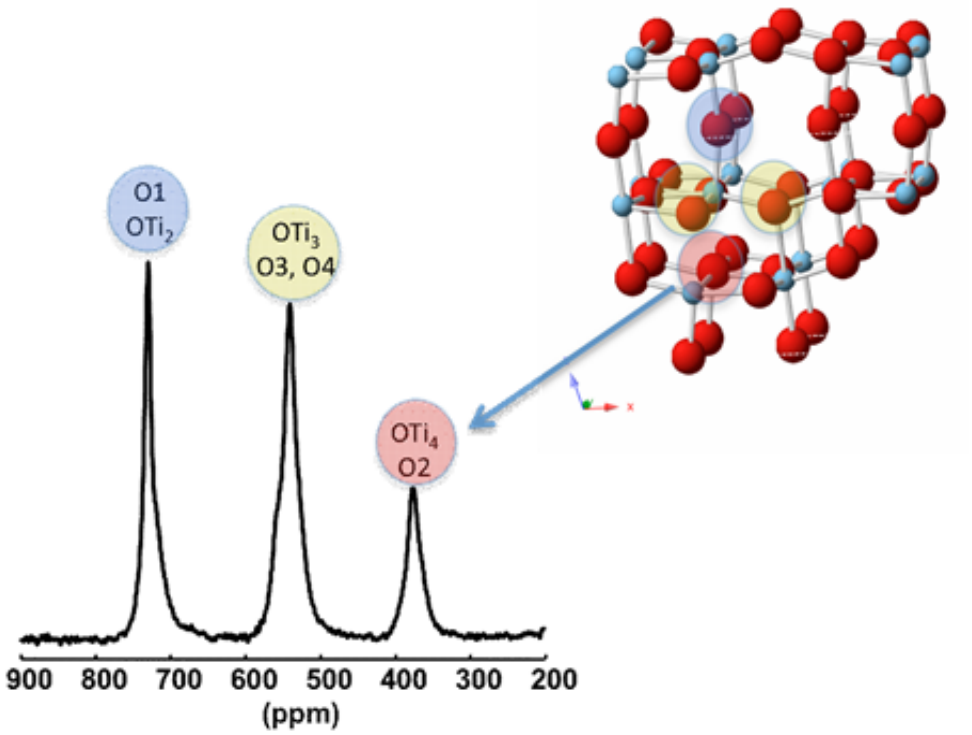

Fig. 4-5 O-17 Solid state MAS NMR pulse spectra collected at 16.5 T on a 600 MHz Bruker Advance III spectrometer at a spinning frequency of 60 kHz, with a π/2 pulse length of 0.5 μs and a recycle delay

Four crystallographically distinct O sites give rise to 3 peaks in ^{17}O solid state MAS NMR (Fig. 4-5), based on the values of chemical shifts, O1(highlighted in the blue circle) coordinates with 2 Ti atoms, while O2 (highlighted in red circle) coordinates with 3 Ti, and both O2 and O3 (highlighted in yellow circle) coordinate with 4 Ti. After integration, a 1:2:1 ratio of these peak area was obtained, which follows the ratio of the number of the corresponding O in perfect TiO_2(B) crystal.

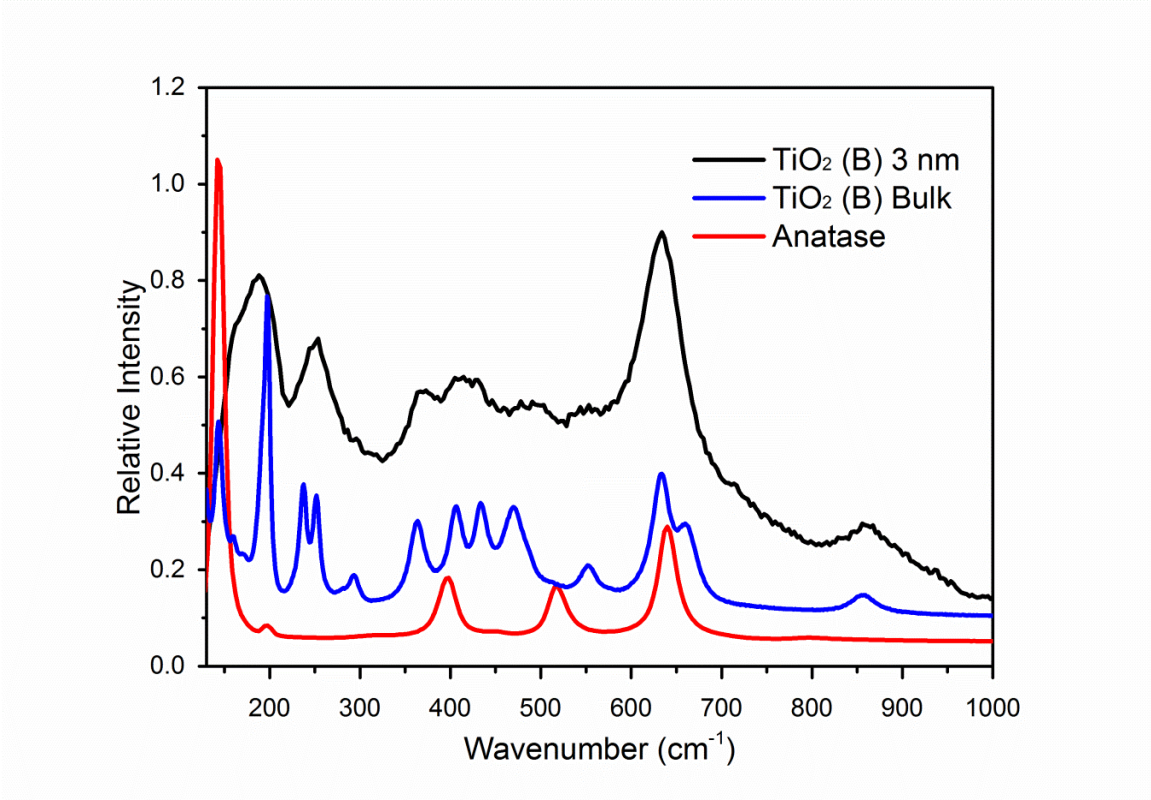

Fig. 4-6 Raman spectrum of 3 nm TiO_2(B) nanoparticles, TiO_2(B) bulk material, and anatase

In Fig. 4-6, the Raman spectrum of the 3 nm TiO_2(B) is compared with that of bulk TiO_2(B) and anatase. When the size of TiO_2(B) particles is on nanoscale, some Raman peaks of the phase merge or disappear while the majority of the rest become broad. In principle, all peaks that correspond to the vibrational or torsional excitation of the Ti-O bonds remain in the same position. Only peaks associated with long-range ordering shift due to size effect. There are no peaks that can be attributed to the anatase phase. According to the calculation of Ben Yihia and co-worker[14], all 5 anatase peaks in the region of wavenumbers from 130 cm^{-1} to 700 cm^{-1} are associated with the vibration modes of the Ti-O or O-Ti-O. Hence, if the anatase phase presents, the corresponding Raman peaks must appear in exactly the same position as in the bulk anatase. The purity of TiO_2(B) nanoparticles has been confirmed.

4.3.3 Surfactant-free surface and hydroxyl groups

One problem that often undermines the functionality of such small nanoparticles and inhibits their application is the remaining of the long chain surfactants on the surface. These surfactants are usually employed as the growth inhibitor during synthesis, and their presence can be detrimental to the properties of the nanoparticles. Complete removal of the surfactants usually involves strong oxidizing, acidic or basic conditions, and often leads to significant

increase in the particle size. Here the removal of surface glycolate has been achieved simply by calcination of the TiO_2(B) nanoparticles in dry air at 300 ^oC for 1 h and is not accompanied by particle growth (according to the diffraction data in Fig. 4-7).

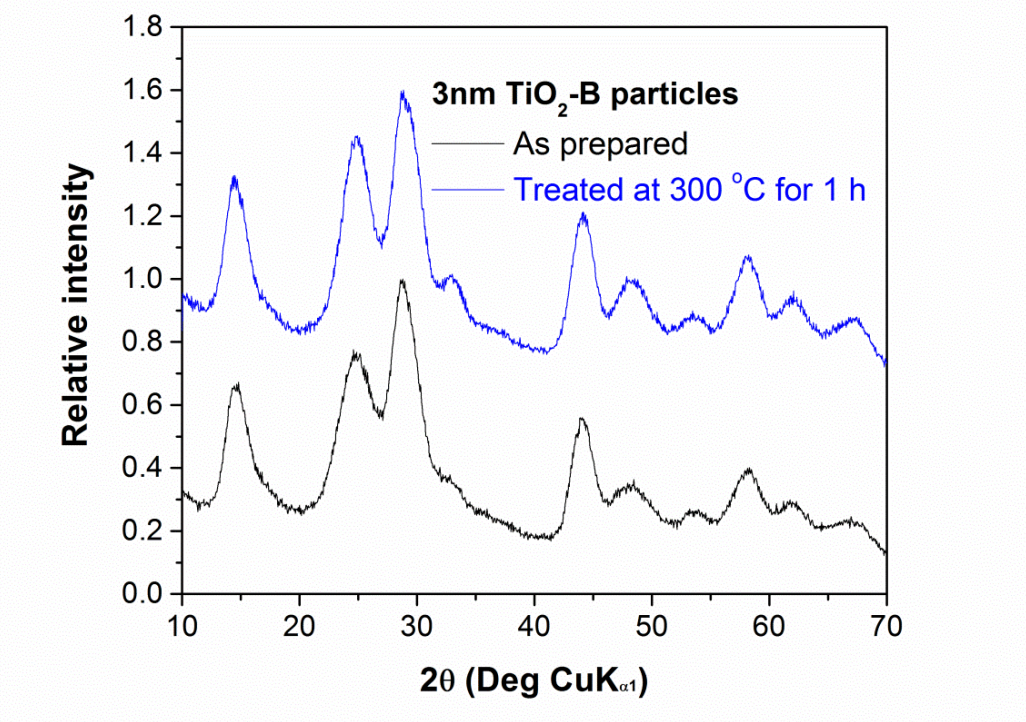

Fig. 4-7 PXRD pattern of the 3 nm TiO_2(B) before and after calcination at 300 ^oC for 1 h

Table 4-2 presents the result of CNH analysis. The amount of carbon drops considerably after the calcination. The 0.3% of the carbon residue translates into a less than 1 Å surface layer, if it is uniformly distributed on the particle surface.

Table 4-2 CHN analysis for 3 nm TiO_2(B)

Sample	C%	H%	N%
Fresh TiO_2(B) after hydrothermal	2.06	1.51	0.00
300 °C calcined in dry air for 1 h	0.33	0.72	0.44

Nanoparticles of small size and clean surface would have high surface energy and dangling bonds, making them unstable. The highly hygroscopic nature of titanium oxide leads to the assumption that the surface of the TiO_2(B) nanoparticles is likely to be stabilized by hydroxyl groups. To demonstrate this, FTIR and ^{1}H-NMR investigations were carried out.

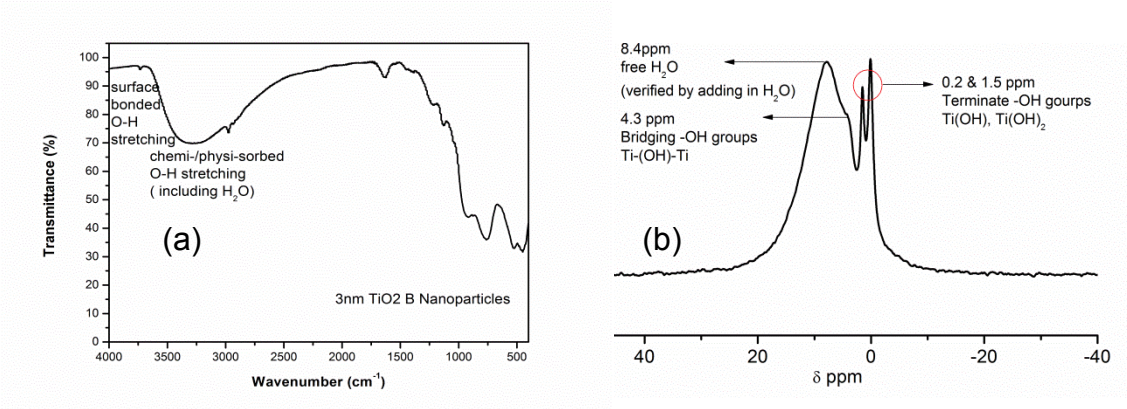

Fig. 4-8 (a) FTIR (b) ^{1}H-NMR Peaks are assigned to different -OH groups according to their chemical shifts

Fig. 4-8 presents the FTIR and ^{1}H-NMR spectra of the 3 nm TiO_2(B) calcined at 300 ^{o}C. The small sharp peak at 3750 cm^{-1} in the FTIR spectrum (Fig. 4-8(a)) is interpreted as a surface bonded -OH stretch, while the broad peak around 3300 cm^{-1} is due to the surface adsorbed undissociated H_2O or -OH involved in H-bonds according to previous literature[15]. More detailed information has been obtained from ^{1}H-NMR (Fig. 4-8(b)). Two types of hydroxyl groups have been identified: terminating -OH (Ti(OH)/Ti$(OH)_2$) and bridging -OH (Ti-(OH)-Ti). These hydroxyl groups, as will be shown later, contribute to the irreversible capacity loss of the battery. According to DFT calculation[16], the existence of these hydroxyl groups lowers the surface energy and promotes non-isotropic growth of the nanoparticles . Removal of the hydroxyl groups from the surface requires heating to a temperature at which the metastable TiO_2(B) phase transforms into more stable anatase.

4.3.4 Shape and size

The most direct method to obtain the shape and size information of nanoparticles is by TEM. However, the TEM itself is a highly selective technique that provides information from only a small part of the sample. Significantly better-averaged data can be obtained through the analysis of powder diffraction data.

The size and shape of nanoparticles determine the shape of peaks in PXRD patterns. Any violation of the translational symmetry is reflected in the broadening of powder diffraction peaks. Reduction in particle size is a prime example of such violation. One method to obtain particle shape information from PXRD data is the application of the Scherrer equation to individual reflections, corresponding to different crystallographic directions. However, unlike in the case of the anatase nanosheets (see previous chapter) whose diffraction peaks are well

resolved, there is significant peak overlap in the pattern of the 3 nm TiO_2(B), making the determination of the half width of each peak difficult. Determination of the half width was attempted by both Le Bail and Rietveld methods using GSAS program suite. Peak profile (using the pseudo-Voigt function), lattice parameters (C2/m), atomic coordinates (refined only in Rietveld) and background were refined to find the minimum of ^{2}- the weighted square difference between the calculated and experimental intensities. The values for full width at half maximum (FWHM) for individual peaks were calculated from the peak parameters and then translated into the sizes of each directions using Scherrer equation. Fig. 4-10 presents the result of the refinements and particles sizes in different directions are listed in the insets. Disagreement between the calculated results and TEM observation is obvious. According to the TEM data, Fig. 4-9, the particles have a preferential growth direction [001], while the calculated results indicate a near-spherical shape (both Le Bail and Rietveld). It is likely that the observed discrepancy stems from the unreliable background shape and anisotropy in the diffraction peak widths. A well-defined background is essential in these two methods. However, the background function parameters are variables in the refinement process, while the pronounced broadening of the peaks, coupled with the low symmetry of the structure, gives no indication as to where the background line is. In such situation the background is refined to allow isotropic peak broadening, which explains the spherical shape of the crystallite.

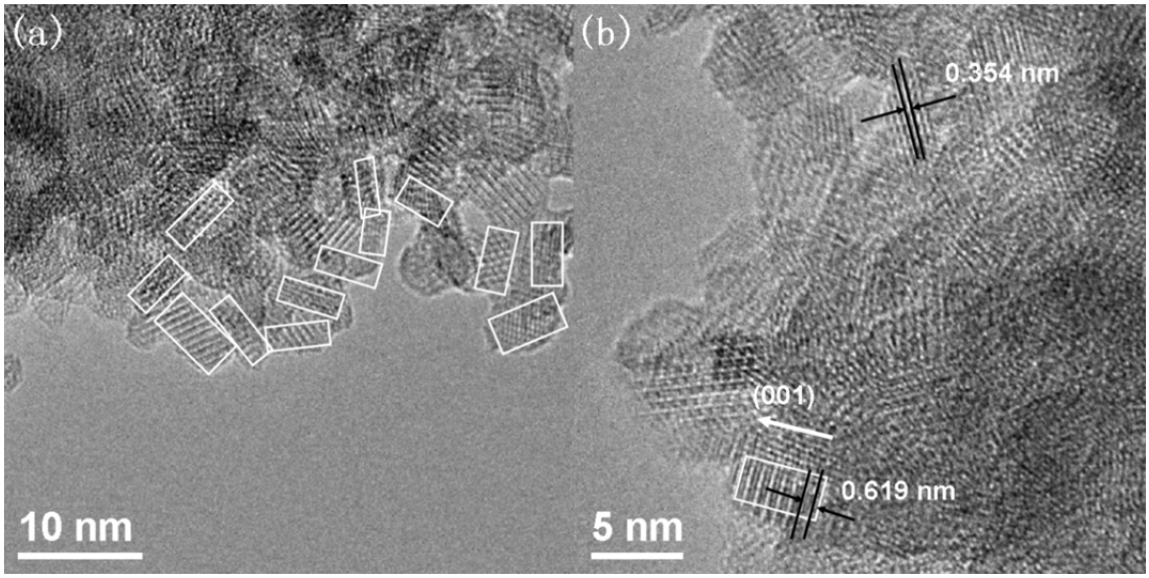

Fig. 4-9 The shape of the 3 nm nanoparticles observed using HR-TEM

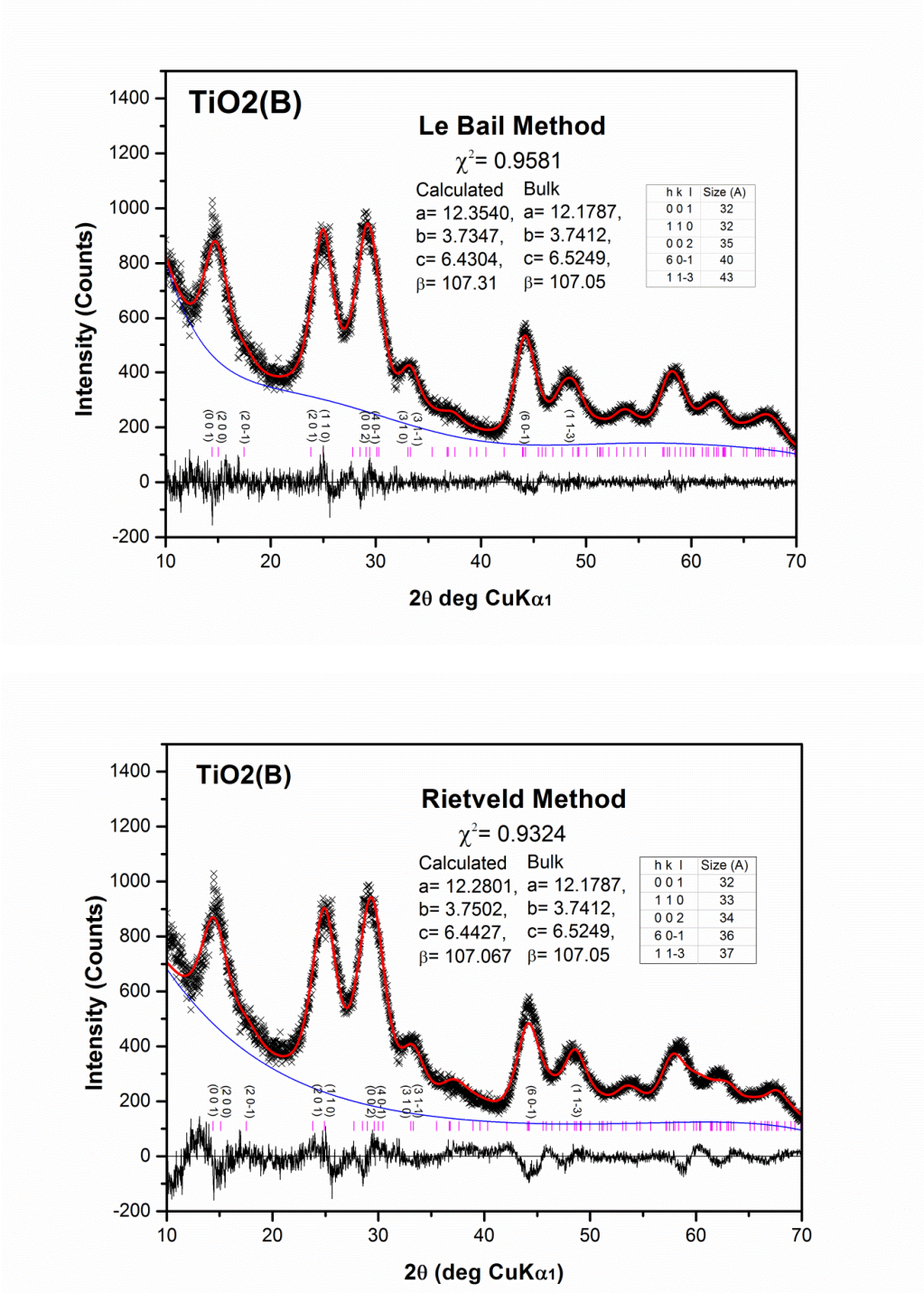

Fig. 4-10 GSAS refinement of the PXRD pattern of the 3 nm TiO_2(B) nanoparticles. The dimensions of nanoparticles calculated from the profile parameters are listed as tables. (a) Le Bail Method; (b) Rietveld Method

However, there are obvious signs of an anisotropic peak broadening in the diffraction data. E.g., the half width of the peak at ca. 29° is smaller than that at ca. 24.8°, while the previous one includes four reflections (002, 40-1, 111, and 400, the first three contribute evenly, and the intensity of the 400 reflection is low) and the later one originates mainly from the 110 reflection (200 reflection has low intensity). Given that, the diffraction should suggest a non-spherical shape of the TiO_2(B) nanoparticles. In order to obtain valid shape information, a new full-profile refinement based on the Debye equation was applied.

In this method, a powder diffraction pattern is calculated using Debye equation,

$$I(\theta) = \sum_n f_n^2(\theta) + 2\sum_i \sum_j f_i(\theta)\, f_j(\theta) \frac{\sin(4\pi r_{ij}\sin\theta/\lambda)}{4\pi r_{ij}\sin\theta/\lambda}$$

where $f_n(\theta)$ is the atomic factor of the corresponding atoms in the real crystal, λ is the wavelength of the X-ray (Cu $K\alpha_1$ =1.540562Å), and r_{ij} is the distance between the i^{th} and the j^{th} atoms in the particle. The summation is carried out over all atoms in a single nanocrystal. Diffraction patterns were calculated based on an ellipsoidal shape of TiO_2(B) nanoparticles. Lattice parameter (C2/m), coordinates, and the length of ellipsoidal axes were allowed to change. Strains and thermal displacement of Ti and O were also variable parameters. Starting from a 3 nm spherical shape, refinement was carried out by global minimization of the χ^2 through simulated annealing. Fig. 4-11 presents the result of the Debye refinement, which establishes that a 2.5x2.5x4.3 nm particle fits well the experimental pattern. This result is in good agreement with the TEM images. The non-spherical particle will still be referred to as 3 nm TiO_2(B) in later sections for convenience.

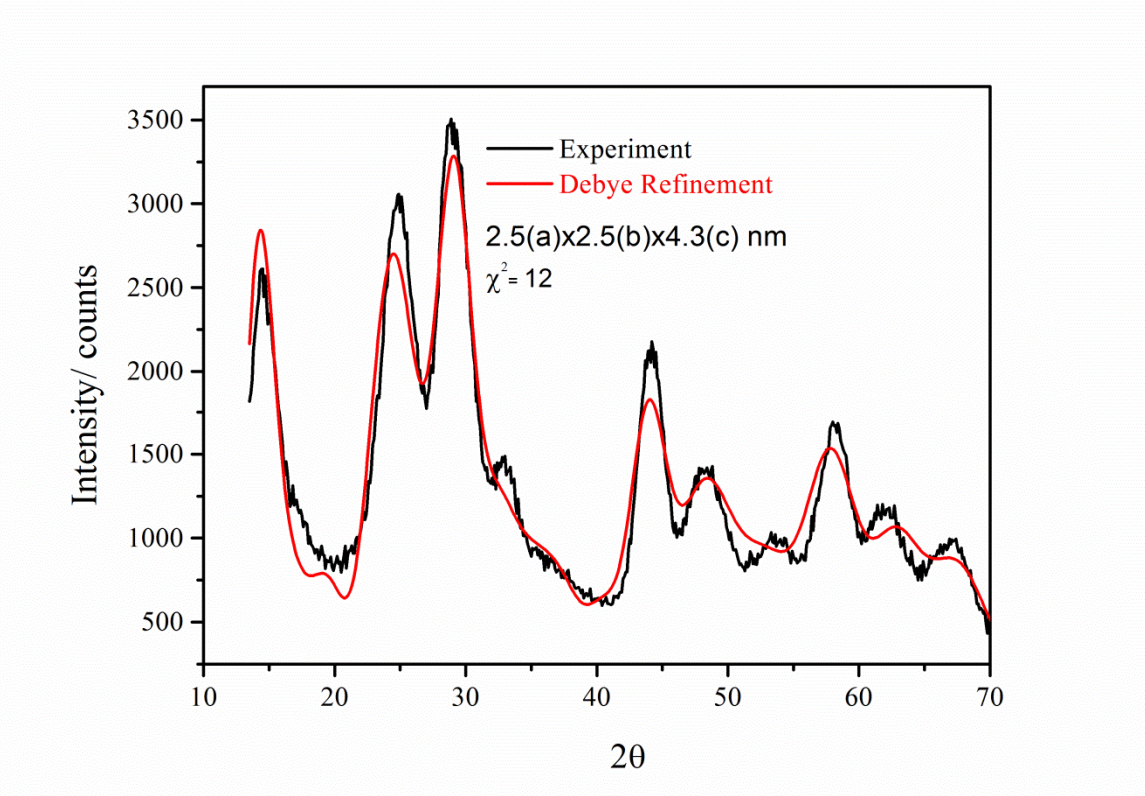

Fig. 4-11 Debye simulation of the PXRD pattern of the 3 nm TiO_2(B) nanoparticles

4.3.5 Electrochemistry of 3 nm TiO_2(B)

So far, the purity of the TiO_2(B) nanoparticles has been verified by a variety of methods and their size and shape have been established. The further study is focused on their electrochemistry. Electrochemical investigation was carried out in a coin cell, assembled according to the procedure introduced in Chapter 2. The ratio of TiO_2(B): Super P: Kynar was 8: 1: 1 and the cell was cycled between 2.5 -- 1 V at different rates.

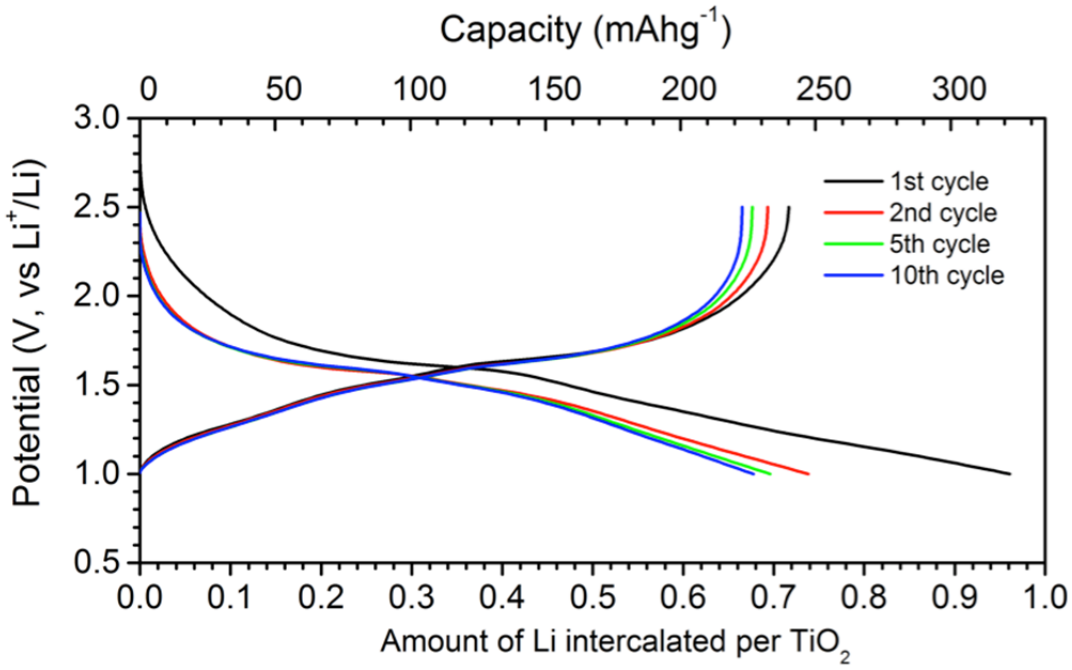

Fig. 4-12 Load curves of 3 nm TiO_2(B) with respect to the corresponding state of discharge/charge (Li amount per TiO_2) at a rate of 50 mA/g.The 1st, 2nd, 5th, and 10th cycles are plotted respectively

The load curves at slow rate (50 mAh/g) are presented in Fig. 4-12. The first discharge and charge capacity are 322 mAh/g and 247 mAh/g respectively, with a 75 mAh/g capacity loss. However, the irreversible capacity loss reduced to 15 mAh/g, 6% on the second discharge, and further reduced to only 2% after the fifth cycle. The reversible capacity becomes stable at 230 mAh/g after that. Most of the irreversible capacity loss on the first cycle is generally associated with the surface reaction between the nanoparticles and the electrolyte, due either to the electrolyte decomposition and the formation of the solid electrolyte interface (SEI) or to the lithiation of the surface -OH groups, which will be discussed in the next section.

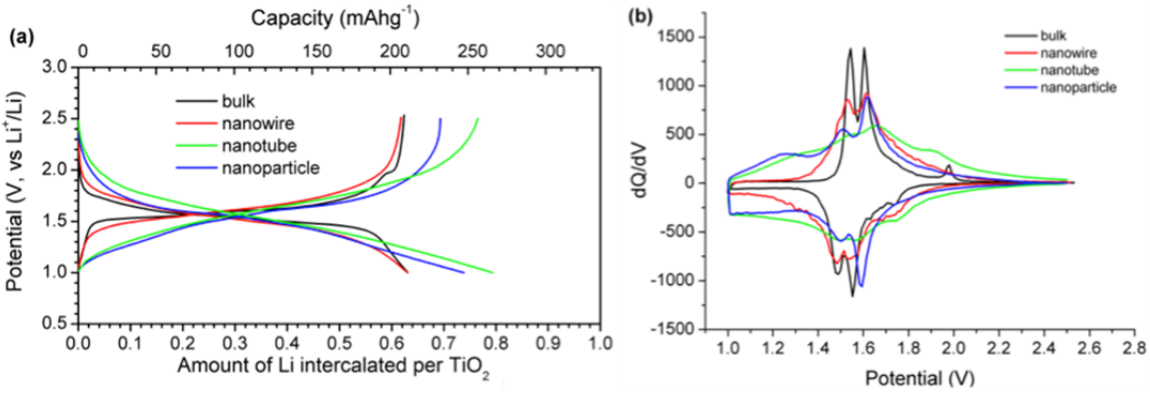

Fig. 4-13 (a) The loading curves of various TiO_2(B) forms. (b) The differential capacity plots of each morphology (The data of nanotubes, nanowires, and bulk are from ref. 4 and ref 9)

Since the first cycle reveals a significant irreversible capacity loss (20%), which is almost certainly due to a side reaction rather than intercalation, a comparison with other forms of TiO_2(B) was made on the second cycle at a slow rate. The second discharge curves are plotted in Fig. 4-13 (a). The data for TiO_2(B) nanotubes, nanowires, and bulk are from previous studies carried out by they St Andrews group[4, 9]. Peaks in the differential capacity plots (Fig. 4-13 (b)) correspond to the plateau in the loading curves. Similarly, all of these load curves have two pairs of plateaus in the range of 1.4 V to 1.65 V. The presence of these plateaus is an indication of 2-phase reactions, due to the intercalation and extraction of Li^+ on A1 and A2 sites of TiO_2(B), according to the previous study[17]. However, the peaks broaden and weaken (i.e, a shift from plateau to slope feature of the load curve plot), as the size of the particles becomes smaller. This transformation in TiO_2(B) nanoparticles and nanotubes implies that the chemical potential of Li^+ intercalated in TiO_2(B) changes continuously with the state of charge, which is not uncommon for the intercalation materials when their size are reduced to several nanometers[18]. This is possibly because the smaller nanostructures are more readily subjected to lattice distortions caused by the insertion of Li^+, and such distortion changes the Li energy in lattice gradually, resulting in the slope feature, or due to the pseudocapacitive behaviour related to the nanomaterials[13].

TiO_2(B) nanoparticles can accommodate about 20% more Li^+ than the bulk or nanowires. It is worth noting that the size of the nanoparticles (3 nm) is similar to the wall thickness of the nanotubes (2.5 nm), and the dimensions of nanowires (35 nm x 5 μ m) are similar to those of bulk (100 nm x 10 μm). No obvious lattice distortion was observed in the pristine nanoparticles while it is significant in the pristine nanotubes[19]. The coincidence of the similarity in particle dimension with that in their capacity, despite whether the overall lattice

is distorted in the pristine structure, indicates that the ability of the nanoparticles to accommodate more Li^+ is mainly a size effect. The additional Li^+ storage of the 3 nm TiO_2(B) nanoparticles compared to the bulk originates primarily from the region below 1.4 V (Fig. 4-13 (b)), where the area below the curves corresponds to the amount of the increased capacity. Such feature does not present in either the bulk or the nanowire form. According to previous study [9, 20] , the reduction of particle size will result in an increased portion of material to appear in the near surface region, where the lattice can be slightly distorted. This is believed to be the reason for extra Li storage for the TiO_2(B) nanotubes, which should also apply to the 3 nm TiO_2(B) particles.

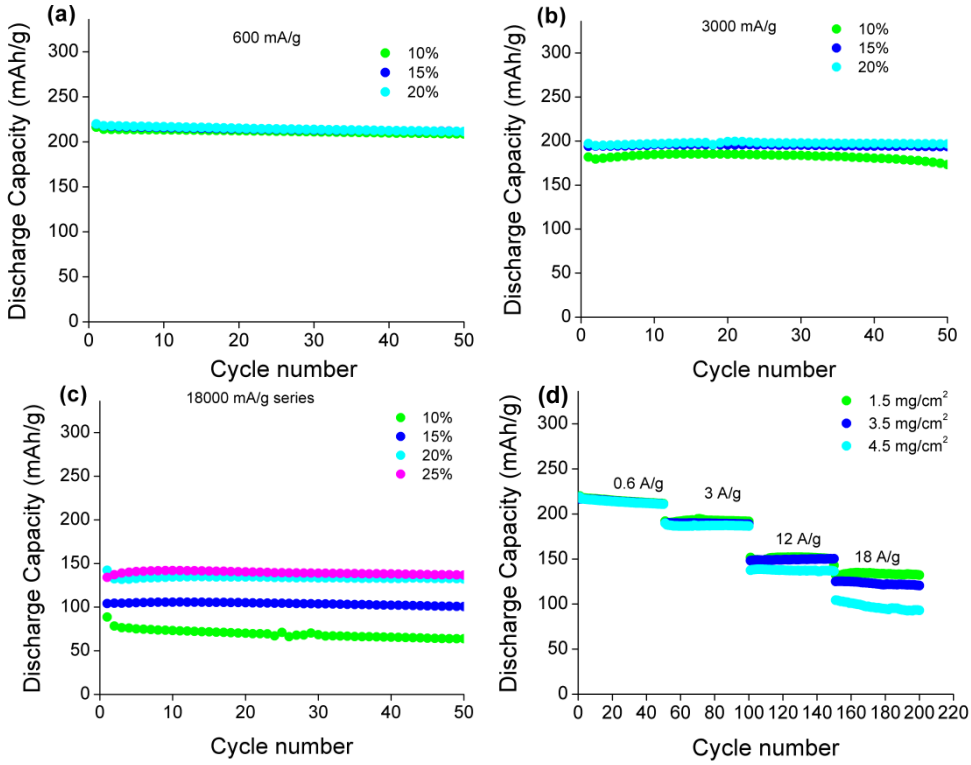

Fig. 4-14 Rate performance. Variation of discharge capacity with cycle number for TiO_2(B) composite electrode. (a)-(c) Consideration of Super P amount at rates of 600 mA/g, 3000 mA/g, 18000 mA/g (mass loading of TiO_2(B) was 1.5 mg/cm^2); (d) Consideration of electrode thickness (20% Super P). The amount of Kynar 2801 was 10%

One of the remarkable advantages of the nanomaterials in Li-ion batteries is their outstanding rate performance. In order to investigate the intrinsic rate performance of TiO_2(B) nanoparticles, one must make sure that the mass loading, the thickness of the electrode, and the percentage of the carbon conductive in the composite electrode are deliberately selected in such a way that the rate capability of the cell depends primarily on the active material itself. The first 50 cycles at different rate with 1.5 mg/cm^2 mass loading of the active material

are presented in Fig. 4-14 (a)-(c), the amount of Super P was adjusted in order to demonstrate the maximum capacity of the active material. The capacity at a high rate depends not only on the intrinsic property of the material, but also on the conductivity of the composite electrode and the electrolyte diffusion inside it. The enhancement is generally achieved by the addition of carbon. No obvious difference was observed in Fig. 4-14 (a) as the carbon amount increased from 10% to 15% and 20% at 600mA/g, indicating that 10% of Super P is adequate to support the cycling at 600 mA/h (2C). However, when the rate rises to 3000 mA/g (10C), Fig. 4-14 (b), the capacity of the cell with 15% and 20% of Super P outperforms the one with 10% of carbon, implying that 15% of Super P is necessary to sustain the performance of the 3 nm TiO_2(B) nanoparticles at this rate. And 20% of Super P is essential for an increasing rate of 18000 mA/g (60C).

The cells demonstrate a reversible capacity of 221 mAh/g at a rate of 600 mA/g and still remain 135 mAh/g at 18000 mA/g without significant capacity fading during cycling. Fig. 4-14 (d) is the consideration of mass loading. 20% of Super P was added to support the high rate performance. High rate performance declines with an increase in the electrode mass (electrode thickness). However, the electrode mass loading can be increased to 3.5 mg/cm^2 for sacrificing only a little capacity under high rates, hence considerably increasing the capacity from the same area of electrode.

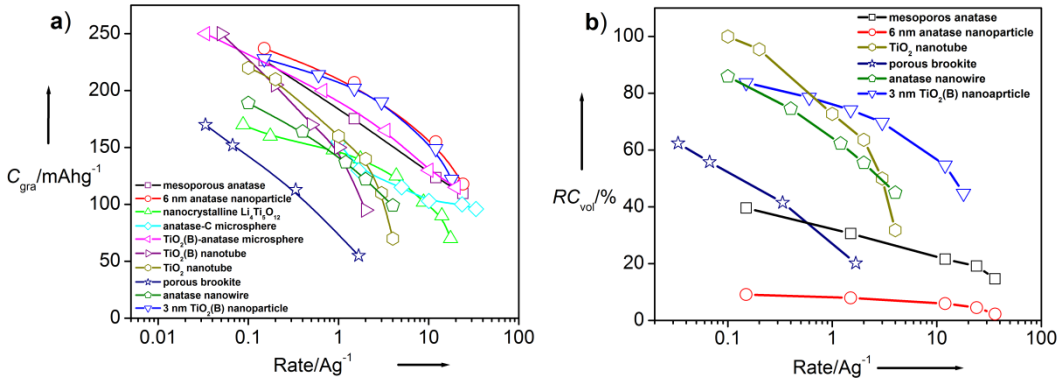

Fig. 4-15 (a) Gravimetric capacity; (b) Relative volumetric capacity. (the low rate discharge capacity of TiO2(B) nanotubes is used as 100%)

One of the major drawbacks of nano materials in Li-ion batteries is their low volumetric capacity due to their low density. In Fig. 4-15, a comparison of different nano titanates is made on both their gravimetric (a) and volumetric (b) capacity. The gravimetric capacity of the 3 nm nanoparticles is on the top of all the other nano forms, and its volumetric capacity wins out significantly for high rates. Their advantage in volumetric capacity is due to the

agglomeration of the 3 nm nanoparticles, which results in a beneficial higher density. Both volumetric and gravimetric capacity of the 3 nm TiO_2(B) show significant advantages as an promising anode material for lithium batteries.

4.3.6 Electrochemistry after surface treatment

As mentioned in the last section, the origin of the irreversible capacity loss (ICL) on the first cycle will be explored. Surface treatment of the TiO_2(B) nanotubes has been established by S. Brutti at el[21] in 2012. In their study, a considerable amount of the irreversible capacity has been removed after the treatment with lithium ethoxide (EtOLi) or n-butyllithium (BuLi), and origin of the irreversible capacity has been investigated. A similar treatment was applied to the 3 nm TiO_2(B). Details for the experiment were described in the experimental section. The first cycles at 50 mA/g of the 3 nm TiO_2(B) under different treatments are compared together with the bulk TiO_2(B) in Fig. 4-16. Their ICLs on the first cycle are listed in Table 4-3.

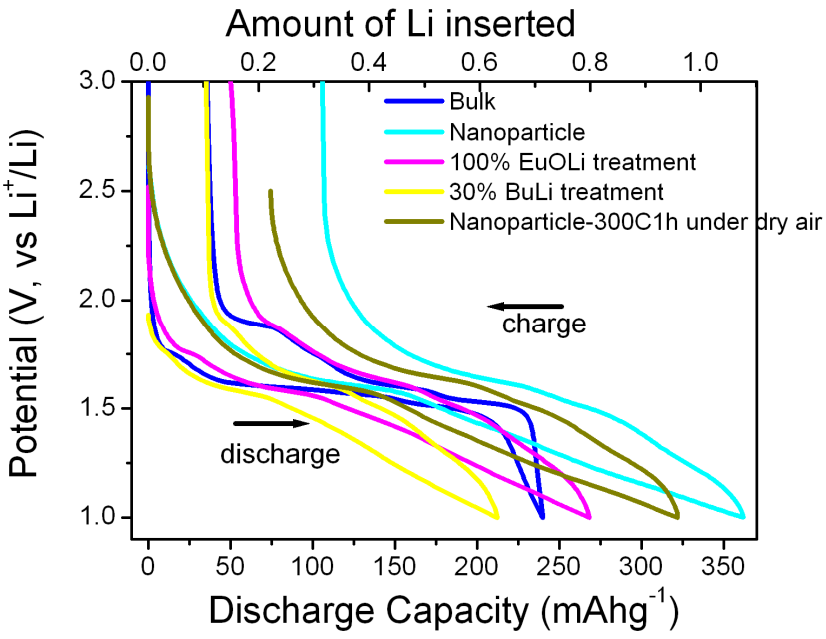

Fig. 4-16 Load curve of TiO_2(B) with or without surface treatment. Rate 50 mA/g.

The irreversible capacity is reduced after surface treatments. These treatments have different functions. Annealing at 300 ^oC under dry air burns away the surface organics (See Table 4-2). EtOLi is a strong base and reacts with the rest of surface -OH groups, resulting in the replacement of H by Li[21]. BuLi serves not only as a strong base but also as a reductant (1 V *vs.* Li^+/Li)[22], meaning that Li^+ will further intercalate into TiO_2(B) lattice after reacting with the –OH groups. Therefore, BuLi neutralizes both surface hydroxyls and irreversible intercalation sites, and the resulting ICL (36 mAh/g) should correspond to the electrolyte

decomposition and SEI formation on the particle surface. A minor difference of 14 mAh/g between the ICL of the EtOLi treated sample (50 mAh/g) and the BuLi one (36 mAh/g) implies that there might be some irreversible lithiation sites in the 3 nm TiO_2(B) nanoparticles. The presence of surface hydroxyls contributes to 25 mAh/g ICL, which is the difference between the ICL of EtOLi treated sample (50 mAh/g) and the one after annealing (75mA/g, the one studied in the last section). Furthermore, the organics on the surface would provide another 31mAh/g ICL if the sample was not subjected to heat treatment.

Table 4-3 Irreversible Capacity Loss and Columbic Efficiency Of The First Cycle Under Different Treatments

Sample	**First discharge (mAh/g)**	**First charge (mAh/g)**	**Irreversible capacity loss (mAh/g)**	**Columbic efficiency**
As prepared	362	256	106	0.71
300 °C annealed*	322	247	75	0.77
EtOLi treated	268	218	50	0.81
BuLi treated (30% intercalation)	253	217	36	0.86

* The surface treatment was based on the 300 ^{o}C annealed sample, which was subjected to the detailed study in the section above.

For the reversible capacity after the treatment, unlike the treatment for TiO_2(B) nanotubes in previous paper[21], it decreases significantly after the surface treatment (See Fig. 4-16). The capacity dropped down to 174 mA/h at the rate of 600 mA/g (Fig. 4-17(a)), a loss of 21% compared with 221 mAh/g at the same rate for the untreated sample, and the high rate performance becomes worse as well (Fig. 4-17(b)-(c)). Adjusting the thickness of electrode also gives rise to a similar result. This may be due to the reduction in electronic conductivity after the surface treatment. More severe reversible capacity loss has been revealed in the BuLi treated sample (Fig. 4-18). This severe overall capacity loss is due possibly to the surface structural change after the reaction, which, discussed in the last section, may relate to the enhanced Li-storage of the nanoparticles. Given that, it is hard to retain a good reversible capacity with the investigated surface treatment, making them not practical for industrial applications. A more proper treating agent needs to be explored in the future.

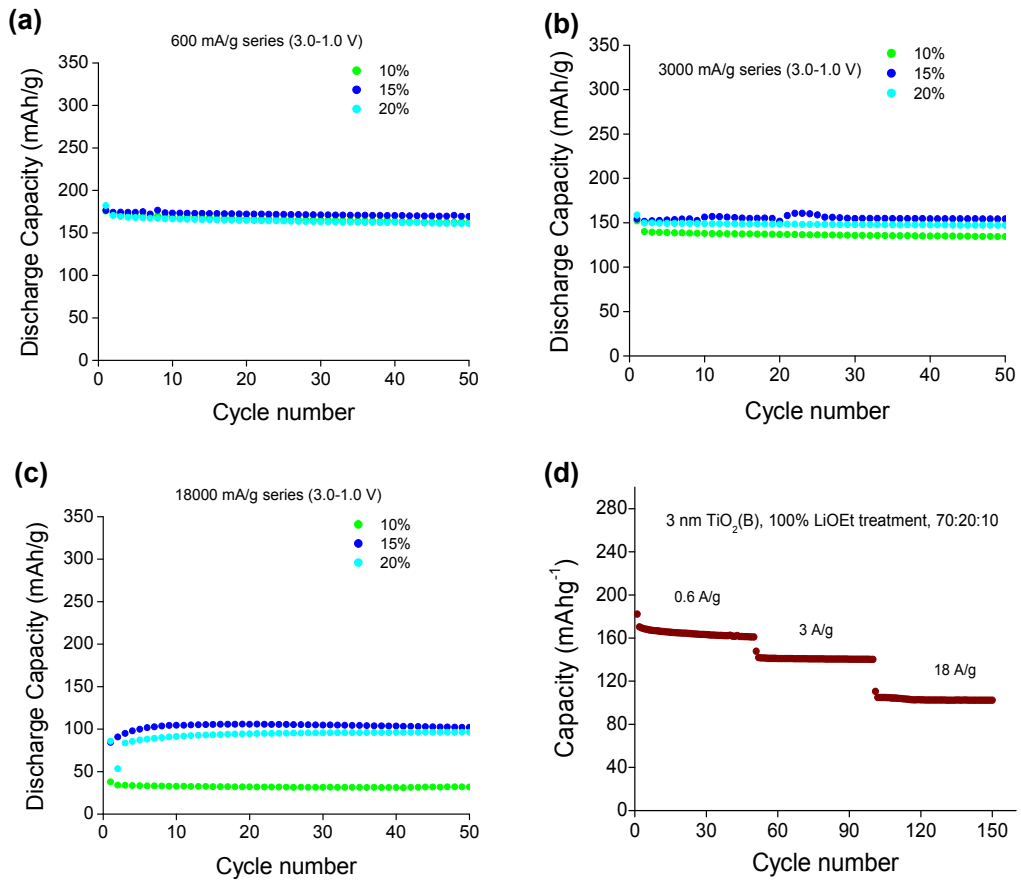

Fig. 4-17 Variation of discharge capacity with cycle number for TiO_2(B) composite electrode. (a)-(c) Consideration of SuperP amount at rates of 600 mA/g, 3000 mA/g, 18000 mA/g; (mass loading of TiO_2(B) was 1.5 mg/cm^2) (d) consideration of electrode thickness (20% Super P). Kynar 2801 was 10% in all the plots

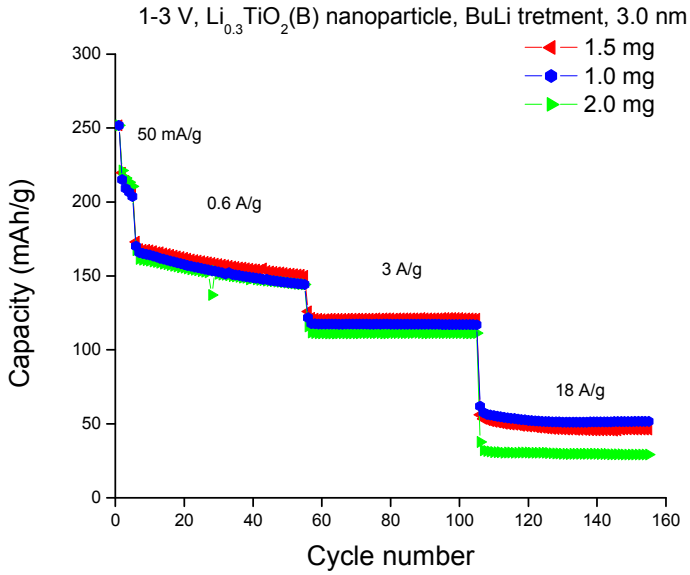

Fig. 4-18 Performance of TiO_2(B) nanoparticle with 30% BuLi treatment. The ratio of TiO_2(B) nanoparticle, Super P carbon, and Kynar 2801 is 70:20:10

4.4 Conclusion

The single-phased TiO_2(B) nanoparticles with the smallest size of 2.5x2.5x4.3 nm have been synthesized by hydrothermal reaction. The surface of this extremely small particle is free of organics and covered by different types of hydroxyl groups. As an anode material for Li-ion batteries, it has demonstrated superior performance for both the gravimetric and volumetric capacity at different rates, exhibiting considerable interest for commercial application.

Reference

1. Marchand, R., L. Brohan, and M. Tournoux, *TiO2(B) a new form of titanium dioxide and the potassium octatitanate K2Ti8O17.* Materials Research Bulletin, 1980. **15**(8): p. 1129-1133.
2. Yazami, R. and P. Touzain, *A reversible graphite-lithium negative electrode for electrochemical generators.* Journal of Power Sources, 1983. **9**(3): p. 365-371.
3. Aurbach, D., et al., *A short review of failure mechanisms of lithium metal and lithiated graphite anodes in liquid electrolyte solutions.* Solid State Ionics, 2002. **148**(3–4): p. 405-416.
4. Armstrong, A.R., et al., *TiO2-B Nanowires.* Angewandte Chemie International Edition, 2004. **43**(17): p. 2286-2288.
5. MacNeil, D.D., Z. Lu, and J.R. Dahn, *Structure and Electrochemistry of Li [Ni x Co1 − 2x Mn x] O 2 (0 ⩽ x ⩽ 1 / 2)* Journal of The Electrochemical Society, 2002. **149**(10): p. A1332-A1336.
6. Dalton, A.S., A.A. Belak, and A. Van der Ven, *Thermodynamics of Lithium in TiO2(B) from First Principles.* Chemistry of Materials, 2012. **24**(9): p. 1568-1574.
7. Inaba, M., et al., *TiO2(B) as a promising high potential negative electrode for large-size lithium-ion batteries.* Journal of Power Sources, 2009. **189**(1): p. 580-584.
8. Zachau-Christiansen, B., et al., *Lithium insertion in isomorphous MO2(B) structures.* Solid State Ionics, 1992. **53–56, Part 1**(0): p. 364-369.
9. Armstrong, G., et al., *Nanotubes with the TiO2-B structure.* Chemical Communications, 2005(19): p. 2454-2456.
10. Jang, H., S. Suzuki, and M. Miyayama, *Synthesis of open tunnel-structured TiO2(B) by nanosheets processes and its electrode properties for Li-ion secondary batteries.* Journal of Power Sources, 2012. **203**(0): p. 97-102.
11. Arrouvel, C., S.C. Parker, and M.S. Islam, *Lithium Insertion and Transport in the TiO2−B Anode Material: A Computational Study.* Chemistry of Materials, 2009. **21**(20): p. 4778-4783.
12. Kobayashi, M., et al., *One-Step Synthesis of TiO2(B) Nanoparticles from a Water-Soluble Titanium Complex.* Chemistry of Materials, 2007. **19**(22): p. 5373-5376.
13. Zukalová, M., et al., *Pseudocapacitive Lithium Storage in TiO2(B).* Chemistry of Materials, 2005. **17**(5): p. 1248-1255.
14. Ben Yahia, M., et al., *Updated references for the structural, electronic, and vibrational properties of TiO2(B) bulk using first-principles density functional theory calculations.* The Journal of Chemical Physics, 2009. **130**(20): p. -.
15. Lin, H., et al., *In situ IR study of surface hydroxyl species of dehydrated TiO2: towards understanding pivotal surface processes of TiO2 photocatalytic oxidation of toluene.* Physical Chemistry Chemical Physics, 2012. **14**(26): p. 9468-9474.
16. Andreev, Y.G., et al., *The Shape of TiO2-B Nanoparticles.* Journal of the American Chemical Society, 2014. **136**(17): p. 6306-6312.
17. Armstrong, A.R., et al., *Lithium Coordination Sites in LixTiO2(B): A Structural and Computational Study.* Chemistry of Materials, 2010. **22**(23): p. 6426-6432.
18. Guo, Y.G., et al., *Superior Electrode Performance of Nanostructured Mesoporous TiO2 (Anatase) through Efficient Hierarchical Mixed Conducting Networks.* Advanced Materials, 2007. **19**(16): p. 2087-2091.

19. Andreev, Y.G. and P.G. Bruce, *Demonstrating Structural Deformation in an Inorganic Nanotube.* Journal of the American Chemical Society, 2008. **130**(30): p. 9931-9934.
20. Hu, Y.S., et al., *High Lithium Electroactivity of Nanometer-Sized Rutile TiO2.* Advanced Materials, 2006. **18**(11): p. 1421-1426.
21. Brutti, S., et al., *TiO2-(B) Nanotubes as Anodes for Lithium Batteries: Origin and Mitigation of Irreversible Capacity.* Advanced Energy Materials, 2012. **2**(3): p. 322-327.
22. Wagemaker, M., et al., *Multiple Li Positions inside Oxygen Octahedra in Lithiated TiO2 Anatase.* Journal of the American Chemical Society, 2002. **125**(3): p. 840-848.

Chapter 5 The Mechanism of O_2 Reduction In Aprotic Li-O_2 Batteries

In this chapter, a novel mechanism of O_2 reduction in aprotic Li-O_2 batteries will be proposed. This mechanism unifies two previous models— Li_2O_2 formation on the electrode surface or in the electrolyte solution—based on the solubility of the intermediate LiO_2 and the applied overpotential. Limited solubility of LiO_2 in the low donor number (DN) solvent, such as acetonitrile, leads to the surface growth of Li_2O_2 film. The intermediate nature of DME is responsible for the significant Li_2O_2 growth via both surface and solution pathways, leading to simultaneous Li_2O_2 film formation and toroidal particle growth from the solution. The high DN solvents, like DMSO and Me-Im, promote the solubility of LiO_2 and hence the solution pathway, resulting in the growth of torodial particles at high discharge potential. However, when the potential is low enough, the electrochemical reduction of O_2^- on electrode surface will become dominant again.

5.1 Introduction

The general conceptions, advantages, and challenges of aprotic Li-O_2 batteries have been introduced in the first chapter. On discharge, O_2 diffuses into the pores of the positive electrode, gets reduced, and binds with Li^+ from electrolyte to form solid Li_2O_2. Fundamental understanding of this process (O_2 reduction) is essential to overcome the onerous challenges of realizing a considerable portion of its theoretical capacity and achieving a sustainable cycleability.

Two competing mechanisms of O_2 reduction and Li_2O_2 growth at the cathode of the Li-O_2 batteries have been proposed, *i.e.*, surface growth[1] and solution growth[2, 3]. Both of these models involve the intermediated superoxide species. In the former, the Li_2O_2 is believed to form on the electrode surface after a second electron reduction of the surface adsorbed $*LiO_2$, leading to the Li_2O_2 film formation, a pure electrodeposition process; In the other model, Li_2O_2 forms in the solution via the disproportionation of the intermediate superoxide anion O_2^- in presence of Li^+, and the rate of disproportionation is based on the Hard Soft Acid Base Theory (HSAB) of Pearson[4]. However, the first model cannot explain the formation of the large toroidal Li_2O_2 particles observed by other researchers[5-7]. And the second model cannot account for many of the observations during discharge, such as varying overpotential in different solvents.

Based on a series of complementary experiments, involving cyclic voltammetry (CV), *in*-situ surface enhanced Raman spectroscopy (*in-situ* SERS), and scanning electron microscope (SEM), a novel theory of O_2 reduction in aprotic Li-O_2 batteries was established and is described here. This universal mechanism includes the previous models as two extremes, and is able to explain the simultaneous film and toroidal particle formation in DME based electrolytes. In this chapter, I will start by discussing studies in each of the solvents, leading to the description of this unified mechanism. Later the mechanism is confirmed again through morphology studies using SEM, and finally, this mechanism is applied to predict the capacity in real lithium O_2 positive electrodes The results indicate that a stable high DN solvent is optimum for Li-O_2 batteries.

5.2 Experimental

5.2.1 Distillation of solvents.

All solvents (from Sigma-Aldrich) were distilled and further dried over 4A molecular sieves for more than 4 days in order to remove the impurities and water. Water content was measured to be below 5 ppm for all the solvents used in this chapter. Me-Im (1-methylimidazole, ≥99%) was distilled under vacuum. DMSO (dimethyl sulfoxide, ≥99.7%) was distilled over $NaNH_2$ under vacuum. DME (dimethoxyethane, 99.9%) was treated with Na and benzophenone overnight and then distilled under argon. And ACN (acetonitrile, ≥99.9%) was distilled over CaH_2 under argon.

5.2.2 Electrochemical measurements.

All Electrochemical measurements were carried out in a N_2-filled glovebox using a VMP3 workstation (Biologic). A pre-charged $LiFePO_4$ (LFP) composite electrode (pre-charged to *ca.* 20% of its capacity, which gives a fixed potential of 3.45 V vs. Li^+/Li) was placed in the solution of 0.1 M $LiClO_4$ (battery grade 99.99%, Sigma-Aldrich) in DMSO behind a porous frit, served as the reference electrode. A platinum wire was used as the counter electrode. A 2 mm Au disk electrode (BAS Inc.) was employed as the working electrode, polished with 0.05 μm alumina/ ethanol slurry before each electrochemical measurements. All electrolytes were saturated with O_2 (N6.0 grade, BOC) by O_2 bubbling for over 5 min. The rotating ring-disk electrode (RRDE) measurement was carried out with a MSR rotator and the electrode contains a 5 mm Au disk and a glassy carbon ring.

5.2.3 *In-situ* surface enhanced Raman spectroscopy (*In-situ* SERS).

In-situ SERS was carried out in an air-tight electrochemical cell equipped with a high purity sapphire window for Raman detection. An Au electrode was roughened electrochemically by repeated oxidation and reduction in the 0.1 M KCl solution. Raman spectra were collected using a confocal Raman microscope with 785 nm diode laser.

5.2.4 Morphology of Li_2O_2

Porous carbon composite electrodes were used to explore the Li_2O_2 morphology after discharge in various solvents at specific potentials. The electrodes were prepared by casting the slurry of 90wt% carbon black (Super P, Timcal Inc.) and 10wt% PTFE onto a 60-mesh stainless steel mesh. Potentiostatic discharge was carried out in an airtight 3-electrode glass cell with pre-charged $LiFePO_4$ as reference electrode and normal $LiFePO_4$ with adequate capacity as counter electrode. After washing with acetonitrile in glovebox, the sample was dried and transferred into FE-SEM (JSM-6700F, JEOL) with a very short exposure to air (generally less than 15 seconds) for direct observation of Li_2O_2 morphology.

5.3 Result and Discussion

5.3.1 Analysis of ORR in Li^+ containing solvents

Electrochemical analysis of ORR in various solvents. The evolution of the cyclic voltammograms (CVs) in four distinct solvents according with varying Li^+ concentration is presented in Fig. 5-1. The cation varied gradually from TBA^+ (tetrabutylammonium) to Li^+ with a fixed total concentration of $[Li^+]+[TBA^+]= 0.1$ M. Without the presence of Li^+, the CVs in all the four solvents demonstrate a similar feature, a single redox process. However, the introduction of Li^+ has different impacts on the CVs depending strongly on the donor number (DN) of the solvents. In high DN solvents such as Me-IM (DN=47, determined by ^{23}Na NMR), and DMSO (DN=30), the first reduction peak remains with only a minor shift to more positive potential while a new reduction peak appears at negative position and shifts to more negative potential extensively, *i.e.*, the position of this peak is highly dependent on the Li^+ concentration. At high Li^+ concentration, no oxidation peak is observed below 3 V, which is consistent with previous reports[3]. In low DN solvents, a new reduction peak appears at more positive position,

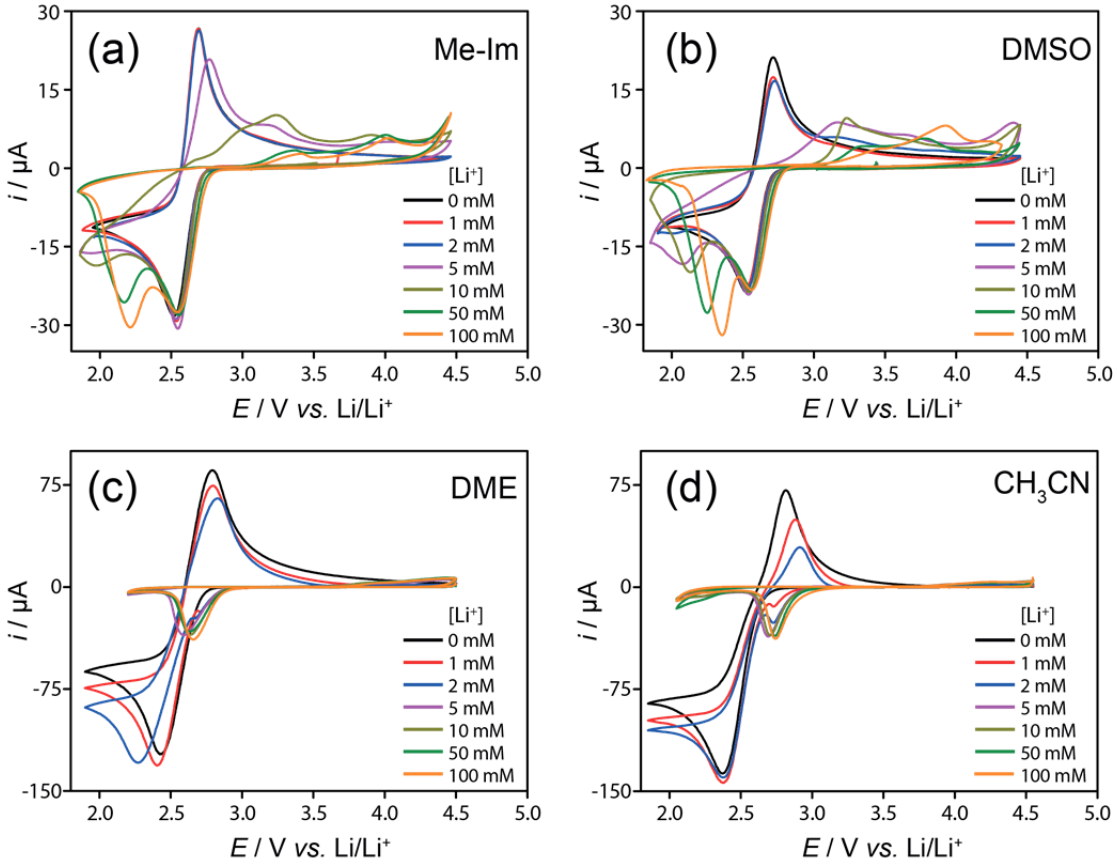

Fig. 5-1 The variation of the CVs with increasing Li^+ concentration in four different solvents. (a) Me-Im, (b) DMSO, (c) DME, and (D) CH_3CN. All data were collected on Au electrode with a scan rate of 100 mV/s. The total concentration of $[Li^+]+[TBA^+]= 0.1$ M in each of the solvents.

which replaces the previous cathodic peak completely at higher Li^+ concentration. These observations are in in good agreement with previous studies. Although some information can be deduced from the CVs itself, the more reliable analysis is given in later sections with a combination of spectroscopic data.

5.3.2 Combined study of electrochemical and spectroscopic analysis in each solvent

High DN Solvents (Me-Im and DMSO). It is well established that the O_2 redox reaction in TBA^+ electrolytes involves a reversible one-electron process between O_2 and O_2^-[8, 9]. In order to understand this process in the presence of Li^+ explicitly, the CVs in high DN solvents (Me-Im and DMSO) were re-collected under the same concentration condition, but within a limited potential range, excluding the second reduction peak. The results are plotted

in Fig. 5-2. No obvious discrepancy is observed among the CVs collected at different Li^+ concentration, implying that Li^+ in these high DN solvents plays a similar role as TBA^+ cation, which doesn't bind O_2^-, *i.e.*, LiO_2 is soluble. This is confirmed by the simulation using BASi DigiSim software, in which all the CVs can be fitted excellently with a one-electron redox model of diffusible species (See Fig. 5-3). The only minor shift towards more positive potential with the increased Li^+ concentration indicates that Li^+ is able to interact with O_2^- weakly, *e.g.*, via solvent separated ion pair, contact ion pair, or some soluble clusters[10].

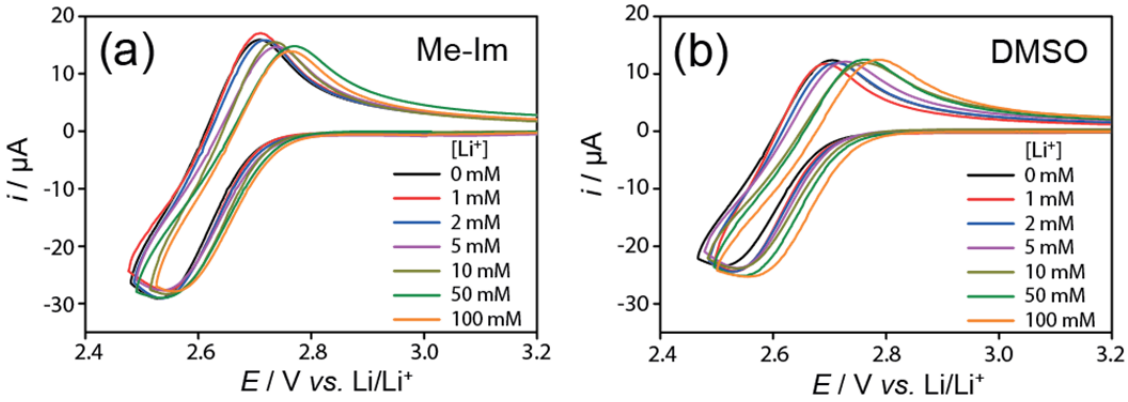

Fig. 5-2 Shift of the first reduction peak in high DN solvents. (a) Me-Im, (b) DMSO. All data were collected on Au electrode with a scan rate of 100 mV/s. The total concentration of $[Li^+]+[TBA^+]$= 100 mM in each of the solvents.

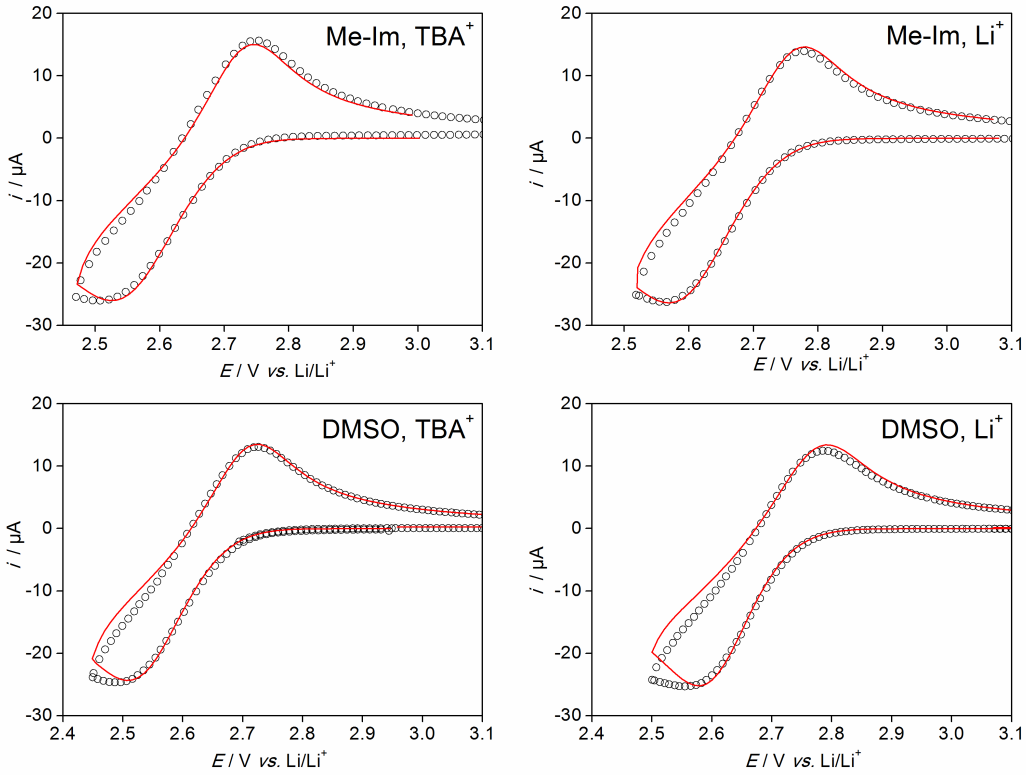

Fig. 5-3 Fits of CVs at high scan rate. The red lines shows the best fits of the CV curves and the black circles are experimental data. The data were collected on Au electrode with a scan rate of 100 mV/s. The concentration of cations is 100 mM in each of the solvents.

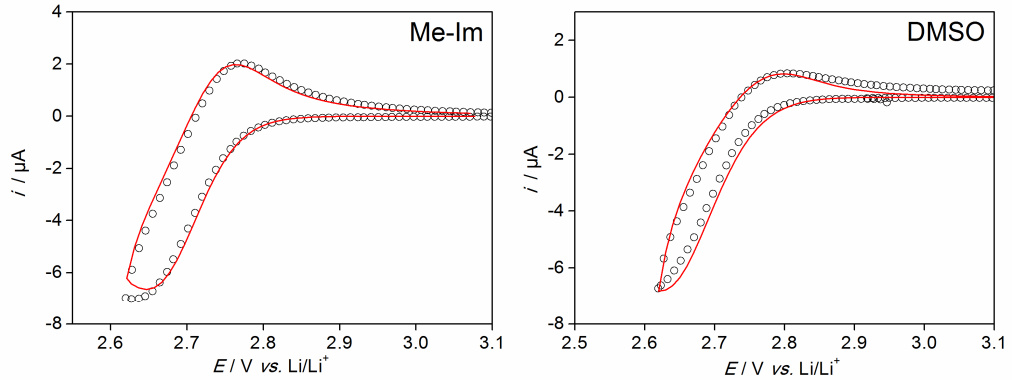

Fig. 5-4 Fits of CVs at low scan rate. The red lines shows the best fits of the CV curves and the black circles are experimental data. The data were collected on Au electrode with a scan rate of 5 mV/s. The concentration of cations is 100 mM in each of the solvents.

The coexistence of Li^+ and O_2^- generally results in Li_2O_2 formation by the disproportionation of O_2^- ($2Li^+ + 2O_2^- \rightarrow Li_2O_2 + O_2$)[2]. The chemical process should also appear during the CV scans. However, the successful fitting with pure electrochemical process suggests that the scan rate of 100 mV/s is much faster comparing to the rate of chemical disproportionation. In

order to reveal the chemical process, the scan rate was reduced to 5 mV/s using the same voltage range in both of the electrolytes with $[Li^+]$ = 0.1 M. The ratio of the oxidation peak to the reduction peak is reduced significantly (See Fig. 5-4), indicating that the O_2^- generated during reduction has undergone disproportionation. The simulation was carried out with an E-C model, that is, an electrochemical process followed by a chemical one. The standard heterogeneous electron transfer rate constant (k^0) of the electrochemical process, concentration of O_2, and the diffusion coefficient (D) were derived from the simulation of the 100 mV/s CV, and the rate of the following chemical step was considered as the first order of $[O_2^-]$. Some valuable parameters obtained from the simulation are listed below in Table 5.1. It is noteworthy that the disproportionation rate in Me-Im (DN=47) is lower than that in DMSO (DN=30), for the reason that the more intensive binding of $[Li^+]$ in high DN Me-Im gives rise to lower Li^+ activity, which results in the slower disproportionation.

Table 5.1 The Diffusion coefficient and electron transfer rate constant in high DN solvents

		5.3.3 10^5 x D / $cm^2\ s^{-1}$	**5.3.4 10^3 x k^0 / $cm\ s^{-1}$**
5.3.5	**Me-Im**		
5.3.6	$TBAClO_4$	5.3.7 9.49	5.3.8 2.72
5.3.9	$LiClO_4$	5.3.10 10.4	5.3.11 2.75
5.3.12	**DMSO**		
5.3.13	$TBAClO_4$	5.3.14 8.6	5.3.15 2.34
5.3.16	$LiClO_4$	5.3.17 8.9	5.3.18 2.34

Look back to the second cathodic peak in Fig. 5-1, which is now assigned to the second electron reduction of O_2, leading to Li_2O_2 formation electrochemically. The process can be described by the following equation in high DN solvents,

$2Li^+ + O_2^- + e^- \rightleftharpoons Li_2O_2$.

The involvement of Li^+ in this reaction is responsible for the prominent negative shift of the second reduction peak by *c.a.* 300 mV in Fig. 5-1 when the Li^+ concentration varied from 1 mM to 100 mM. The standard potential for this reaction ($E_2^{\ominus}$) cannot be read directly from Fig. 5-1, as a result of the asymmetric peaks. However, it can be calculated by employing the standard potential of O_2/O_2^- ($E_1^{\ominus} = 2.65\ V$) obtained from Fig. 5-2 and the standard potential of the overall reaction ($2Li + 2O_2 \rightleftharpoons Li_2O_2 + O_2, E_{total}^{\ominus} = 2.96\ V$) obtained from literature[11]. The $E_2^{\ominus}$ is located at a considerable high potential of 3.27 V. Although thermodynamically, the second electron reduction should appear right after the formation of O_2^-, the slow kinetic of the second reduction renders the noticeable cathodic current of the second reduction occurring at much lower potential (See Fig. 5-1). In fact, if the kinetic of the second electron reduction were fast, we should NOT be able to observe the chemical reversibility in Fig. 5-2 and the reduction peak should be close to 2-electron process. The reason why this step is slow still remains unclear.

In order to demonstrate the process more explicitly, rotating ring-disk electrode measurement was employed. Presented in Fig. 5-5, the RRDE data confirms both surface film formation at low voltage and the presence of the soluble O_2^- species. In contrast to CV, the current on the rotating disk is controlled by the solution flow rather than diffusional limitation. The current decrease at lower potential provides evidence of the film formation on the electrode surface. Since if there is no insoluble and nonconductive species formed on electrode surface, the current should remain at a static value as the potential decreases. The potential of the ring is held at a certain value so that O_2^- can be oxidized. Hence, the ring current (corrected according to the collection efficient, shown in Fig. 5-5 as the green region) is proportional to the amount of O_2^- generated at the disk during the measurement. Another important bit of information is that the difference between the current of the disk and that of the ring is associated with the surface Li_2O_2 formation electrochemically (red shaded region in Fig. 5-5). The results of DMSO and Me-Im suggest that the Li_2O_2 formation via electrochemical reduction occurs even at high potential but the rate is very slow. Noteworthy, in the second electron reduction is more difficult in Me-Im than in DMSO because higher DN solvent binds Li^+ more strongly, hindering the electrochemical reduction process $2Li^+ + O_2^- + e^- \rightleftharpoons Li_2O_2$, which involves Li^+.

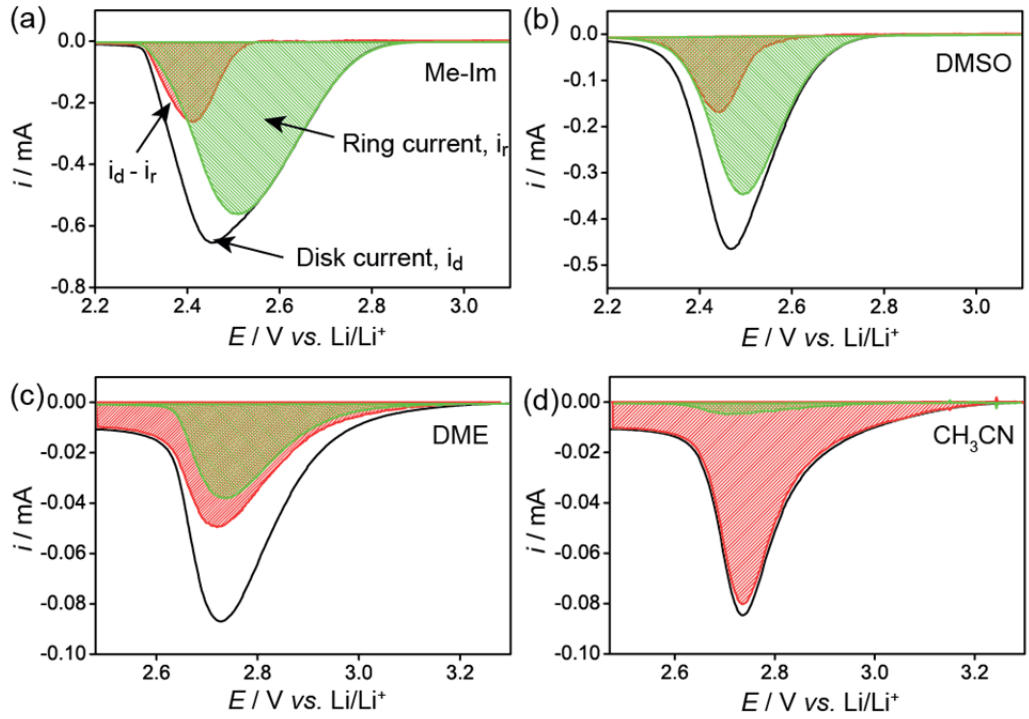

Fig. 5-5 Rotating ring-disk electrode (RRDE) experiments demonstrating the presence of O_2^- in different solvents. (a) Me-Im, (b) DMSO, (c) DME, (d) CH_3CN. The concentration of Li^+ is 100 mM. The rotating rate was 2000 rpm. The green area stands for the ring current, associated with the soluble O_2^-, and black line is the disk current, the difference between these two is presented by the red area, corresponding to the insoluble surface species.

Though the analysis of these electrochemical data has provided us an excellent illustration of the undergoing electrochemical process, a more reliable confirmation of the chemical species involved is made by the *in-situ* surface enhanced Raman spectroscopy (*in-situ* SERS). The spectra were collected in different solvents under specific potentials shown on Fig. 5-6. Starting from DMSO, SERS reveals no evidence of LiO_2 on the electrode surface at any potential and any time. At the highest potential (low overpotential, See Fig. 5-6 the red spectra of DMSO), a very weak signal of Li_2O_2 is identified after the longer acquisition time. This may be due either to the second electron reduction or to the crystallization of chemically generated Li_2O_2 on the electrode surface. The more detailed explanation is given below. The standard potential of the second reduction is 3.27 V. Even though the process is kinetically slow, from the thermodynamic point view, it is still allowed, in accord with the RRDE data. The other possibility is that a small portion of the Li_2O_2 formed via disproportionation in solution phase might nucleate and deposit on the electrode surface. With longer acquisition

time, the signal of the Li_2O_2 increases and that of O_2^- decreases. This is because the growth of Li_2O_2 on electrode surface blocks more and more available surface for O_2^- adsorption. The similar behavior is observed on lower potential (blue spectra in Fig. 5-6). At lowest potential (green spectra), significant amount of Li_2O_2 forms on the electrode surface within only 15 second. This potential, highlighted as a green dot on the CV of DMSO in Fig. 5-6, is associated with the second reduction peak, at which O_2^- can rapidly pick up an electron from the electrode to form Li_2O_2 in the presence of Li^+. The results of SERS for Me-Im are similar to that of DMSO. However, a solvent peak at the region of O_2^- and LiO_2 makes it less valuable. The weaker signal of Li_2O_2 at the highest potential after 3 min than that in DMSO, in good agreement RRDE, implies that the second electron reduction is slower and more difficult in higher DN solvent.

Up to now, the mechanism in high DN solvent has been established. The overall process can be described as follow,

Step 1 $O_2 + e^- \rightleftarrows O_2^-$,

Step 2a $2Li^+ + 2O_2^- \rightleftharpoons Li_2O_2 + O_2$ (high voltage, chemical disproportionation)

Step 2b $2Li^+ + O_2^- + e^- \rightleftharpoons Li_2O_2$ (low potential, second electron reduction)

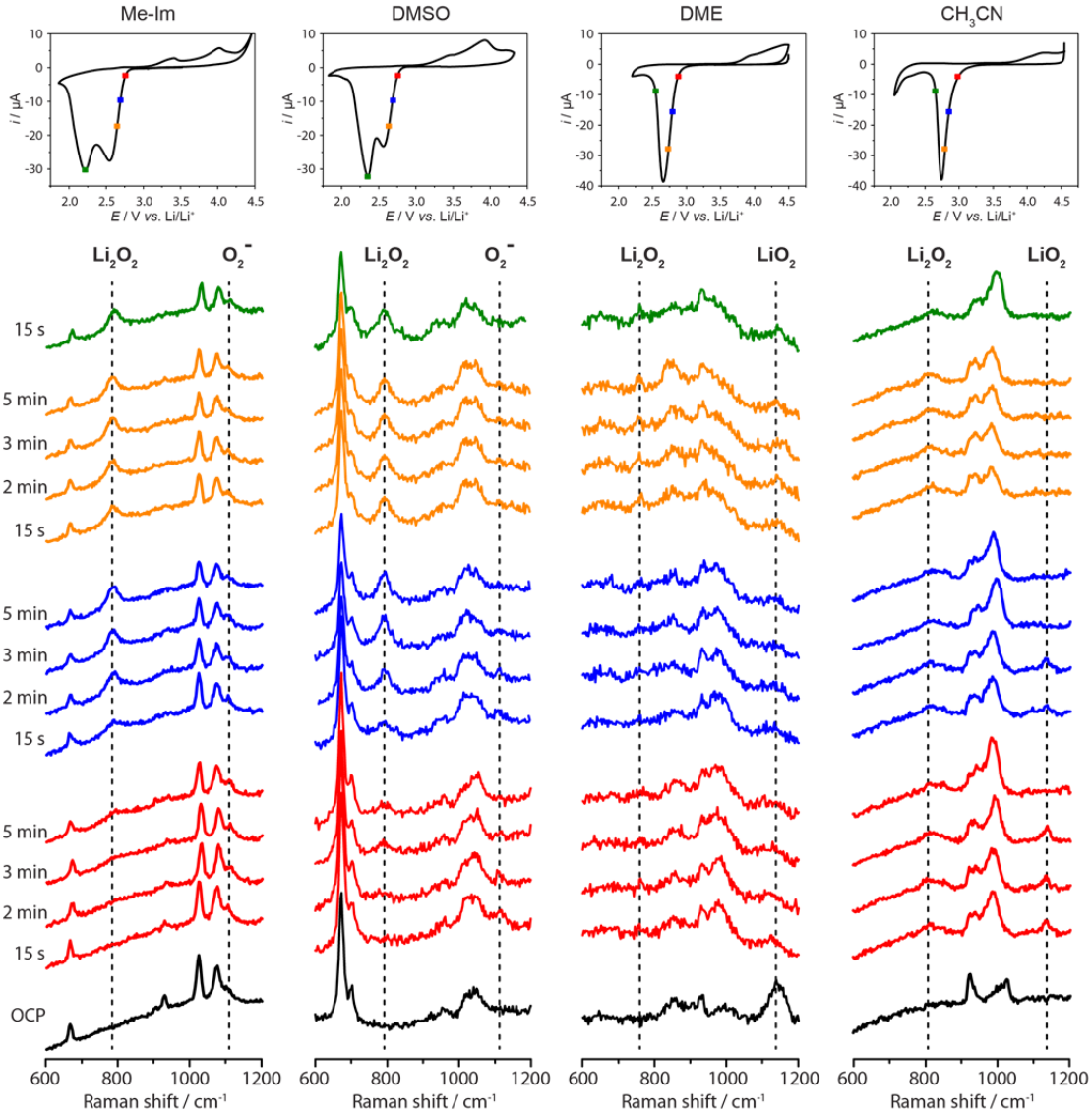

Fig. 5-6 The presence of O_2^-, LiO_2, and Li_2O_2 on the electrode surface and the changes over time revealed by *In-situ* surface enhanced Raman Spectra (*in-situ* SERS). The spectra were collected at roughen gold surface in each of the solvents. The concentration of Li^+ is 100 mM. The potential held at the colored lines correspond to the points with the same color in the CV scans.

Low DN solvent (Acetonitrile, CH_3CN). The CVs of the lowest DN solvent (CH_3CN, DN=14) exhibits a different feature compared to those of DMSO and Me-Im. A new reduction peak occurs at more positive potential as TBA^+ is replaced by Li^+. Instead of shifting to negative position, which is observed in the high DN solvent, this peak grows in intensity with the increasing Li^+ concentration and dominates after the Li^+ concentration reaches 5 mM, in the meantime, the original peak disappears (See Fig. 5-1), implying that a

more stable species is formed instead of O_2^-. SERS reveals no evidence of O_2^- at any potential and any time, but confirms the presence of LiO_2 on the electrode surface, consistent with the surface growth mechanism. The peak of Li_2O_2 appears immediately after 15 second at any potential, indicating that the second electron transfer ($LiO_2 + Li^+ + e^- \longrightarrow Li_2O_2$) and/or the disproportionation ($2LiO_2 \longrightarrow Li_2O_2 + O_2$) is fast. Lower potential promotes the conversion rate from LiO_2 to Li_2O_2 by increasing overpotential of the second reduction and/or the surface concentration of LiO_2 and hence the rate of disproportionation. The RRDE result (Fig5-5(d)) shows very little contribution from the O_2^- in the solution phase, due to the very limited solubility of LiO_2 in CH_3CN.

Intermediate DN solvent (DME). The DN of DME is 20, lying right between those of CH_3CN and DMSO. The CVs (Fig. 5-1 (c)) are similar to those of CH_3CN, but with a broader peak. The RRDE result (Fig. 5-5 (c)) demonstrates that the reduction products comprise significant amount of both soluble and insoluble species. A broad solvent peak in the regions of LiO_2 and O_2^- in SERS again makes the result badly resolved. Nevertheless, the evident growth in intensity of this peak, combined with the RRDE result, is enough to infer the adsorption of LiO_2 on the electrode surface. LiO_2 has an intermediate solubility in DME. The growth of Li_2O_2 on the electrode surface is observed in SERS, slower than CH_3CN, but faster than DMSO. The above results imply that O_2 reduction in DME involves both surface pathway—insoluble LiO_2 on the surface and solution pathway—soluble O_2^- in the electrolyte.

Summary of the four solvents. The combined studies of electrochemistry and spectroscopy on these four solvents manifest that the mechanism of O_2 reduction involves the insoluble LiO_2 as an intermediate in low DN solvent (CH_3CN), which transforms into its soluble form (solvated Li^+ and O_2^- in the solution) in high DN solvent (DMSO and Me-Im). DME, which has an intermediate DN, sits in the middle and significant amount of LiO_2 and O_2^- presents during the reduction—a switch point from the surface mechanism to the solution pathway. This gradual change from one pathway to another indicates that these two pathways are not distinct ones, but strongly correlated.

5.3.19 The unified mechanism

The main divergence between the solution pathway and surface pathway involves the status of the intermediate LiO_2. Therefore, a new unified mechanism is proposed based on the solubility of LiO_2, or more precisely, the standard Gibbs free energy ($\Delta G^{\ominus}$) of the following equilibrium:

$* LiO_2 \rightleftharpoons Li^+_{(solv)} + O^-_{2(solv)}(+ion\ pairs + clusters)$, Eq (1)

This equation simply stands for the equilibrium between the LiO_2 solid adsorbed on the electrode surface (on the left hand of the equation) and the LiO_2 dissolved in the solution (on the right hand of the equation), which, according to previous reports may embrace solvated ionic Li^+ and O_2^-, ion pairs, and dissolved LiO_2 clusters[10, 12]. The first reaction in all solvents involves one electron reduction of O_2 to **LiO_2 (the double star notation here indicates that the products includes all possible forms of LiO_2—LiO_2 solid on the electrode surface and the soluble species in the solution.). If $\Delta G^{\ominus} \gg 0$, the equilibrium shifts to the left side, LiO_2 forms on the electrode surface, then undergoes the second electron reduction or chemical disproportionation, resulting in the surface Li_2O_2 film formation, which is what we have observed in the low DN solvent. If $\Delta G^{\ominus} \ll 0$, the equilibrium shifts to the right side, then solution mechanism takes over. The dominant following reaction at high potential is the disproportionation of the O_2^- (or LiO_2 clusters) in the solution in the presence of the solvated Li^+, leading to the Li_2O_2 particulate growth from the solution phase. However, if the potential becomes low enough, the second electron reduction ($2Li^+ + O_2^- + e^- \rightleftharpoons Li_2O_2$) will become more favorable, driven by the high overpotential, Li_2O_2 will again form on the electrode surface. This situation has been observed in the high DN solvents. If $\Delta G^{\ominus} \cong 0$, it is possible that LiO_2 is present as both a solid and in dissolved form, leading to both surface and solution growth of Li_2O_2, which is the case of DME. A more clear illustration is given jn the following equations. The morphology of the Li_2O_2 will be discussed in detail in later section.

Step 1: $O_2 + e^- \rightleftarrows O_2^-$ ($\Delta G^{\ominus} \ll 0$, high DN solvents),

$O_2 + e^- + Li^+ \rightleftarrows * LiO_2$ ($\Delta G^{\ominus} \gg 0$, low DN solvents)

Step 2:

For high DN solvents,

$2Li^+ + 2O_2^- \rightleftharpoons Li_2O_2 + O_2$ (high voltage, chemical disproportionation)

$2Li^+ + O_2^- + e^- \rightleftharpoons * Li_2O_2$ (low potential, second electron reduction)

For low DN solvents,

$* LiO_2 + Li^+ + e^- \rightleftharpoons * Li_2O_2$ (at all potential, second electron reduction)

$2 * LiO_2 \longrightarrow * Li_2O_2 + O_2$ (at all potential, chemical disproportionation)

The * denotes the surface adsorbed species.

Gutmann donor number is a quantitive measure of Lewis basicity, hence it is reasonable to be used as an indicator of solvation capability of the solvents. A higher DN generally leads to

stronger solvation of Li^+, pushing the equilibrium forward and leading to solution pathway, and vice versa. Although the value of DN can provide us a clue to the O_2 reduction pathway in different solvents, it is merely based on the enthalpy of the formation of a1:1 adduct between the solvent molecule and $SbCl_5$, the entropy term is not included. Furthermore, the strength of this adduction may not entirely apply to that of Li^+, whose coordination number varies in different solvents. Lastly, the interaction between anion and solvent is not in consideration. Hence, the value of $\Delta G^{\ominus}$ serves as a more powerful tool for the prediction of the equilibrium direction.

5.3.20 The estimation of Gibbs free energy for the dissolution reaction.

The estimation of $\Delta G^{\ominus}$ of Eq (1) is based on the following 3 equations:

$$Li_{(s)} + O_{2(solv)} \rightleftharpoons Li^+_{(solv)} + O^-_{2(solv)}(+ion\ pairs + clusters) \quad \text{Eq (2)}$$

$$O_{2(g)} \rightleftharpoons O_{2(solv)} \quad \text{Eq (3)}$$

$$LiO_{2(s)} \rightleftharpoons Li_{(s)} + O_{2(g)} \quad \text{Eq (4)}$$

Eq (1) is obtained by the summation of these three equations, and $\Delta G^{\ominus} = \Delta G_2^{\ominus} + \Delta G_3^{\ominus} + \Delta G_4^{\ominus}$. $\Delta G_2^{\ominus}$ is calculated by two half-cell reaction according to $\Delta G^{\ominus} = -nFE^{\ominus}$. The standard electrochemical potential $E^{\ominus}_{O_2/O_2^-}$ of $O_{2(solv)}/O^-_{2(solv)}$ couple was measured in the presence of $TBAClO_4$ in each of these solvents; the standard electrochemical potential $E^{\ominus}_{Li^+/Li}$ of $Li_{(s)}/Li^+_{(solv)}$ couple was obtained in the presence of $LiClO_4$, the pre-charged $LiFePO_4$ was used instead of Li, due to the Li instability in all these solvents. The reference electrode is the same as the one described in the experimental sections, 3.45 V vs. Li^+/Li in DMSO. $\Delta G_3^{\ominus}$ is derived by the equilibrium $O_{2(g)}$ pressure in the headspace and $O_{2(solv)}$ concentration in the solvents[13]. $\Delta G_4^{\ominus}$ is a known value of -221 kJ·mol^{-1} according to the first principle calculation[14]. The $\Delta G^{\ominus}$ calculated in this way is only an approximation for the 2 reasons. Firstly, $\Delta G_2^{\ominus}$ is derived from 2 half-cell reactions, in which the Li^+-O_2^- interaction, the possible species in the parentheses in Eq (1), is not included, considering the solvent-cation and solvent-anion interactions are the main contribution to the dissolution. Secondly, the $\Delta G_4^{\ominus}$ is obtained based on first principle calculation, and the free energy of the LiO_2 nanofilm on the electrode surface may deviate from that of its bulk form, but the film to bulk deviation should be similar in different solvents due to the similar morphology. So it does not affect the prediction of the trends. The values of $\Delta G^{\ominus}$ are listed in Table 5.2. It is noteworthy that DME has a $\Delta G^{\ominus}$ of 25 kJ·mol^{-1}, the equilibrium of Eq (1) should shift to the

left side, that is, the surface pathway. But a maximum value of 0.4 mM of O_2^- in the solution phase is predicted (using 100 mM Li^+), indicative of the simultaneous solution pathway, in good agreement with the experimental results. All the calculations predict the correct trends, and this method should be applicable to unknown solvents.

In later sections, high/low/intermediate DN will still be used to refer to different solvents for convenience.

Table 5.2 The standard free energy change of the LiO_2 dissolution reaction

Solvent	DN	$\Delta G^{\ominus}$
CH_3CN	14	36
DME	20	25
DMSO	30	-20
Me-Im	47	-26

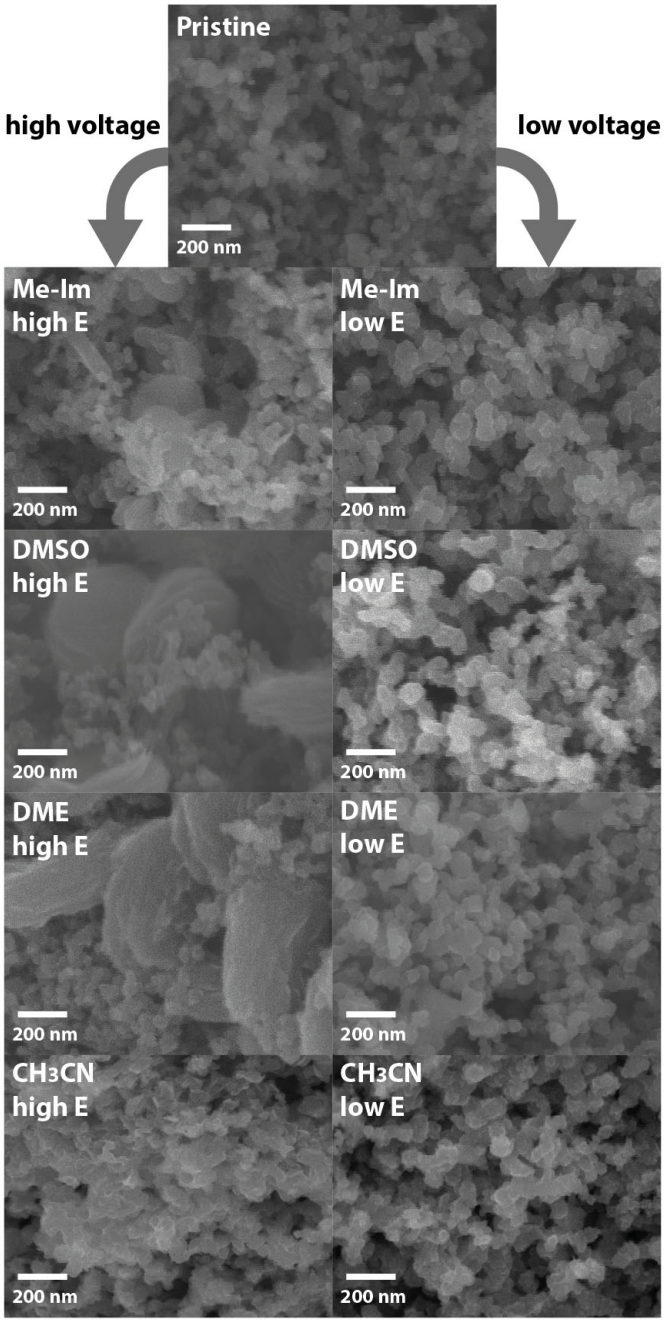

Fig. 5-7 SEM images obtained in different solvents at different potentials with composite carbon electrode, demonstrating the morphology evolution in response to the variation of the discharge potentials. The high E and low E correspond to the highest and lowest potential points on the CVs of Fig. 5-6.

5.3.21 The morphology of Li_2O_2.

After understanding the mechanism of O_2 reduction through the analysis of electrochemical and spectroscopic data, it is also important to examine the morphology of the Li_2O_2 as a result of different pathways in these solvents. The experiments were performed on composite carbon electrodes for the following three reasons. Firstly, the observation of Li_2O_2 particles (from solution pathway) in porous electrode is much easier than that on planar electrode, since the Li_2O_2 trapped in the pores is more stationary while that attached on electrode surface can detach and be removed during the rinsing with CH_3CN. Secondly, it proves the mechanism is (inert) cathode invariant. That is, if the mechanism is correct and universal, it should apply to all inert cathode materials, the Li_2O_2 morphology might be different, due to different nucleation sites on different substrates, but Li_2O_2 should always be big particles if the growth is from the solution. Finally, it is of considerable importance to look at a practical cell. The discharge was carried out as described in the experimental section. The potentials of the potentiostatic discharge corresponded to the points on CV curves in Fig. 5-5. The FE-SEM images of the discharged electrodes in the four solvents at the highest and lowest potentials are presented in Fig. 5-7. In excellent agreement with the mechanism, the characteristic toroidal Li_2O_2 particles/agglomerates[6] are dispersed among the porous structure of the carbon electrode in high DN solvents, Me-IM and DMSO, at high potential. At low potential, no particles are identified, but FTIR reveals the presents of Li_2O_2 (See Fig. 5-8). Together with SERS and electrochemical data, it implies that Li_2O_2 forms on the carbon surface, as a result of the prompt second electron reduction. In CH_3CN, there is no evidence of Li_2O_2 particle formation at any potential, consistent with surface pathway of the unified mechanism. In DME, the Li_2O_2 is observed at high potential due to the mixed nature of both solution and surface pathways.

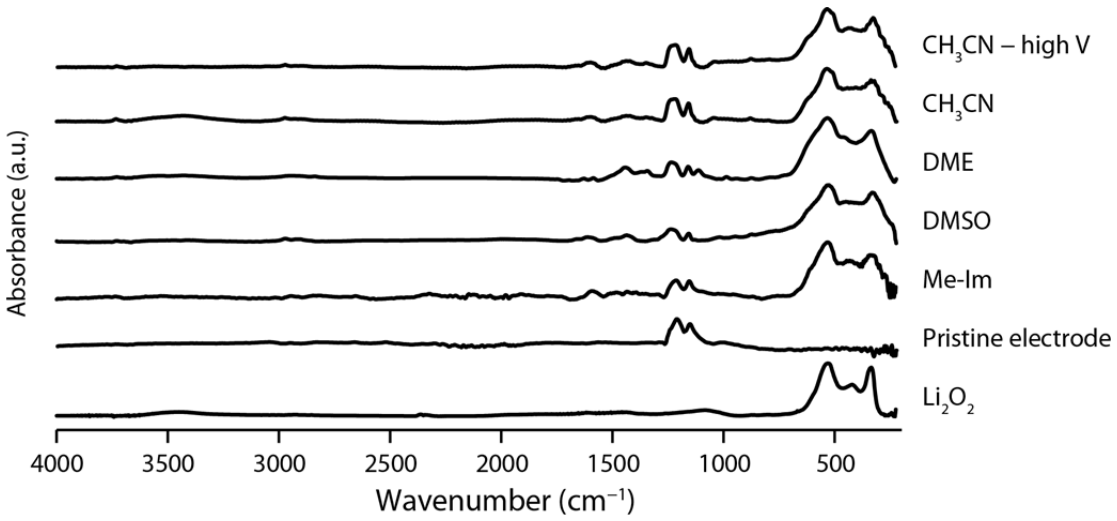

Fig. 5-8 FTIR spectra of the lowest potential discharged electrode in the different solvents, demonstrating the presence of Li_2O_2, which cannot be detected by SEM.

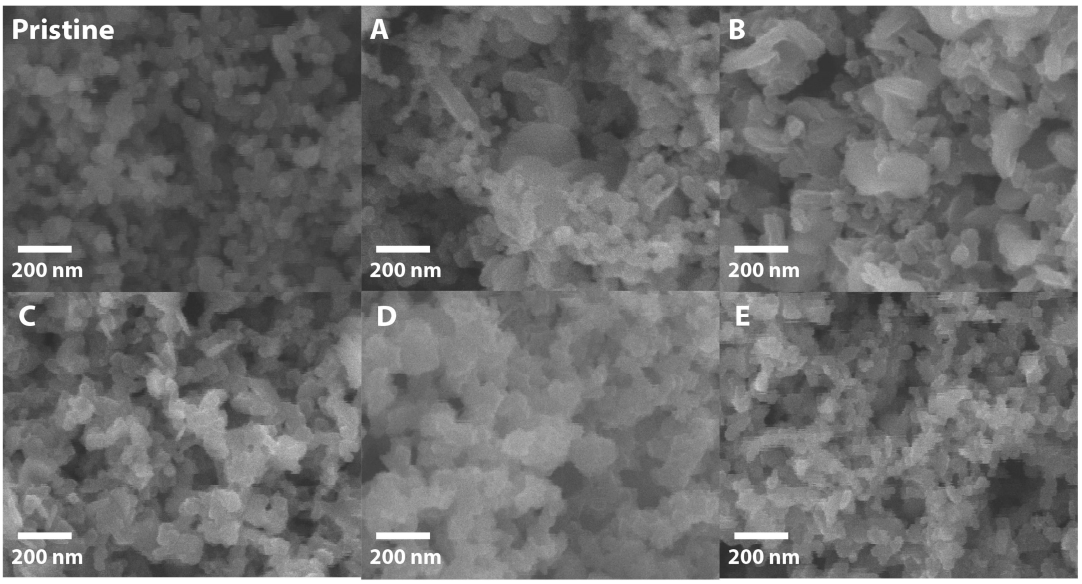

Fig. 5-9 Morphology evolution of Li_2O_2 revealed by SEM images with the decreased discharge potential in Me-Im. The discharge potentials from A to E decreases. A, B, C, E correspond to the points on the CVs of Fig. 5-6 in an order of the decreased potential. The potential of D is at the first peak position, whose potential in between C and E.

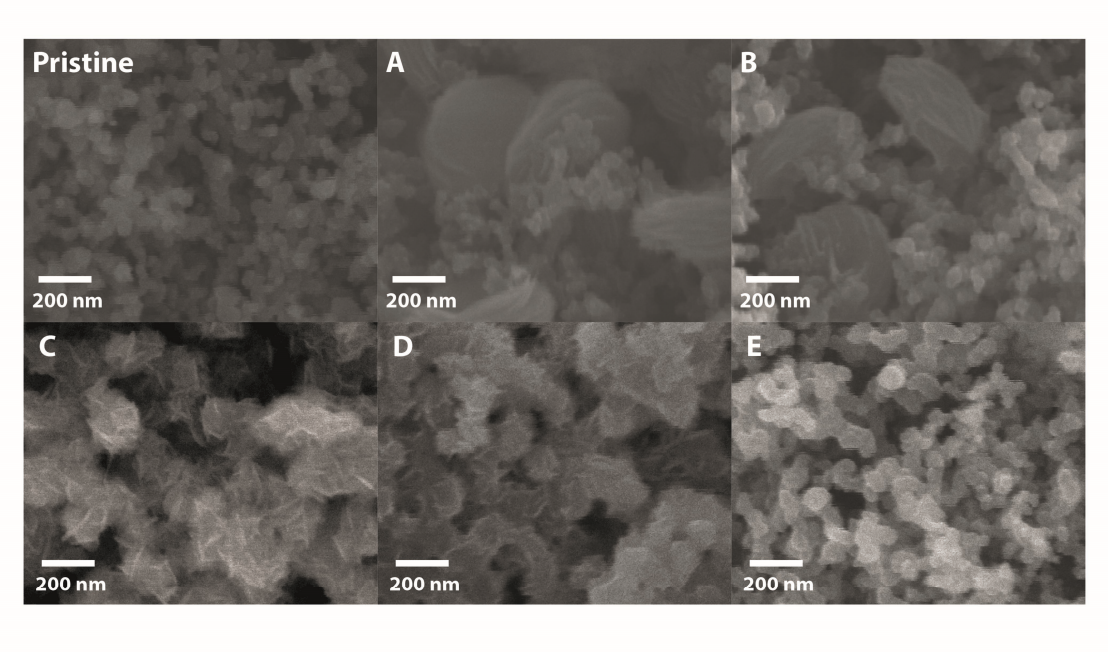

Fig. 5-10 Morphology evolution of Li_2O_2 revealed by SEM images with the decreased discharge potential in DMSO. The discharge potentials from A to E decreases. A, B, C, E correspond to the points on the CVs of Fig. 5-6 in an order of the decreased potential. The potential of D is at the first peak position, whose potential in between C and E.

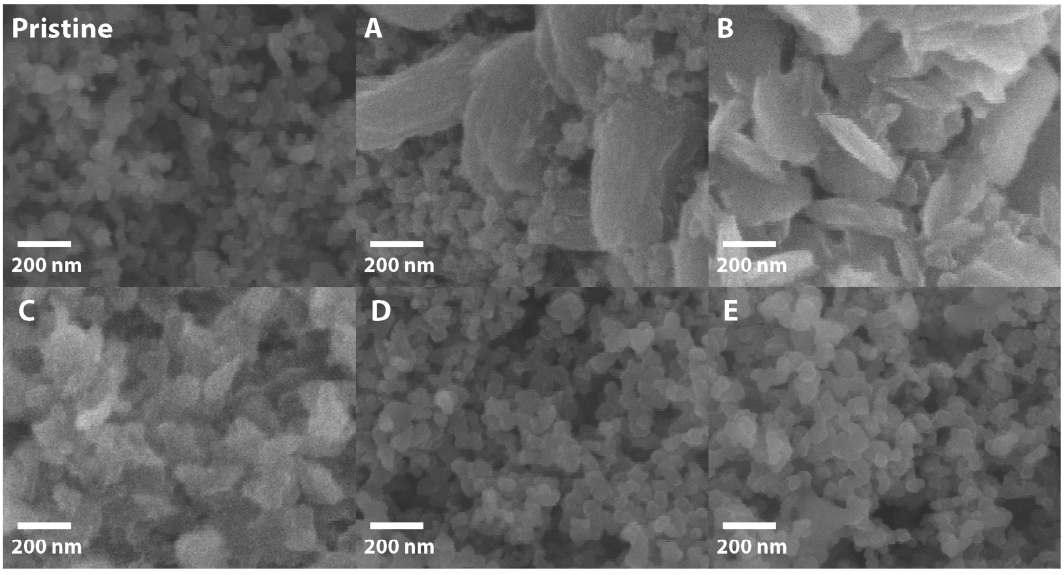

Fig. 5-11 Morphology evolution of Li_2O_2 revealed by SEM images with the decreased discharge potential in DME. The discharge potentials from A to E decreases. A, B, C, E correspond to the points on the CVs of Fig. 5-6 in an order of the decreased potential. The potential of D is at the peak position, whose potential in between C and E.

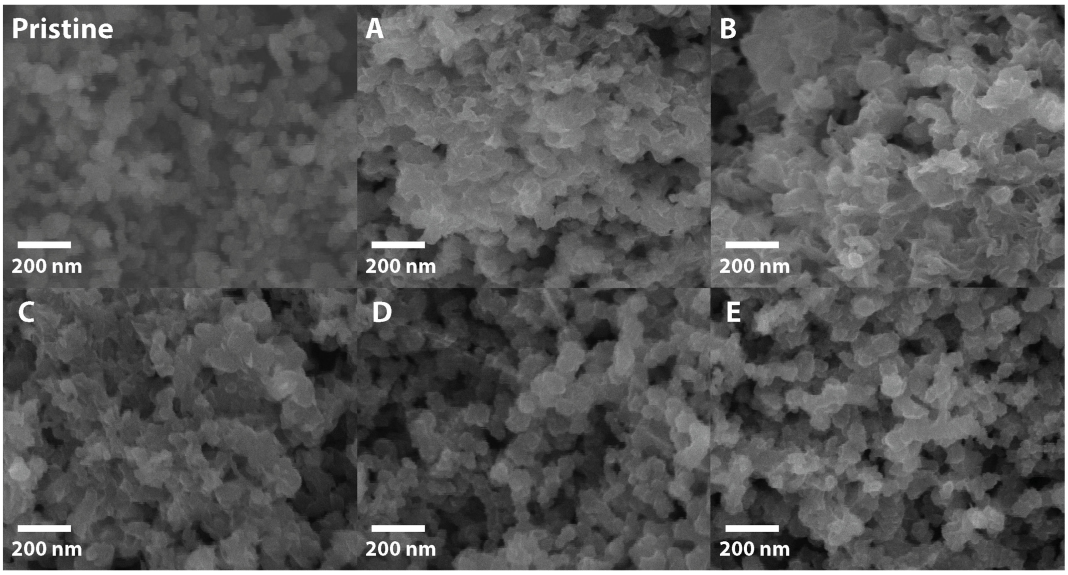

Fig. 5-12 Morphology evolution of Li_2O_2 revealed by SEM images with the decreased discharge potential in CH_3CN. The discharge potentials from A to E decreases. A, B, C, E correspond to the points on the CVs of Fig. 5-6 in an order of the decreased potential. The potential of D is at the peak position, whose potential in between C and E.

Fig. 5-(9-12) presents the morphology evolution based on the variation of the discharge potential in different electrolytes. In Me-Im, DMSO, and DME, the size of the particles decreases with the reduction in discharge potential, but the number of particles in the same area increases. This is ascribed to the increased concentration of O_2^- in the solution driven by the lower discharge potential. According to Nernst equation $E = E^{\ominus} + \frac{RT}{F} ln \frac{[O_2]}{[O_2^-]}$, The $[O_2]$ is a constant due to the equilibrium between the O_2 dissolved in the electrolyte and in the gas phase, and hence, $[O_2^-]$ increases with the decreased potential (E). The increment of O_2^- concentration gives rise to a faster disproportionation rate, which generally leads to more nucleus /seeds, therefore the increased the number of the Li_2O_2 particles formed in the same area. Since there are more Li_2O_2 seeds, together with the fact that lower potential results in more surface film formation and associated lower capacity (lower amount of Li_2O_2 formed), the decrease in the size of Li_2O_2 is explained. As the potential continues reducing, significant second electron reduction steps in, leading to entire film formation as discussed above. It is noteworthy that at medium overpotential corresponding to D in the figures (Fig. 5-9 and Fig.

5-10) small particles can still form in high DN electrolytes, but in DME no Li_2O_2 is observed in Fig. 5-11(D). Acetonitrile exhibits no obvious divergence with the decrease in the discharge potential due to the surface film growth.

5.3.22 The consequence in Li-O_2 batteries.

Up to now, we have elucidated the mechanism of O_2 reduction in aprotic solvents in the presence of Li^+, understood the criteria for different pathways, and observed the potential dependence of the Li_2O_2 morphology in different solvents. In this section, we will pay more attention to the practical consequence of different pathways.

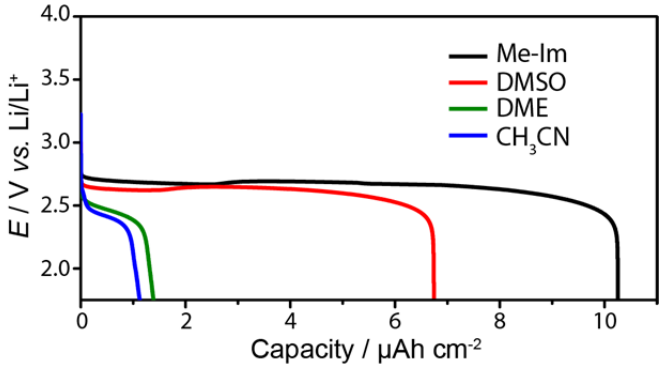

Fig. 5-13 Galvanostatic discharge curve on planar Au electrode in various solvents. The concentration of $LiClO_4$ was 100 mM, and the discharge rate was 60 μA/cm^2.

Fig. 5-13 presents the discharge curves in the four solvents on planar electrodes at the same current density. The capacity decreases from Me-Im to CH_3CN, following the trends of the decreasing DN (increasing $\Delta G^{\ominus}$ of Eq (1)). In CH_3CN, the capacity fades rapidly, resulting in the premature cell death, due to the insulating Li_2O_2 film formation on the electrode surface, whose thickness is estimated to be 6 nm according to the capacity and the area of the electrode, in accord with previous study[15], in which 5-10 nm Li_2O_2 film has been demonstrated to lead to the cell sudden death. In DME, the capacity increases, but still very low, due to the significant involvement of the surface pathway. In high DN solvent, such as Me-Im and DMSO, the capacity goes far beyond that calculated from the film limitation, because the Li_2O_2 is formed from the solution. However, the capacity still reaches a limitation, as surface pathway and surface deposition is not excluded. (See the description of the mechanism.)

In practical batteries, the case will be different. But composite electrode with optimized porous structure can generally accommodate more Li_2O_2 through solution pathway (in high DN solvents) than through the surface pathway (in low DN solvents). For example, carbon black Super P, a kind of carbon commonly used as cathode material in Li-O_2 batteries, has a surface area of *c.a.* 60 m^2/g and density of 160 kg/m^3. The calculated capacity via surface pathway in the low DN solvent is 1100 mAh/g, corresponding to a 7 nm surface layer. The composite electrode, comprising 90% of Super P and 10% of PTFE doubles the density of Super P. Assuming that the pore volume hold 50% of the electrode and 60% of the pores are filled by Li_2O_2 particles from the solution growth, the corresponding capacity can readily reach 3100 mAh/g. For most of the cathode materials for Li-O_2, the solution pathway in high DN solvents results in higher capacity.

5.4 Conclusion

In this chapter, a unified mechanism of O_2 reduction in aprotic solvents is proposed, which is applicable to both high and low DN solvents. The switch point between the surface and solution pathways relies on the solubility of LiO_2, *i.e.*, free energy change of the dissolution reaction $* LiO_2 \rightleftharpoons Li^+_{(solv)} + O^-_{2(solv)} (+ion\ pairs + cluster)$. The potential dependence of morphology of Li_2O_2 in composite carbon electrode is in good accord with this mechanism. In practice, the surface pathway in low DN solvents leads to the Li_2O_2 film formation, which blocks further electron transfer and results in a premature cell death. In contrast, the high DN solvents provides more capacity due to the solution pathway of O_2 reduction. In this point of view, hunting for a stable high DN solvent for Li-O_2 battery is of more interest in future research.

Reference

1. McCloskey, B.D., et al., *On the Mechanism of Nonaqueous Li–O2 Electrochemistry on C and Its Kinetic Overpotentials: Some Implications for Li–Air Batteries.* The Journal of Physical Chemistry C, 2012. **116**(45): p. 23897-23905.
2. Laoire, C.O., et al., *Elucidating the Mechanism of Oxygen Reduction for Lithium-Air Battery Applications.* The Journal of Physical Chemistry C, 2009. **113**(46): p. 20127-20134.
3. Laoire, C.O., et al., *Influence of Nonaqueous Solvents on the Electrochemistry of Oxygen in the Rechargeable Lithium–Air Battery.* The Journal of Physical Chemistry C, 2010. **114**(19): p. 9178-9186.
4. Pearson, R.G., *Hard and Soft Acids and Bases.* Journal of the American Chemical Society, 1963. **85**(22): p. 3533-&.
5. Lu, Y.-C., et al., *Lithium-Oxygen Batteries: Bridging Mechanistic Understanding and Battery Performance.* Energy & Environmental Science, 2013. **6**(3): p. 750-768.
6. Mitchell, R.R., et al., *Mechanisms of Morphological Evolution of Li2O2 Particles During Electrochemical Growth.* The Journal of Physical Chemistry Letters, 2013. **4**(7): p. 1060–1064.
7. Adams, B.D., et al., *Current density dependence of peroxide formation in the Li-O2 battery and its effect on charge.* Energy & Environmental Science, 2013. **6**(6): p. 1772-1778.
8. Sawyer, D.T., et al., *Effects of Media and Electrode Materials on the Electrochemical Reduction of Dioxygen.* Analytical Chemistry, 1982. **54**(11): p. 1720-1724.
9. Vasudevan, D. and H. Wendt, *Electroreduction of oxygen in aprotic media.* Journal of Electroanalytical Chemistry, 1995. **392**(1–2): p. 69-74.
10. Bryantsev, V.S., M. Blanco, and F. Faglioni, *Stability of Lithium Superoxide LiO2 in the Gas Phase: Computational Study of Dimerization and Disproportionation Reactions.* Journal of Physical Chemistry A, 2010. **114**(31): p. 8165-8169.
11. Lu, Y.C., et al., *The Influence of Catalysts on Discharge and Charge Voltages of Rechargeable Li-Oxygen Batteries.* Electrochemical and Solid State Letters, 2010. **13**(6): p. A69-A72.
12. Pasgreta, E., et al., *Ligand-exchange processes on solvated lithium cations: DMSO and water/DMSO mixtures.* Chemphyschem, 2007. **8**(9): p. 1315-1320.
13. Kretschmer, C.B., J. Nowakowska, and R. Wiebe, *Solubility of Oxygen and Nitrogen in Organic Solvents from —25° to 50° C.* Industrial & Engineering Chemistry, 1946. **38**(5): p. 506-509.
14. Snow, R.H., *Thermodynamic Evaluation of the Possibility of Lithium Superoxide Production Technical Report*, 1965.
15. Viswanathan, V., et al., *Electrical conductivity in Li2O2 and its role in determining capacity limitations in non-aqueous Li-O2 batteries.* The Journal of Chemical Physics, 2011. **135**(21): p. 214704.

Chapter 6 Conclusion and Future Works

Firstly, the extremely small-sized anatase and TiO_2(B) nanoparticles with at least one dimension less than 3 nm were synthesis via solvothermal/hydrothermal reaction without the assistance of long-chain organic surfactants. The size and shape of the nanoparticles could be tuned by the variation of synthesis conditions. In particular, the size and shape of the anatase nanoparticles were controlled by altering the ratio of starting materials, and annealing condition. And the size control of TiO_2(B) nanoparticles were achieved by varying the time of hydrothermal reaction. The single-phased TiO_2(B) nanoparticles with dimensions of 2.5x2.5x4.3 nm was achieved for the first time.

The morphology of the nanoparticles was subjected to the combined studies based on the analysis of the PXRD data and TEM images. The characterisation of the phase purity is not simple for extremely small-sized nanomaterials with low symmetric crystal structures due to the peak broadening and overlapping of the PXRD pattern. A systemic method for the characterisation based on diffraction, Raman, solid-state MAS NMR and electrochemistry has been developed for this purpose. This combined method should be able to transplant to identify the purities of other extremely small-sized nanomaterials.

Then, these nanoparticles, with relatively clean surface (free of organics) and high phase purity, served as prime examples for the studies of nanosize effects in Li-ion cells. These nanomaterials demonstrate better lithium storage and loss of plateau with reduced particles size. The electrochemical study of anatase nanosheets with different thickness and surface condition suggests the excessive lithium storage originated not only from pseudocapacitive (interfacial) Li^+-storage, but also from the excessive Li^+-storage from the bulk. The TiO_2(B) nanoparticles also exhibit the similar behaviour. The sub-3nm TiO_2(B) nanoparticles demonstrate a reversible capacity of 221 mAh/g at a rate of 600 mA/g and remain 135 mAh/g at 18000 mA/g without significant capacity fading during cycling, superior to the previous established TiO_2(B) nanotubes and nanowires, exhibiting considerable interest for commercial application.

The method for the synthesis of the extremely small-sized nanomaterials with pure phase and clean surface should be able to be used for the synthesis of other nanomaterials for battery applications, in order to increase the capacity and enhance the rate performance of current Li-ion batteries.

Finally, the O_2 reduction mechanism in aprotic electrolytes for Li-O_2 batteries was been investigated. Techniques, such as CV, RRDE, in-situ Raman, were exploited to characterise

the reduction process. FTIR and SEM were used to study the final product and to examine the morphology of the Li_2O_2 formed under different conditions. A novel mechanism was proposed. This mechanism unifies two previous competing models for the growth of Li_2O_2 during discharge, *i.e.*, Li_2O_2 particle formation in the solution phase and Li_2O_2 film formation on the electrode surface. The switch point from the solution growth of Li_2O_2 to the surface pathway is determined by the solubility of LiO_2 in different electrolytes. High DN electrolytes give rise to better solubility of LiO_2, and hence the Li_2O_2 growth from the solution phase, while low DN electrolytes promote the growth of Li_2O_2 on electrode surface, which blocks further electron transfer and results in a premature cell death and associated low capacity. This mechanism has a positive implication for the high DN electrolytes due to the higher capacity originated from the solution growth of Li_2O_2. The investigations on stable high DN electrolytes should draw more interest in the future research work.

List of Publications

1. Hua X, Liu Z, Bruce PG, Grey CP. The Morphology of TiO_2 (B) Nanoparticles. Journal of the American Chemical Society. 2015;137(42):13612-23.

2. Johnson L, Li C, Liu Z, Chen Y, Freunberger SA, Ashok PC, et al. The role of LiO_2 solubility in O_2 reduction in aprotic solvents and its consequences for Li–O_2 batteries. Nat Chem. 2014 12//print;6(12):1091-9.

3. Andreev YG, Panchmatia PM, Liu Z, Parker SC, Islam MS, Bruce PG. The Shape of TiO_2-B Nanoparticles. Journal of the American Chemical Society. 2014 2014/04/30;136(17):6306-12.

4. Ren Y, Ma Z, Morris RE, Liu Z, Jiao F, Dai S, et al. A solid with a hierarchical tetramodal micro-meso-macro pore size distribution. Nat Commun. 2013 06/14/online;4.

5. Ottakam Thotiyl MM, Freunberger SA, Peng Z, Chen Y, Liu Z, Bruce PG. A stable cathode for the aprotic Li–O_2 battery. Nat Mater. 2013 11//print;12(11):1050-6.

6. Liu Z, Andreev YG, Robert Armstrong A, Brutti S, Ren Y, Bruce PG. Nanostructured TiO_2(B): the effect of size and shape on anode properties for Li-ion batteries. Progress in Natural Science: Materials International. 2013 6//;23(3):235-44.

7. Ren Y, Liu Z, Pourpoint F, Armstrong AR, Grey CP, Bruce PG. Nanoparticulate TiO_2(B): An Anode for Lithium-Ion Batteries. Angewandte Chemie. 2012;124(9):2206-9.